

INVESTIGATING PATHOLOGICAL  
FEATURES OF A NOVEL AMYOTROPHIC  
LATERAL SCLEROSIS MOUSE MODEL

By

Winonah Ruby Riddell  
B. Med. Sc. (Biomolecular)

A THESIS SUBMITTED TO MACQUARIE UNIVERSITY  
FOR THE DEGREE OF  
MASTER OF RESEARCH  
DEPARTMENT OF BIOMEDICAL SCIENCES  
FACULTY OF MEDICINE AND HEALTH SCIENCES  
FEBRUARY 2020



**MACQUARIE**  
University  
SYDNEY · AUSTRALIA



# Declaration

The following is a thesis submitted to Macquarie University in fulfilment of the requirement for the Degree of Master of Research.

The work presented in this thesis is my own and to the best of my knowledge and belief, original. References and sources of information have been acknowledged in the text and references list. All help and assistance I was provided in the work or preparation of this thesis is noted below and also in the text. I declare that I have not submitted the material within this thesis, either in full or in part, for a degree at this or any other university.

The following lists the technical support I received whilst completing this thesis: generation and provision of the CRISPR-*CCNF*<sup>S621G</sup> mouse model by Professor Roger Chung, neuro-2a cell protein lysate extraction was performed by Dr Shu Yang, mouse brain protein lysate extraction was performed by Ms Flora Cheng, mass spectrometry was performed by Ms Flora Cheng and Dr Albert Lee, initial mass spectrometry data quality check was performed by Dr Albert Lee, and DNA sequencing was performed by Macrogen, South Korea.

Research conducted for this thesis was granted approval by the Macquarie University Institutional Biosafety Committee.

**Biosafety approval #5201401007.**

Animal ethics approval was not required for this thesis as the mouse tissue used in the thesis had been collected prior to commencement.

This thesis project was funded by Macquarie University.

Winonah Ruby Riddell



# Acknowledgements

Foremost, I would like to thank my supervisors Professor Ian Blair and Dr Shu Yang for the opportunity to work on this project and for the support, encouragement, guidance, and patience you have given me during my Masters. Your passion and knowledge for the field inspired and motivated me to keep working to the best of my abilities.

My sincerest thanks to Natalie for her invaluable lab advice with this project. The lab would have been a very lonely and even more stressful place without you. Thank you — Kelly for introducing me to Latex and to yourself, Emily, Sandrine and Sharlynn for helping me troubleshoot formatting issues; Emily for genotyping; Alison for your incredibly quick and valuable feedback. Thank you also to everyone else in the Blair research group who have provided assistance and guidance when I needed it.

My appreciation is extended to the researchers who collaborated with me during the project; Roger for providing the CRISPR-*CCNF*<sup>S621G</sup> mouse samples; Albert for explaining how to use protein analysis software, Rowan for providing practice mouse tissue for me to initially work with, Roshana for teaching me how to use the tissue processor and embedding machine, Amanda for assisting with setting up RNA extraction and qPCR and for checking in on my wellbeing, and Hannah for giving me proteomics tips and being a friendly face I could go to for advice.

To my family, especially my parents Philip and Ruth, thank you for your constant support and reminders to keep living a balanced life during my Masters. Yankai, thank you for providing a listening ear and reassurance when I needed it.

Finally, thank you to Jen Rowland for your support and thesis tips, and my fellow MRes peers for helping me maintain my sanity. Our lunchtime banter was refreshing. 😊

- Winonah



# Abstract

Amyotrophic lateral sclerosis (ALS) is a fatal neurodegenerative disease characterised by the loss of brain and spinal cord motor neurons. A proportion of ALS patients also develop frontotemporal dementia (FTD). A mutation in the *CCNF* gene (*CCNF*<sup>S621G</sup>) was recently reported in a family with ALS and FTD, offering a new opportunity to model ALS/FTD, including development of pre-clinical animal models. Over-expression of this mutation has been studied in zebrafish and in two mouse cell lines, NSC-34 and neuro-2a. However, the effects of endogenously expressed *CCNF*<sup>S621G</sup> on the mammalian system remain unclear. To assess this, tissues from a previously generated CRISPR-Cas9 mouse model carrying *CCNF*<sup>S621G</sup> in its genome (CRISPR-*CCNF*<sup>S621G</sup>), were studied. This thesis **aimed** to characterise, for the first time, pathological features in the CRISPR-*CCNF*<sup>S621G</sup> mouse model, to evaluate its utility for ALS research. Specifically, this study assessed the impact of *CCNF*<sup>S621G</sup> on cyclin F expression, and investigated characteristic ALS/FTD histopathologies (mis-localised TDP-43, hyper-phosphorylated and aggregates of TDP-43, and ubiquitinated protein inclusions) and proteomic changes within brain and spinal cord tissues from six-month-old heterozygous and homozygous CRISPR-*CCNF*<sup>S621G</sup> mice. Genetics, molecular biology, histology, and proteomic techniques, were employed. It was found that *CCNF* gene (mRNA) and cyclin F protein levels were not altered in the CRISPR-*CCNF*<sup>S621G</sup> mice. No characteristic ALS/FTD histopathologies were identified within brain and spinal cord tissues from the CRISPR-*CCNF*<sup>S621G</sup> mice, but a significant loss of spinal cord motor neurons was observed in homozygous CRISPR-*CCNF*<sup>S621G</sup> mice when compared to control and heterozygous CRISPR-*CCNF*<sup>S621G</sup> mice. Filtering and analysis of proteomics data identified aberrantly expressed proteins in the CRISPR-*CCNF*<sup>S621G</sup> mice, which included *TBC1D15* and *GNAI2* among others, that are implicated in ALS-relevant biological processes. In summary, this project systematically characterised molecular and cellular pathologies present in the CRISPR-*CCNF*<sup>S621G</sup> mice, which may represent early features associated with disease pathogenesis prior to the occurrence of significant motor deficits. This was the first CRISPR-*CCNF* mouse model study and provides insights into cellular and biochemical changes relevant to ALS/FTD-linked *CCNF*<sup>S621G</sup>. Future studies in an older cohort are required to examine progression of these changes and to gain a full understanding of *CCNF*-related disease aetiology.



# Contents

<b>Declaration</b>	<b>iii</b>
<b>Acknowledgements</b>	<b>v</b>
<b>Abstract</b>	<b>vii</b>
<b>List of Figures</b>	<b>xiii</b>
<b>List of Tables</b>	<b>xv</b>
<b>Abbreviations</b>	<b>xvii</b>
<b>1 Introduction</b>	<b>1</b>
1.1 Amyotrophic Lateral Sclerosis (ALS)	1
1.2 Genetics, proteins, and ALS	2
1.2.1 Mouse models of ALS	3
1.2.2 <i>CCNF</i>	10
1.3 Aims	12
<b>2 Subjects &amp; materials</b>	<b>15</b>
2.1 Mouse model cohorts	15
2.2 Chemicals, reagents, materials, and kits	16
2.3 Antibodies	20
<b>3 Methods</b>	<b>23</b>
3.1 CRISPR- <i>CCNF</i> <sup>S621G</sup> mouse model genotyping	23
3.1.1 DNA extraction	23
3.1.2 Primer design	24
3.1.3 Primer optimisation	24
3.1.4 DNA amplification	25
3.1.5 DNA sequencing and analysis	26
3.2 CRISPR- <i>CCNF</i> <sup>S621G</sup> mouse model tissue sample preparation	26

3.2.1	Tissue fixation, processing, and embedding . . . . .	26
3.2.2	Tissue sectioning . . . . .	27
3.3	CRISPR- <i>CCNF</i> <sup>S621G</sup> mouse model	
	histopathology . . . . .	27
3.3.1	Immunofluorescence staining . . . . .	27
3.3.2	Nissl staining . . . . .	33
3.4	CRISPR- <i>CCNF</i> <sup>S621G</sup> mouse model tissue protein analysis . . . . .	34
3.4.1	Protein lysate collection . . . . .	34
3.4.2	Mass spectrometry . . . . .	35
3.4.3	Protein analysis from mass spectrometry . . . . .	35
3.4.4	Western blot . . . . .	36
3.4.5	Reverse transcription-quantitative polymerase chain reaction (RT-qPCR) . . . . .	39
<b>4</b>	<b>Results</b>	<b>43</b>
4.1	CRISPR- <i>CCNF</i> <sup>S621G</sup> mouse model genotyping . . . . .	43
4.2	CRISPR- <i>CCNF</i> <sup>S621G</sup> mouse model	
	histopathology . . . . .	45
4.2.1	Immunofluorescence staining . . . . .	45
4.2.2	Nissl staining . . . . .	68
4.3	Proteomic analysis in CRISPR- <i>CCNF</i> <sup>S621G</sup> mouse . . . . .	70
4.3.1	Mass spectrometry and protein analysis . . . . .	70
4.3.2	Western blot . . . . .	79
4.3.3	RNA extraction and RT-qPCR . . . . .	85
<b>5</b>	<b>Discussion</b>	<b>93</b>
5.1	Evaluation of ALS/FTD histopathology in the CRISPR- <i>CCNF</i> <sup>S621G</sup> mouse model . . . . .	94
5.1.1	Immunofluorescence staining . . . . .	94
5.1.2	Nissl staining and spinal cord motor neuron counts . . . . .	97
5.2	<i>CCNF</i> expression level changes . . . . .	99
5.2.1	The <i>CCNF</i> <sup>S621G</sup> mutation did not lead to loss of <i>CCNF</i> gene expression in CRISPR- <i>CCNF</i> <sup>S621G</sup> mouse model . . . . .	99
5.2.2	The <i>CCNF</i> <sup>S621G</sup> mutation did not lead to loss of cyclin F protein expression in the <i>CCNF</i> <sup>S621G</sup> mouse model . . . . .	100
5.2.3	Other protein changes . . . . .	102
5.3	Future directions - further analysis of the CRISPR- <i>CCNF</i> <sup>S621G</sup> mouse model	110
5.3.1	Refinements . . . . .	110
5.3.2	Compare data from six-month-old cohorts to an aged cohort . . . . .	112

---

5.4	Conclusion . . . . .	113
<b>A</b>	<b>Appendix</b>	<b>115</b>
A.1	Methods . . . . .	115
A.1.1	Genotyping . . . . .	115
A.1.2	CRISPR- <i>CCNF</i> <sup>S621G</sup> mouse model histopathology . . . . .	116
A.1.3	CRISPR- <i>CCNF</i> <sup>S621G</sup> mouse model tissue protein analysis . . . . .	117
A.2	Results . . . . .	120
A.2.1	Mass spectrometry . . . . .	120
A.2.2	Western blot . . . . .	122
A.3	Biosafety approval letter . . . . .	122
	<b>References</b>	<b>127</b>



# List of Figures

1.1	The CRISPR-Cas9 system. . . . .	4
1.2	Cyclin F protein structure. . . . .	10
1.3	Project methodology overview. . . . .	13
3.1	Brain and spinal cord tissue section collection. . . . .	28
3.2	Motor cortex, hippocampus, and ventral horn - regions of interest for histopathological analysis. . . . .	31
3.3	Nissl stained ventral spinal cord region delimited for motor neuron counts. . . . .	34
3.4	cDNA synthesis protocol. . . . .	40
4.1	Cyclin F protein and cDNA sequence homology between humans and mice. . . . .	44
4.2	PCR primer optimisation. . . . .	44
4.3	Mouse genotypes were confirmed by sequencing. . . . .	45
4.4	Rabbit cyclin F (Santa Cruz) antibody optimisation. . . . .	46
4.5	Mouse NeuN (Merck Millipore) antibody optimisation. . . . .	49
4.6	Mouse TDP-43 (Abnova) and rabbit TDP-43 (ProteinTech) antibody optimisation. . . . .	51
4.7	Mouse cyclin F (Santa Cruz) antibody optimisation. . . . .	53
4.8	Mouse cyclin F blocking peptide (Santa Cruz) antibody optimisation. . . . .	55
4.9	Rabbit cyclin F (LifeSpan BioSciences) antibody optimisation. . . . .	56
4.10	TDP-43 does not aggregate in, or mis-localise to, the cytoplasm of motor cortex neurons in CRISPR- <i>CCNF</i> <sup>S621G</sup> mice . . . . .	59
4.11	TDP-43 remains nuclear in the hippocampus of CRISPR- <i>CCNF</i> <sup>S621G</sup> mice, where it co-localises with cyclin F. . . . .	60
4.12	No difference in TDP-43 or cyclin F staining in the spinal cord of WT and CRISPR- <i>CCNF</i> <sup>S621G</sup> mice. . . . .	61
4.13	Phosphorylated TDP-43 was not detected in cortical tissue from CRISPR- <i>CCNF</i> <sup>S621G</sup> mice. . . . .	62
4.14	Phosphorylated TDP-43 was not found in hippocampal neurons from CRISPR- <i>CCNF</i> <sup>S621G</sup> mice. . . . .	63

4.15	Phosphorylated TDP-43 was not detected in cortical tissue from CRISPR- <i>CCNF</i> <sup>S621G</sup> mice. . . . .	64
4.16	Diffuse ubiquitin and puncta in motor cortex neurons from heterozygous and homozygous CRISPR- <i>CCNF</i> <sup>S621G</sup> mice. . . . .	65
4.17	No ubiquitin-positive inclusions were detected in hippocampal neurons from CRISPR- <i>CCNF</i> <sup>S621G</sup> mice. . . . .	66
4.18	Diffuse ubiquitin staining in spinal cord motor neurons from CRISPR- <i>CCNF</i> <sup>S621G</sup> mice. . . . .	67
4.19	Cyclin F expression was not altered in spinal cord motor neurons of mice with S621G mutation. . . . .	68
4.20	Nissl stain time comparison . . . . .	69
4.21	Total number of lumbar spinal cord motor neurons was significantly reduced in homozygous mice compared to WT and heterozygous mice. . . . .	69
4.22	Nissl stained spinal cord sections showed that homozygous CRISPR- <i>CCNF</i> <sup>S621G</sup> mice had significantly less lumbar spinal cord motor neurons than their WT and heterozygous counterparts. . . . .	70
4.23	Quality check of MS from brain protein lysates. . . . .	71
4.24	Overview of protein expression changes identified in CRISPR- <i>CCNF</i> <sup>S621G</sup> brain protein lysates by MS. . . . .	72
4.25	Total protein numbers from MS on WT and heterozygous and homozygous CRISPR- <i>CCNF</i> <sup>S621G</sup> brain protein lysates. . . . .	73
4.26	Functional classification of unregulated (“over-expressed”) proteins in the CRISPR- <i>CCNF</i> <sup>S621G</sup> model – PANTHER analysis. . . . .	74
4.27	Functional classification of “under-expressed” proteins in the CRISPR- <i>CCNF</i> <sup>S621G</sup> model – PANTHER analysis. . . . .	76
4.28	Network between the “under-expressed” proteins in CRISPR- <i>CCNF</i> <sup>S621G</sup> mice. . . . .	78
4.29	TDP-43 protein expression level was not altered in CRISPR- <i>CCNF</i> <sup>S621G</sup> mice. . . . .	81
4.30	Ubiquitin levels unaffected by mutant cyclin F protein. . . . .	82
4.31	No specific cyclin F band was detected in mouse brain lysate when using Santa Cruz or ThermoFisher cyclin F antibodies. . . . .	83
4.32	Cyclin F was unidentifiable in mouse spleen protein lysate by Western blot but speculatively apparent in HEK293 lysate. . . . .	84
4.34	qPCR showed that the S621G mutation did not significantly alter <i>CCNF</i> gene expression in mouse spleen tissues. . . . .	88
A.1	First Western blot membrane — incomplete protein transfer. . . . .	122

# List of Tables

1.1	Major ALS-linked genes and representative transgenic mouse models. . . .	7
2.1	Mouse cohorts . . . . .	15
2.2	Chemicals, reagents and materials . . . . .	18
2.3	Kits . . . . .	20
2.4	Antibodies, their concentrations and applications . . . . .	21
3.1	Genotyping primers . . . . .	24
3.2	Primer optimisation PCR reaction mixture and thermocycling conditions .	25
3.3	PCR DNA amplification reaction mixture and thermocycling conditions . .	25
3.4	Tissue processing protocol . . . . .	26
3.5	Tissue washing steps for paraffin wax removal . . . . .	29
3.6	Summary of combinations and conditions used in each round of optimisa- tion IF staining . . . . .	30
3.7	Summary of combinations and conditions used in each round of IF staining	32
3.8	Summary of combinations used for each Western blot . . . . .	38
3.9	Test qPCR reaction mixture and plate layout with reaction combinations .	40
3.10	qPCR conditions. . . . .	41
4.1	IF antibody optimisation outcomes – Rb cyclin F (Santa Cruz) . . . . .	47
4.2	IF antibody optimisation outcomes – Ms NeuN (Merck Millipore) . . . . .	50
4.3	IF antibody optimisation outcomes – Ms TDP-43 (Abnova) and Rb TDP- 43 (ProteinTech) . . . . .	52
4.4	IF antibody optimisation outcomes – Ms cyclin F (Santa Cruz) . . . . .	54
4.5	IF antibody optimisation outcomes – Ms cyclin F blocking peptide (Santa Cruz) . . . . .	55
4.6	IF antibody optimisation outcomes – Rb cyclin F (LifeSpan BioSciences) .	57
4.7	“Over-expression” results from lowest level of PANTHER molecular func- tion analysis. . . . .	75
4.8	“Over-expressed” biological processes in CRISPR- <i>CCNF</i> <sup>S621G</sup> mice. . . . .	75

---

4.9	Final “under-expression” results from PANTHER molecular function analysis - GTPase activity . . . . .	77
4.10	GO biological processes associated with ALS relevant “under-expressed” proteins . . . . .	79
4.11	Nucleic acid concentrations and purity of mouse RNA samples. . . . .	86
4.12	qPCR data and calculation terminology . . . . .	87
4.13	Preliminary qPCR data . . . . .	87
4.14	Spleen tissue qPCR data . . . . .	89
4.15	Mouse spleen cDNA quantity and quality. . . . .	91
5.1	Previously reported mutant <i>CCNF</i> associated proteins. . . . .	108
5.2	Life stage equivalents in mice and humans. . . . .	113
A.1	Mouse ( <i>mus musculus</i> ) exon 17, NM_007634.4. . . . .	115
A.2	Human ( <i>homo sapiens</i> ) exon 16, NM_001761.2. . . . .	115
A.3	GO biological process categories from the 564 “under-expressed” proteins in the heterozygous and homozygous CRISPR- <i>CCNF</i> <sup>S621G</sup> mice. . . . .	120

# Abbreviations

AD	Alzheimer's disease
ALS	amyotrophic lateral sclerosis
a.u.	arbitrary units
bp	base pair
cDNA	coding DNA
CNS	central nervous system
DPBS	Dulbecco's phosphate-buffered saline
DNA	deoxyribonucleic acid
DMEM	Dulbecco's Modified Eagle's Medium
fALS	familial ALS
FBS	fetal bovine serum
FFPE	formalin-fixed paraffin-embedded
FTD	frontotemporal dementia
IF	immunofluorescence
IHC	immunohistochemistry
mRNA	messenger RNA
MN	motor neuron
NLS	nuclear localisation signal
PAGE	polyacrylamide gel electrophoresis

PBS	phosphate buffered saline
PCR	polymerase chain reaction
qPCR	quantitative PCR
RIPA	radioimmunoprecipitation assay
RNA	ribonucleic acid
RT	room temperature
sALS	sporadic ALS
SC	spinal cord
SDS	sodium dodecyl sulfate
T <sub>A</sub>	annealing temperature
TBS	tris-buffered saline
UPS	ubiquitin-proteasome system
UTR	untranslated region
WB	Western blot
WT	Wild-type

# 1

## Introduction

### 1.1 Amyotrophic Lateral Sclerosis (ALS)

The debilitating, ultimately fatal, and incurable neurodegenerative disease Amyotrophic Lateral Sclerosis (ALS), also known as Motor Neuron Disease, is the cause of death for around 700 people every year in Australia ([Australian Institute of Health and Welfare \(AIHW\), 2018](#)). Clinically, the disease is recognised by a combination of symptoms such as muscle weakness and wasting, hyporeflexia, deterioration of limb motor function, swallowing difficulties, and dysarthria ([Picher-Martel et al., 2016](#); [Tan et al., 2017](#)). These symptoms are caused by progressive dysfunction, decay, and death of upper motor neurons in the brain and lower motor neurons in the spinal cord. More specifically, it is the motor neurons in the brainstem, primary motor cortex and anterior (ventral) horns that are affected in disease ([Mancuso and Navarro, 2015](#)). This neuronal loss then leads to patient death, predominantly by respiratory failure as respiratory muscles that are necessary for breathing, are no longer innervated ([Nguyen et al., 2018](#)). Death can occur anywhere from months to years after symptom onset, depending on the rate of disease course ([McCann et al., 2017](#); [Tan et al., 2017](#)).

ALS may be classified as familial (fALS), in which the patient has inherited the disease from a family member, or sporadic (sALS) in which disease has arisen from a combination of external triggers and genetic risk factors ([Renton et al., 2013](#)). Despite the division being approximately 10% fALS and 90% sALS ([Williams et al., 2016](#)), at the cellular level (especially in neurons), the disease is characterised by similar features. In surviving

neurons, pathological hallmarks of ALS include protein misfolding and aggregates of ubiquitinated proteins such as TAR DNA-binding protein 43 (TDP-43) (Al-Chalabi et al., 2012), protein mislocalisation, excessive protein phosphorylation, the presence of RNA containing stress granules (Fan and Leung, 2016), and neuroinflammation (Mancuso and Navarro, 2015).

Ubiquitin-tagged proteins are typically flagged for degradation by the ubiquitin-proteasome-system (UPS), one of the main mechanisms used by cells to remove unnecessary proteins in order to maintain proteostasis (Galper et al., 2017). The persistence of ubiquitinated aggregates in ALS suggests there is a fault with UPS-mediated degradation. Other pathological hallmarks also imply that RNA processing and prevention of oxidative stress, are also altered in disease state. Some of these cellular and molecular abnormalities are also seen in other central nervous system (CNS) diseases such as frontotemporal dementia (FTD), Alzheimer’s disease, and Parkinson’s disease, implying that they share some pathological mechanisms (Al-Chalabi et al., 2012; Renton et al., 2013). Notably, TDP-43 positive aggregates, which are found in tissues from 97% of ALS cases (in nearly all sALS and around 84% fALS cases (Tan et al., 2017)), are also present in around half of FTD cases (Neumann et al., 2006; Scotter et al., 2015). As well, FTD has been reported in around 15% of ALS cases and as many as half of all ALS cases have evidence of cognitive and behavioural dysfunction (Belzil et al., 2016; Ng et al., 2015). As such, ALS and FTD are considered a spectrum of disease (Al-Chalabi et al., 2012).

## 1.2 Genetics, proteins, and ALS

Advancements in whole genome and exome sequencing, as well as genetic analysis, have permitted the efficient screening of thousands of ALS patients and their families, and the identification of around thirty genes that play a role in the disease. Mutations in four of these genes account for over half of fALS patients (McCann et al., 2017). These major genes are chromosome 9 open reading frame 72 (*C9orf72*), fused in sarcoma gene (*FUS*), superoxide dismutase 1 gene (*SOD1*), and transactive response DNA binding protein gene (*TARDBP*).

*C9orf72* encodes the neuronally expressed C9orf72 protein that is thought to operate on DNA transcription, RNA translation, and endosomal trafficking (Balendra and Isaacs, 2018; Farg et al., 2014). Abnormal expansions of a GGGGCC hexanucleotide repeat in *C9orf72* are the most common cause of, both ALS and FTD (O’Rourke et al., 2015). It is speculated that expansions may cause neurodegeneration through a combination of: loss of normal C9orf72 function; disruption of RNA metabolism and nucleolar function due to build-up of RNA foci containing the hexanucleotide

repeats (Renton et al., 2013); and toxic gain-of-function through dipeptide repeat proteins that are encoded by the hexanucleotide repeats (Balendra and Isaacs, 2018; Lutz, 2018). *FUS* encodes a nuclear, RNA binding protein (FUS) that is involved in RNA processing (splicing, transcription, and translation) (Machamer et al., 2014). Most *FUS* mutations occur within a nuclear localisation signal region which leads to loss of nuclear function and cytoplasmic *FUS* aggregates (Al-Chalabi et al., 2012). *SOD1* encodes copper/zinc superoxide dismutase that binds to copper and zinc molecules to breakdown superoxide radicals (byproducts of cellular processes). Mutations in *SOD1* contribute to the accumulation of charged toxic species, as a result of improper binding and breakdown of superoxide radicals (Deng et al., 2006). It has also been speculated that a threshold of mutant *SOD1* protein must be reached before it triggers neurodegeneration (Lutz, 2018). *TARDBP* encodes the predominantly nuclear TAR DNA binding protein of 43 kDa (TDP-43). TDP-43 is an RNA binding protein that regulates transcription, alternative splicing, and stability of target RNA transcripts (Al-Chalabi et al., 2012; Berning and Walker, 2019). In ALS and FTD with TDP-43 pathology, TDP-43 mis-localises to the cytoplasm where it forms aggregates. This is thought to lead to loss of its normal nuclear function and gain of toxic function in the cytoplasm. TDP-43 pathology is present in almost all sALS and fALS cases, with the exception of some *SOD1* and *FUS* mutations (Renton et al., 2013).

### 1.2.1 Mouse models of ALS

Studying the effects of ALS-linked gene mutations is valuable for confirming their roles in disease pathogenesis and understanding disease mechanisms. Animal models carrying these mutations and mimicking features of disease, can provide insight to the complex and continuously interacting molecular processes and protein pathways that occur, and define links between genes and disease (Xia et al., 2012). Numerous animal species have been used to model ALS, the most commonly used being rodents (Mancuso and Navarro, 2015). Reported models include stable transgenic gene knock-down, gene knock-in, or transient gene expression animals. Traditionally, knock-in mouse lines were created through insertion of a vector, that carried a mutant ALS/FTD-linked gene into the genome of mouse, via pronuclear microinjection (Liu, 2013). This relied on random integration of the DNA into the mouse's genome, which resulted in various levels and locations of gene expression that were not necessarily representative of what occurs in patients with disease. Other approaches to create knock-in or knock-out heritable genome changes in mice include the use of site-specific recombinases (Cre-LoxP and FLP-FRT) and artificial endonucleases (zinc finger nucleases and transcription activator-like effector

nucleases (Talens)). These provide a more targeted approach for transgenesis, as modifications are directed to specific locations in the genome. Site-specific recombinases can only be used if the mouse genome contains both Cre and LoxP, or FLP and FRT genes, such that recombination can occur between the two sites resulting in gene deletion, inversion or translocation (Liu, 2013). The endonucleases utilise engineered DNA binding domains that direct double strand DNA-cleavage and prevent gene expression (Sander and Joung, 2014).

Knock-down or gene silenced mouse models can also be created through the use of antisense oligonucleotides (ASOs) or small interfering RNA (siRNA). These models differ to those mentioned above as they carry non-heritable genomic changes. ASOs are synthetic single-stranded DNA or RNA that are complementary to a specific region in the genome (Evers et al., 2015). RNA ASOs reduce protein translation by binding to messenger RNA (mRNA) and thus hindering ribosomal subunits, and DNA ASOs bind to complementary RNA to form DNA/RNA hybrids that are degraded by RnaseH enzyme to inhibit protein expression (Watts and Corey, 2012). siRNA are delivered into the mouse as double-stranded duplexes that associate with the Argonaute component of the RNA-induced silencing complex (Watts and Corey, 2012). One strand is then lost and the remaining strand (guide strand) binds to complementary RNA thereby silencing gene expression.

More recently, Clustered Regularly Interspaced Short Palindromic Repeats (CRISPR)-Cas9 genome editing has been increasingly adopted as an efficient method to create both knock-in and knock-out mouse models. The CRISPR-Cas9 system is composed of a guide RNA (gRNA) and a Cas9 nuclease (figure 1.1). First, the gRNA associates with the

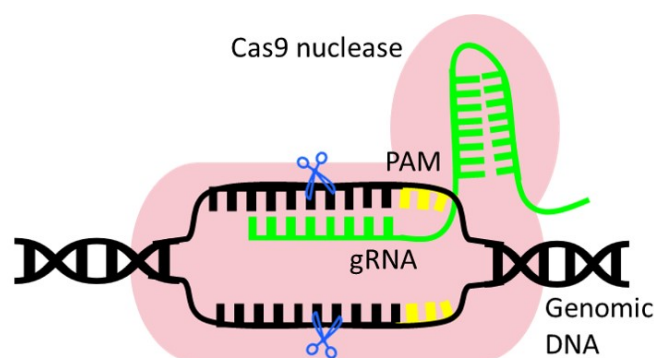


FIGURE 1.1: **The CRISPR-Cas9 system.** In this representation, the black strands are genomic DNA, the green strand is single stranded gRNA, the yellow notches are the PAM sequence, and the blue scissors illustrate that the CRISPR-Cas9 system makes a double strand cut in genomic DNA, at a specific location.

Cas9 nuclease to form a complex. This Cas9 complex locates and binds to a protospacer adjacent motif (PAM) sequence in the genome where the gRNA then unwinds the double

helix until it finds and binds to a complementary sequence. Here, Cas9 cuts the DNA, making a double strand break, which the cell then tries to repair through non-homologous end joining and homology dependent repair. For knock-in, CRISPR-Cas9 utilises a DNA repair template with homology to the ends of the double strand break, to incorporate sequence via homology dependent repair (Tu et al., 2015). For knock-out or knock-down, the CRISPR-Cas9 system makes a double strand cut, and indels formed in the repair process of non homologous end-joining, can result in silenced or reduced gene expression. CRISPR-Cas9's greater control over the location of DNA cleavage and transcript insertion, results in a more accurate representation of disease (Kruminis-Kaszkiel et al., 2018). Genome editing using CRISPR-Cas9 can be a relatively quick process if the method is optimised, taking just months as opposed to years to generate a traditional stable transgenic mouse line.

Other methods used to create ALS mouse models include the injection of mRNA of the respective ALS/FTD gene of interest into a mouse embryo, or by injection of a virus (for example adeno-associated virus) that carry the transgene into an adult mouse. The resulting mice transiently express the genes. However, short term gene expression may be insufficient cause ALS/FTD-like features.

Table 1.1 lists a selection of reported ALS mouse models based on major ALS-linked genes, that were generated using a variety of methods. Their analysis has provided a vast amount of information about disease. The creation of ALS/FTD mouse models using CRISPR/Cas9 has only recently been adopted (Anderson et al., 2019).



TABLE 1.1: Major ALS-linked genes and representative transgenic mouse models.

Gene (mutation)	Model type	Method	Main finding	Reference
<i>C9orf72</i>	Deletion	ZFN pronuclear microinjection	Normal functioning of C9orf72 necessary for macrophage cleanup of cell debris and foreign particles. Loss of this leads to neuroinflammation in the spleen and CNS.	(O'Rourke et al., 2016)
<i>C9orf72</i> ((G <sub>4</sub> C <sub>2</sub> ) <sub>800</sub> )	Insertion - over-expression	BAC pronuclear microinjection	C9orf72 over-expression resulted in sense and antisense RNA foci throughout the cortex in the brain, dipeptide repeat production and RAN dipeptides. However, these were insufficient to cause neurodegeneration on their own. Nucleolar function was also disrupted as seen through altered nucleolin distribution.	(O'Rourke et al., 2015)
<i>C9orf72</i> ((G <sub>4</sub> C <sub>2</sub> ) <sub>66</sub> )	Insertion - transient over-expression	Intracerebral AAV injection	C9orf72 hexanucleotide repeat expansions may play a role in the initiation of TDP-43 pathology. ASOs targeted to the repeat expansions may relieve this TDP-43 toxicity, and prevent formation of RNA foci and RAN translation.	(Chew et al., 2015)
<i>FUS</i>	Knock-out - silencing	Blastocysts were injected with FUS knock-out embryonic cells. Mice from these were crossed with a second strain to achieve homozygosity.	Complete loss of normal FUS function did not result in ALS-phenotypic neurodegeneration. This suggests that additional adverse factors are needed to cause disease. SOD1 loss also appeared to induce abnormal behaviour (hyperactivity and reduced anxiety) and the formation of vacuole-like structures in hippocampus.	(Hicks et al., 2000; Kino et al., 2015)
<i>FUS</i> (R521C, P525L)	Knock-in - inducible	Cre-LoxP recombination	Synaptic failure and withdrawal of axons from neuromuscular junction occurred early in disease and prior to slow-progressing motor neuron neurodegeneration. Mutant FUS proteins had increased stability. Toxicity associated with mutant FUS was not caused by increased FUS activity.	(Sharma et al., 2016)
<i>FUS</i> (R521C, <i>FUS<sub>NLS</sub></i> )	Insertion - transient	Intracerebral AAV injection	Mutant FUS protein was insoluble and accumulated in the axons and dendrites of neurons. It was in this location that it was thought to play an early role in neurodegeneration as the mutant FUS may attract RNA-binding proteins into permanent inclusions, therefore disrupting RNA metabolism.	(Verbeeck et al., 2012)



Table 1.1 continued...

Gene (mutation)	Model type	Method	Main finding	Reference
<i>SOD1</i>	Deletion	Electroporation of SOD1-targeted plasmid into embryonic stem cells. Homologous recombination resulted in homozygous SOD1 knock-out mice.	SOD1 was not required for the normal development and function of neurons, but was needed for neuron survival after injury and during cell stress (scavenge potentially toxic superoxide radicals). Absence of SOD1 function did not single-handedly cause motor neuron death	( <a href="#">Reaume et al., 1996</a> )
<i>SOD1(A4V, G93A)</i>	Insertion - over-expression	Plasmid pronuclear microinjection	Elevated levels of mutant SOD1 produced a gain-of-function toxic effect through activation of oxidative damage pathway. This resulted in spinal cord motor neuron loss, limb paralysis, and premature death in mice.	( <a href="#">Gurney et al., 1994</a> )
<i>SOD1 (G86R)</i>	Insertion - over-expression	Plasmid pronuclear microinjection	Astrocyte-specific expression of mutant SOD1 alone was insufficient to cause motor neuron death. Astrocytes may contribute to disease progression once other cell types initiate disease.	( <a href="#">Gong et al., 2000</a> )
<i>TARDBP</i>	Knock-out	Cre-LoxP recombination	TDP-43 is important in maintaining normal neuronal activity. Loss of TDP-43 in post-natal motor neurons results in disruption of axonal retrograde transport and age-dependent deterioration of motor function.	( <a href="#">Iguchi et al., 2013</a> )
<i>TARDBP (G348C, A315T)</i>	Insertion - moderate expression	BAC site-directed mutagenesis followed by embryonic microinjection of BAC fragments.	Moderate expression of mutant TDP-43 was sufficient to elicit formation of ubiquitinated mutant TDP-43 cytoplasmic aggregates in motor neurons and neurofilament aggregates in cell body and axon. Neuroinflammation evident through astrogliosis, occurred before behavioural abnormalities (context and spatial learning and memory) were detected.	( <a href="#">Swarup et al., 2011</a> )
<i>TARDBP (M337V)</i>	Insertion - transient over-expression	Intrastriatal AAV injection	Mutant TDP-43 selectively accumulated in neurons rather than glial cells, hinting that both cell types have different abilities and/or strategies to cope with mutant proteins. It was noted that glial cells have higher proteasome activity and this was likely the reason for the difference in expression levels. Striatal expression of mutant TDP-43 caused a severe phenotype with significantly impaired movement and premature death.	( <a href="#">Yan et al., 2014</a> )

This table provides a non-exhaustive selection of transgenic mouse models to date. Deletion models refer to mice in which an ALS-linked gene has been removed or changed such that it no longer expresses endogenous levels of its respective protein. Insertion and knock-in mouse models carry an ALS-linked gene and most commonly over-express its respective protein. In transient models, an ALS-linked gene is not stably integrated into the mouse's genome and is therefore most strongly expressed for a short period of time post transfection. AAV = adeno-associated virus, BAC = bacterial artificial chromosome, RAN = repeat-associated non-ATG-dependent, CNS = central nervous system.

### 1.2.2 *CCNF*

A recent gene discovery at Macquarie University identified *CCNF* mutations in patients with fALS and FTD (Williams et al., 2016). *CCNF* is located on chromosome 16 in humans, and on chromosome 17 in mice. It encodes the ubiquitously expressed cyclin F protein, also known as F-box only 1 (Fbxo1) protein (Bai et al., 1994). Cyclin F (figure 1.2) includes two nuclear localisation sequences (NLS), an F-box domain, a cyclin domain, and a Proline (P), Glutamic acid (E), Serine (S), Threonine (T) rich (PEST) region which is located at the carboxyl terminal (Bai et al., 1994; Galper et al., 2017).

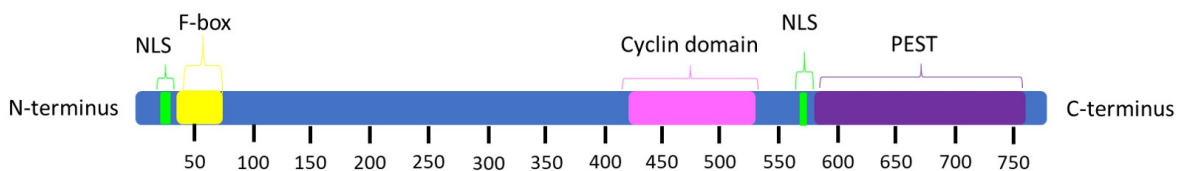


FIGURE 1.2: **Cyclin F protein structure.** The blue horizontal bar represents the 777 amino acid long, cyclin F sequence. Coloured boxes represent the functional regions on the protein, and the black numbers along the bottom of the blue bar are the amino acid count.

The cyclin domain recruits and binds substrates and contains functional D-boxes necessary for degradation of cyclin F itself during the cell cycle. Likewise, the PEST region signals proteolysis of cyclin F during cell cycle, and also after DNA damage. Cyclin F is expressed in the centrosome during the G2 phase of the cell cycle (D'angioloella et al., 2013), nucleus in post-mitotic cells, the perinuclear space (Bai et al., 1994), and can be translocated to the cytoplasm if bound to mutant cyclin B1 (Kong et al., 2000).

In general, the functions of cyclin F are to drive cell cycle progression (Burdova et al., 2019), mediate protein degradation, regulate dNTP production, centrosome duplication, and spindle assembly (D'angioloella et al., 2013), and to suppress DNA replication, which ultimately affect genome stability and protein homeostasis. These functions are predominantly mediated through ubiquitin-mediated proteolysis (Galper et al., 2017). Unlike other cyclins, cyclin F is also an F-box protein containing a structural and functional F-box domain. This domain links two other proteins, S-phase kinase-associated protein 1 (Skp1) and Cull1, to cyclin F, and together they form an SCF (Skp1-Cul1-F-box) complex which acts as an E3 ubiquitin ligase (Burdova et al., 2019; D'angioloella et al., 2013). E3 ubiquitin ligases are the final ligase in an enzymatic pathway, that add ubiquitin tags to specific proteins and signal their degradation via the UPS.

The mechanisms by which the ten reported ALS/FTD-linked *CCNF* mutations (Galper et al., 2017), lead to neurodegeneration are still largely unknown. One mutation that segregated in an extended family (an amino acid change from a Serine (S)

residue to a Glycine (G) residue at position 621, denoted by  $CCNF^{S621G}$ ), has been extensively studied ([Hogan et al., 2018, 2017](#); [Lee et al., 2018](#); [Williams et al., 2016](#)). In the mouse neuron-like cell line, neuro-2a,  $CCNF^{S621G}$  expression led to increased Lys48-ubiquitinated proteins despite proteasome function being unaffected ([Lee et al., 2018](#)). This suggested elevated E3 ubiquitin ligase activity and impaired enzymatic processes or transportation of proteins to the proteasome for degradation. In a human neuroblastoma cell line, SH-SY5Y,  $CCNF^{S621G}$  was found to alter levels of autophagy markers, alluding to functional impairment of the autophagy protein degradation pathway. In a mouse neuron-like cell line, NSC-34,  $CCNF^{S621G}$  impaired UPS-mediated protein degradation and increased levels of ubiquitinated proteins, likely due to abnormal protein ubiquitination and/or transport to proteasome ([Williams et al., 2016](#)).

So far, the only animal species in which the effects of  $CCNF^{S621G}$  have been studied is zebrafish. This original study reported transient over-expression of  $CCNF^{S621G}$  in the CNS of zebrafish ([Hogan et al., 2017](#)). Researchers found that zebrafish expressing mutant cyclin F carried elevated levels of caspase 3 (an enzyme involved in protein cleavage and executing apoptosis pathways), suffered increased cell death in the spinal cord, motor neuron axonopathy, abnormal motor neuron branching, and decreased photomotor response. Later attempts to generate a stable zebrafish line proved unsuccessful due to embryonic lethality ([Hogan et al., 2018](#)).

The mechanisms by which  $CCNF$  mutations lead to motor neuron degeneration remain poorly understood. The cell line and zebrafish studies supported the utility of using mutant  $CCNF$  to model ALS, to further investigate pathogenic mechanisms including UPS dysfunction and aberrant protein degradation. Accordingly, a novel transgenic mouse model carrying  $CCNF^{S621G}$  was created through CRISPR-Cas9 genome editing. A CRISPR-Cas9 gRNA, targeted to the *Ccnf* gene in a mouse embryo's genome, was used to create a double strand break in the gene. At this break site, a DNA repair template containing the mouse equivalent of the human mutant S621G sequence was inserted into the genome via homology dependent repair. From this, a CRISPR- $CCNF^{S621G}$  heterozygous mouse line was raised, and then bred to homozygosity. Preliminary behavioural studies showed the mutant mice had cognitive impairments but no significant motor changes, and initial proteomics analysis predicted increased neurite and axon degeneration. Critically, no assessment has yet been performed to determine whether this mouse develops pathological features associated with ALS.

All experimental models have advantages and disadvantages. As previously mentioned,  $CCNF$  had already been studied in zebrafish and cell models, so the effects of  $CCNF$  in a mammalian animal model still required investigation. Mammalian animals like mice have evolved to carry more physiological and anatomical similarities to humans than zebrafish have ([Barré-Sinoussi and Montagutelli, 2015](#)), for example their highly regulated and integrated central nervous systems. This makes mice a good species to study the greater

disease complexities and molecular pathway interactions in once initial disease studies have been performed in more simple animal systems like zebrafish.

### 1.3 Aims

The CRISPR-*CCNF*<sup>S621G</sup> mouse is among the first ALS mouse models to be developed using CRISPR technology. Characterisation of this mouse is therefore essential to establish the potential of this model for the assessment of disease mechanisms and longer-term pre-clinical studies. At the commencement of this study, the mechanisms by which mutant *CCNF* leads to neurodegeneration were yet to be studied in a mammalian system. Neuronal pathology was yet to be studied and more specifically, it was unknown whether mutations cause build-up of ubiquitinated proteins similar to that witnessed in zebrafish and cell models (Hogan et al., 2017). It was also unclear if disease severity differed between *CCNF*<sup>S621G</sup> homozygous and heterozygous mice and whether mutant cyclin F is expressed at comparable endogenous levels to the wild-type protein.

Therefore, **the overall aim** of this thesis was to assess the impact of *CCNF*<sup>S621G</sup> and subsequently the expression of mutant cyclin F, on ALS/FTD-associated cellular pathology in the novel CRISPR-*CCNF*<sup>S621G</sup> mouse model. The experimental approaches that were taken to do this, include histology and protein quantification (Figure 1.3).

In histology, mouse model and wild-type (WT) mouse brain and spinal cord tissues were processed, embedded and sectioned, and the expression of cyclin F along with other ALS/FTD-related proteins was characterised. Localisation changes were validated, interactions between ALS/FTD-related proteins and cyclin F were detected, and levels of motor neuron death were gauged, using immunofluorescence and Nissl staining and microscopy.

For protein quantification, protein lysates were collected from mouse model and WT mouse brain tissue and subjected to Western blot and mass spectrometry (MS) analysis, followed by in silico analysis of the output data. Additionally, real-time quantitative polymerase chain reaction (RT-qPCR) was employed to quantify *CCNF* expression levels.

In all analyses, the CRISPR-*CCNF*<sup>S621G</sup> mouse cohorts were compared to a wild-type cohort, and the data interpreted with regard to what is known about *CCNF*<sup>S621G</sup> and ALS/FTD pathology, so as to determine if the model accurately and reliably recapitulates features of disease at molecular and cellular levels. It was hypothesised the *CCNF*<sup>S621G</sup> models would show characteristic ALS/FTD cellular pathologies such as TDP-43 mislocalisation and aggregation, decreased lumbar spinal cord motor neurons, and ubiquitinated protein inclusions, and would therefore be the first mutant *CCNF* CRISPR-Cas9 mouse model of ALS/FTD that could potentially be used for pre-clinical testing including the efficacy of potential treatments.

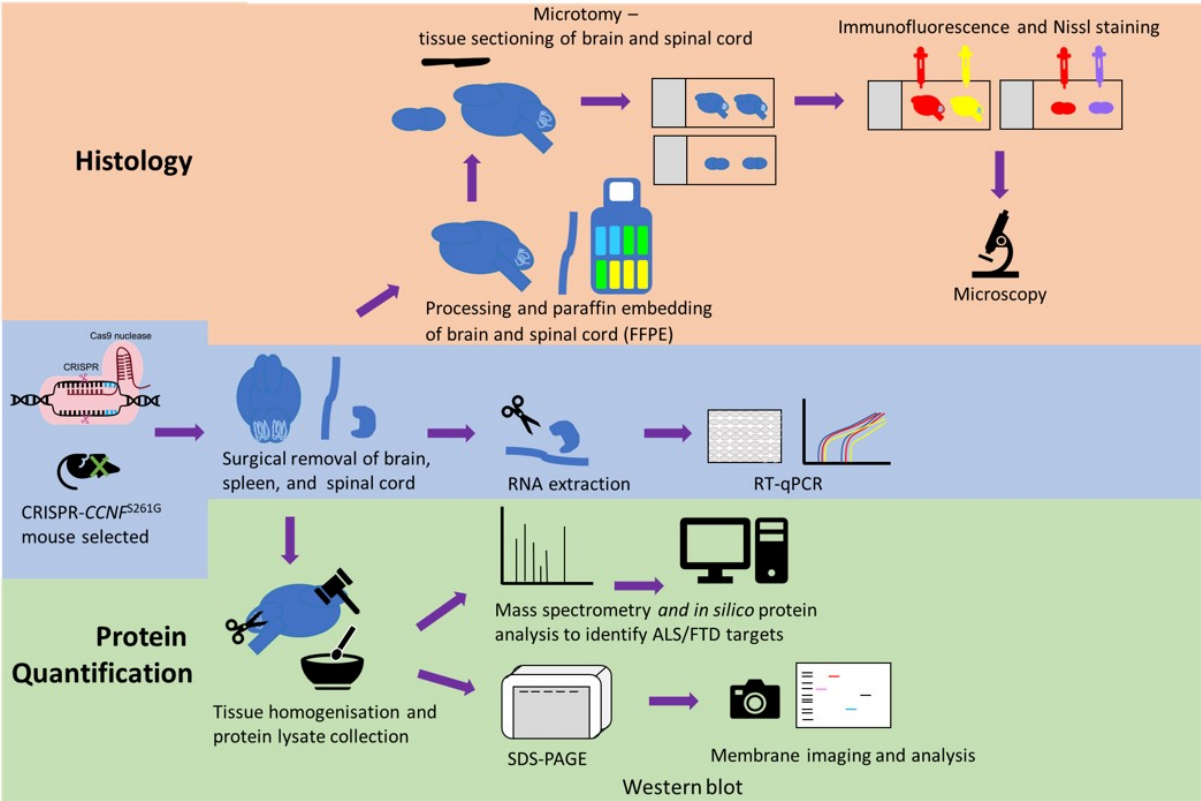


FIGURE 1.3: **Project methodology overview.** Schematic representation of the dual part methodological approach that was undertaken during the project.



*“Some things you know about, you know what the ingredients are  
—maybe not all of them. But it’s up to you to put in the amount.”*

- Judi Dench

# 2

## Subjects & materials

### 2.1 Mouse model cohorts

Tissue samples from a total of nine, six-month-old mice were used in this project. Three of the mice were WT, three mice were heterozygous for the  $CCNF^{S621G}$  mutation and three were homozygous for the  $CCNF^{S621G}$  mutation (table 2.1). The mice were grown and housed at Western Sydney University before being culled, dissected and tissues (brain, spinal cord, spleen, and liver) fresh frozen.

TABLE 2.1: **Mouse cohorts**

<b>Wild-type</b>	<b>Heterozygous <math>CCNF^{S621G}</math></b>	<b>Homozygous <math>CCNF^{S621G}</math></b>
#4 (M)	#9 (F)	#3 (M)
#7 (F)	#14 (F)	#8 (F)
#15 (F)	#16 (F)	#17 (F)

M: male, F: female.

## 2.2 Chemicals, reagents, materials, and kits

Table 2.2 contains chemicals, reagents and solutions that were used in all histology, biochemical and proteomic experiments unless otherwise stated. Table 2.3 lists the details of each commercial kit used in this thesis.



TABLE 2.2: Chemicals, reagents and materials

Product	Company	Composition
<b>Genotyping</b>		
Agarose powder	Bioline	
DNA cleanup solution	Promega, NEB, Merck Millipore	0.2 $\mu$ L TSAP, 0.3 $\mu$ L EXoI, 4.6 $\mu$ L Milli-Q <sup>®</sup> H <sub>2</sub> O
MyTaq <sup>TM</sup> DNA polymerase	Bioline	2X
SYBR <sup>TM</sup> safe DNA gel stain	ThermoFisher	
Tris/Borate/EDTA (TBE) buffer	Sigma-Aldrich	10 mM Tris-HCl, 1 mM disodium EDTA, pH 8.0
1.5% agarose gel	Bioline, Sigma-Aldrich	50 mL: 0.75g agarose powder, 50 mL TBE buffer, 5 $\mu$ L SYBR <sup>TM</sup> safe
<b>Tissue processing</b>		
Ethanol	Chem-Supply, Merck Millipore	100% ethanol, 70% ethanol diluted with Milli-Q <sup>®</sup> H <sub>2</sub> O
Paraformaldehyde (PFA)	ProSciTech	16% paraformaldehyde (formaldehyde) aqueous solution diluted to 4% with phosphate buffered saline (PBS)
Xylene	Chem-Supply	100%
<b>Tissue staining</b>		
Blocking solution	Vector laboratories, Astral Scientific, Sigma-Aldrich	5% normal goat serum (NGS), PBS (phosphate-buffered saline)/T (Tween 20)
Citrate Buffer Antigen Retriever (low pH, 1X)	Sigma-Aldrich, Merck Millipore	500 mL: 50 mL Citrate Buffer Antigen Retriever, 450 mL Milli-Q <sup>®</sup> H <sub>2</sub> O pH 6
Cresyl violet solution (10X) (Nissl stain stock, 10X)	Sigma-Aldrich	0.2 g cresyl violet-acetate dissolved in 150 mL deionised water
Cresyl violet solution (1X) (Nissl stain, 1X)	Sigma-Aldrich	30 mL nissl stain stock solution, 300 mL buffer solution (282 mL 0.1 M acetic acid and 18 mL 0.1 M sodium acetate)
DAPI Prolong Gold Antifade Mountant	ThermoFisher	
DPX mountant	Sigma-Aldrich	
EnVision <sup>TM</sup> FLEX Target Retrieval Solution (high pH, 1X)	Dako	500 mL: Tris/EDTA, pH 9
EnVision <sup>TM</sup> FLEX Target Retrieval Solution (low pH, 1X)	Dako	500 mL: Citrate buffer, pH 6.1
Ethanol	Chem-Supply, Merck Millipore	100% ethanol, 95% ethanol and 70% ethanol diluted with Milli-Q <sup>®</sup> H <sub>2</sub> O
High pH antigen retrieval buffer (10X prepared)	Merck Millipore, AppliChem, Sigma-Aldrich	12.1 g Tris, 3.7 g EDTA, 1 L Milli-Q <sup>®</sup> H <sub>2</sub> O, 0.005% Tween 20, pH9
High pH antigen retrieval buffer (1X prepared)	Merck Millipore, AppliChem, Sigma-Aldrich	100 mL 10X prepared high pH antigen retrieval buffer, 900 mL Milli-Q <sup>®</sup> H <sub>2</sub> O, pH9
Low pH antigen retrieval buffer (10X prepared)	Merck Millipore, Chem-Supply, Sigma-Aldrich	29.4 g trisodium citrate (dihydrate), 1 L Milli-Q <sup>®</sup> H <sub>2</sub> O, 0.005% Tween 20, pH6
Low pH antigen retrieval buffer (1X prepared)	Chem-Supply, Sigma-Aldrich	100 mL 10X prepared low pH antigen retrieval buffer, 900 mL Milli-Q <sup>®</sup> H <sub>2</sub> O, pH6
PBS	Astral Scientific, Merck Millipore	1 L: 1 PBS tablet (pH 7.4) dissolved in 1 L Milli-Q <sup>®</sup> H <sub>2</sub> O
PBS/T	Astral Scientific, Sigma-Aldrich, Merck Millipore	1 L: 1 PBS tablet (pH 7.4) dissolved in 1 L Milli-Q <sup>®</sup> H <sub>2</sub> O and 0.001 % tween 20

Table 2.2 continued...

<b>Protein lysate collection</b>		
Complete RIPA buffer	Sigma-Aldrich, Chem-Supply, BDH laboratory supplies	100 uL plus phospho stop (10x), 100 uL complete protease inhibitor (7x), 800 uL RIPA buffer
Dulbecco's Modified Eagle's Medium (DMEM)	Sigma-Aldrich	4500 mg/L glucose, L-glutamine, sodium pyruvate, sodium bicarbonate pH 7.2
DPBS solution	ThermoFisher	
FBS (Fetal bovine serum)	ThermoFisher	
RIPA buffer	Sigma-Aldrich, Chem-Supply, BDH laboratory supplies	50 mM Trizma HCL pH 7.4, 150 mM NaCl, 0.5% sodium deoxycholate, 1% Triton X, 0.1% sodium dodecyl sulphate
Trypsin-EDTA	Sigma-Aldrich	10X, sterile-filtered, 5.0 g porcine trypsin, 2 g EDTA • 4Na per litre of 0.9% sodium chloride
<b>Western blot</b>		
Bio-Safe <sup>TM</sup> Coomassie stain	Bio-Rad	
Blocking buffer	LiCor	1:1 odyssey blocking buffer (OBB) to 1X TBS
Blot absorbent filter paper	Bio-Rad	
Immobilon <sup>TM</sup> -FL PVDF membrane	Merck Millipore	
Laemmli sample buffer (4X)	Bio-Rad	
NuPAGE reducing agent (10X)	Invitrogen	
Ponceau S solution	Sigma-Aldrich	0.1% w/v Ponceau S solution in 5% acetic acid
Precision plus protein <sup>TM</sup> dual colour standard	Bio-Rad	
Running buffer (1X)	Bio-Rad, Merck Millipore	1 L: 100 mL 10X Tris/Glycine/SDS dissolved in 900 mL Milli-Q <sup>®</sup> H <sub>2</sub> O
Sodium dodecyl sulfate (SDS) polyacrylamide gel, 4-15% criterion <sup>TM</sup>	Bio-Rad	
TGX <sup>TM</sup> precast gel		
Transfer buffer (1X)	Bio-Rad, Merck Millipore	1.5 L: 150 mL 10X Tris/Glycine Buffer stock and 300 mL 100% methanol dissolved in 1050 mL Milli-Q <sup>®</sup> H <sub>2</sub> O
Transfer buffer (1X, prepared)	Sigma-Aldrich, Merck	1 L: 72 g glycine, 15.14 g tris(hydroxymethyl)aminomethane dissolved in 1 L Milli-Q <sup>®</sup> H <sub>2</sub> O
Tris-buffered saline (TBS)	AMRESCO, Chem-Supply	Tris-HCl (pH 7.5), NaCl
<b>Quantitative polymerase chain reaction</b>		
QIAzol <sup>®</sup> lysis reagent	QIAGEN	1 mL per tissue sample, contains phenol and thiocyanate compounds

TABLE 2.3: Kits

Name	Catalogue No.	Brand	Experiment
Allprep DNA/RNA mini kit	80204	QIAGEN	DNA extraction
Pierce BCA Protein Assay Kit	PIE23225	ThermoFisher	Western blot
TaqMan <sup>TM</sup> <i>CCNF</i> Gene Expression Assay, VIC primer	4448489	ThermoFisher	qPCR
TaqMan <sup>TM</sup> <i>ACTB</i> Gene Expression Assay, FAM primer	4352933E	ThermoFisher	qPCR
RNeasy <sup>®</sup> mini kit part 1 and 2	74104	QIAGEN	qPCR

## 2.3 Antibodies

Details of the antibodies used in either IF staining or Western blot can be found in table 2.4. Greater details of the combinations and the experiments the antibodies were used in can be found in tables 3.7 and 3.8.

TABLE 2.4: **Antibodies, their concentrations and applications**

Antibody	Species	Specificity	Dilution(application)	Catalogue No.	Brand
<b>Primary</b>					
Cyclin F	Mouse	Monoclonal	1:50, 1:100 and 1:200(IF), 1:100 and 1:500(WB)	SC-515207	Santa Cruz
Cyclin F	Rabbit	Polyclonal	1:50 and 1:100(IF), 1:500(WB)	SC-952	Santa Cruz
Cyclin F	Rabbit	Polyclonal	1:500 and 1:750(WB)	PA5-36049	ThermoFisher
Cyclin F blocking peptide	Mouse	Monoclonal	1:40 and 1:100(IF)	SC-515207 P	Santa Cruz
Cyclin F	Rabbit	Polyclonal	1:50, 1:100, and 1:200(IF)	LS-C351947	LifeSpan Bio-Sciences
NeuN	Mouse	Monoclonal	1:25, 1:50 1:100, and 1:200(IF)	MAB377	Merck Millipore
Phospho TDP-43	Rabbit	Polyclonal	1:500(IF)	pS409/410-2	CosmoBio
TDP-43	Mouse	Monoclonal	1:100(IF)	H00023435-M01	Abnova
TDP-43	Rabbit	Polyclonal	1:500(IF), 1:1,000(WB)	10782-2-AP	ProteinTech
GAPDH	Mouse	Monoclonal	1:5,000 and 1:6,000(WB)	60004-1-Ig	ProteinTech
Ubiquitin	Rabbit	Polyclonal	1:500(IF, WB)	Z0458	Dako
<b>Secondary (IgG)</b>					
AlexaFluor 488 anti-mouse	Goat		1:250(IF)	A11001	Invitrogen
AlexaFluor 488 anti-rabbit	Goat		1:250(IF)	A11008	Invitrogen
AlexaFluor 555 anti-mouse	Goat		1:250(IF)	A21422	Invitrogen
AlexaFluor 647 anti-rabbit Plus	Goat		1:250(IF)	A32733	Invitrogen
IRDye 680LT Donkey anti-Mouse IgG	Donkey	anti-Donkey	1:20,000(WB)	LCR-926-68022	LiCor/ Millenium Science
IRDye 800CW Donkey anti-Mouse IgG	Donkey	anti-Donkey	1:20,000(WB)	LCR-926-32212	LiCor/ Millenium Science
IRDye 680LT Donkey anti-Rabbit IgG	Donkey	anti-Donkey	1:20,000(WB)	LCR-926-68023	LiCor/ Millenium Science
IRDye 800CW Donkey anti-Rabbit IgG	Donkey	anti-Donkey	1:20,000(WB)	LCR-926-32213	LiCor/ Millenium Science

IF: immunofluorescence staining, WB: Western blot.



*“And like Alice, she went down the rabbit hole....”*

# 3

## Methods

The following chapter outlines the methods and approaches that were used to assess ALS/FTD-associated molecular and cellular pathologies in the CRISPR-*CCNF*<sup>S621G</sup> mouse model.

### 3.1 CRISPR-*CCNF*<sup>S621G</sup> mouse model genotyping

To confirm that the CRISPR-*CCNF*<sup>S621G</sup> mouse model cohorts and controls were 1) heterozygous, 2) homozygous, and 3) WT, genotyping was performed for a representative mouse from each cohort.

#### 3.1.1 DNA extraction

DNA was extracted from 20 mg spleen tissue from CRISPR-*CCNF*<sup>S621G</sup> mice #14(Het) and #3(Homo), and #4(WT), using the AllPrep DNA/RNA mini kit (QIAGEN) and a protocol adapted from the AllPrep DNA/RNA mini handbook (QIAGEN (2005), accessed <https://www.qiagen.com/au/resources/resourcedetail?id=bbd50261-3b80-4657-ad58-6a5a97b88821&lang=en>). To start, each spleen sample was homogenised in 600  $\mu$ L buffer RLT (1%  $\beta$ -mercaptoethanol) using the omni (TH) tissue homogeniser (Omni International). Tissue lysates were left to settle (5 min), and then each was transferred to an AllPrep DNA spin column placed in a 2 mL collection tube, and centrifuged at 13,000 g for 45 s. The remaining protocol steps were followed as per

manufacturer’s instructions. Lastly, DNA purity and quantity was measured using the QIAxpert spectrophotometer (QIAGEN).

### 3.1.2 Primer design

Gene-specific primers for the mouse *Ccnf* S621G gene mutation were required to validate CRISPR-*CCNF*<sup>S621G</sup> mice genotypes. To confirm protein sequence conservation at peptide 621 between human (NP\_001752.2) and mouse (NP\_031660.3) cyclin F, protein sequences were obtained from NCBI homologue (accessed <https://www.ncbi.nlm.nih.gov/homologene>), and aligned using Clustal Omega (EMBL-EBI, accessed <https://www.ebi.ac.uk/Tools/msa/clustalo/>). Genomic and coding DNA (cDNA) reference sequences were obtained for the human (GRCh37/hg19, NM001761.2) and mouse (GRCm38/mm10, NM007634.4) *CCNF* gene from The University of California, Santa Cruz (UCSC) GenomeBrowser (accessed <https://genome.ucsc.edu/cgi-bin/hgGateway>). The cDNA sequences were also aligned using Clustal Omega to determine the affected cDNA position, and corresponding exon in the mouse *CCNF* gene. Primer sequences were designed to target exon 17 using ExonPrimer software (Institute of Human Genetics, Helmholtz Center Munich, accessed <https://ihg.helmholtz-muenchen.de/cgi-bin/primer/ExonPrimerUCSC.pl?db=mm10&acc=ENSMUST00000115390.4>). A primer pair that generates a product less than 500 base pairs (bps) was chosen for downstream Sanger sequencing. The specificity of the primer pair across the mouse genome was confirmed using the UCSC *in silico* PCR tool (accessed <https://genome.ucsc.edu/cgi-bin/hgPcr>), with the result of a single product. Universal M13 primer sequences (red text in table 3.1) were added to the primers to improve efficiency of sequencing. The primers (table 3.1) were then synthesised by Sigma-Aldrich.

TABLE 3.1: **Genotyping primers**

Primer name	5'-3' sequence	PCR product size (bp)
CCNF_mouse_exon16_F	TGTA <del>AAACGACGGCCAGT</del> GATAGC ATTACGTTGGCTCTCC	298
CCNF_mouse_exon16_R	<del>CAGGAAACAGCTATGAC</del> CCTCAGAT CATGTGTCACCCG	

Note: the red text in the sequence is the M13 primer and the black text is the *Ccnf* specific sequence.

### 3.1.3 Primer optimisation

Prior to using the custom designed primers for mouse genotyping, optimal PCR reaction conditions were determined. An optimisation reaction was performed according to the reaction and thermocycling conditions in table 3.2. Briefly, eight 10  $\mu$ L reactions

were prepared using control #4(WT) mouse DNA and were PCR amplified with various annealing temperatures ( $T_A$ ).

TABLE 3.2: **Primer optimisation PCR reaction mixture and thermocycling conditions**

Reagent	1X Volume ( $\mu$ l)	Temperature	Time	Cycles	$T_A$ Gradient
Milli-Q <sup>®</sup> H <sub>2</sub> O	3.2	95 °C	3 min	1X	53.4
My <i>Taq</i> <sup>™</sup> DNA polymerase	5.0				55.7
10 mM F primer	0.4	94 °C	15 sec	35X	58.3
10 mM R primer	0.4	50–72 °C ( $T_A$ )	30 sec		61.0
20 ng #4(WT) DNA	1.0	72 °C	15 sec		63.7
Total	10.0	72 °C	5 min	1X	66.1
		15 °C	Hold		68.0
					69.4

To visually identify whether *Ccnf* had been successfully amplified, the PCR products were electrophoresed on agarose gel. 2  $\mu$ L each PCR product was loaded into a 1.5% agarose gel alongside EasyLadder I (Bioline) which would aid the determination of product size. The electrophoresis was run (120 V, 30 min), then the gel was imaged and analysed with the Gel Doc EZ System (Bio-Rad) and Image Lab software (version 6.0.1, Bio-Rad). The optimal PCR reaction condition was determined by the the annealing temperature that generated the clearest PCR product at the expected size.

### 3.1.4 DNA amplification

One representative DNA sample from each mouse cohort, and a template control were PCR amplified using the optimised annealing temperature (table 3.3). PCR products were validated by agarose gel electrophoresis as described in section 3.1.3, followed by EXoSAP purification with DNA cleanup solution.

TABLE 3.3: **PCR DNA amplification reaction mixture and thermocycling conditions**

Reagent	1X Volume ( $\mu$ l)	Temperature	Time	Cycles
Milli-Q <sup>®</sup> H <sub>2</sub> O	7.4	95 °C	3 min	1X
My <i>Taq</i> <sup>™</sup> DNA polymerase	10.0			
10 mM F primer	0.8	94 °C	15 sec	35X
10 mM R primer	0.8	68 °C	15 sec	
20 ng DNA	1.0	72 °C	15 sec	
Total	20.0	72 °C	5 min	1X
		15 °C	Hold	

### 3.1.5 DNA sequencing and analysis

Amplified samples underwent Sanger sequencing (Macrogen, South Korea). Sequence data was analysed using Sequencher<sup>®</sup> v5.1 software (Gene Codes Corporation). Resultant sequence chromatograms were aligned to the reference *Ccnf* mouse genomic DNA sequence (NM007634.4) obtained above (section 3.1.2). Sequence chromatograms were then visually inspected and compared at the affected nucleotide position, to ensure the correct genotype was present in each sample.

## 3.2 CRISPR-*CCNF*<sup>S621G</sup> mouse model tissue sample preparation

### 3.2.1 Tissue fixation, processing, and embedding

Fresh-frozen spinal cord tissues from three WT, three heterozygous, and three homozygous, six-month-old CRISPR-*CCNF*<sup>S621G</sup> mice were cut into three parts: thoracic, lumbar, and sacral. These spinal cord tissues, and brain “hemispheres”<sup>1</sup> from the same mice, were then fixed in 4% PFA (overnight ~ 20 h, 4 °C). The tissues were washed in PBS (three 3 min washes, with gentle rocking), and incubated in 70% ethanol (overnight, 4 °C). The brain “hemispheres” and spinal cords were next processed using the Leica ASP200S ‘brain’ protocol (Table 3.4), were embedded in paraffin wax (Tissue-Tek TEC5 Tissue Embedding Console), and from then onwards termed formalin-fixed paraffin-embedded (FFPE) tissue.

TABLE 3.4: Tissue processing protocol

Stage	Solution	Cycle length
Dehydration	70 % ethanol	1 h
Dehydration	70 % ethanol	1 h
Dehydration	100 % ethanol	2 h
Dehydration	100 % ethanol	1 h
Dehydration	100 % ethanol	2 h
Dehydration	100 % ethanol	2 h
Tissue clearing	100 % xylene	2 h
Tissue clearing	100 % xylene	1 h
Tissue clearing	100 % xylene	2 h
Wax infiltration	Paraffin wax	2 h
Wax infiltration	Paraffin wax	1 h
Wax infiltration	Paraffin wax	2 h

<sup>1</sup>Due to previous uneven collection of a slice of brain tissue for proteomic analysis, the remaining amount and physical structure of the brain tissue hemisphere left, somewhat varied for each sample.

### 3.2.2 Tissue sectioning

To start with, FFPE brain tissue from three practice four-month-old C57 mice, a gift from Mr Rowan Radford, was sectioned for practice. The Mikrom HM325 Microtome was used to cut 5  $\mu\text{m}$  sagittal sections, of which four sections were mounted per glass microscope slide (Superfrost<sup>TM</sup> Plus microscope slides, ThermoFisher). Next, the FFPE brain and thoracic and lumbar spinal cord tissues from WT(#4) control mouse, were cut into 5  $\mu\text{m}$  sagittal and transverse sections, respectively. Forty-five slides carrying three consecutive brain sections were taken, followed by the collection of three sets of 15 slides, each carrying three brain sections that were 30  $\mu\text{m}$  apart. Specifically, one section was cut and mounted onto a slide in each of the three sets, followed by the cutting and disposal of three sections (figure 3.1). Throughout the brain tissue sectioning process, sections were observed under an Olympus CX23 light microscope to identify and note the sagittal location in the brain in reference to ‘The Mouse Brain in Stereotaxic Coordinates’ by [Franklin and Paxinos \(2007\)](#). This was essential as later immunofluorescence staining for ALS/FTD histopathologies would focus on assessing changes in the motor cortex and hippocampus — key areas affected in disease ([Al-Chalabi et al., 2012](#); [Mancuso and Navarro, 2015](#); [van Hummel et al., 2018](#)).

For the thoracic spinal cord, 42 slides carrying five consecutive spinal cord sections were collected. For the lumbar spinal cord, one section was cut and mounted onto a slide from each of the three sets, followed by the cutting and disposal of seven sections (therefore leaving 50  $\mu\text{m}$  between sections on the same slide) (figure 3.1). Five spinal cord sections were mounted onto each slide.

Finally, all FFPE CRISPR-*CCNF*<sup>S621G</sup> mouse model brain and lumbar spinal cord tissue samples were cut into 5  $\mu\text{m}$  sections using the microtome, and mounted onto glass slides. Three sets of eight slides were collected from each sample, with three brain sections and five spinal cord sections per slide, each section either 30  $\mu\text{m}$  or 50  $\mu\text{m}$  apart, as previously described.

## 3.3 CRISPR-*CCNF*<sup>S621G</sup> mouse model histopathology

### 3.3.1 Immunofluorescence staining

For immunofluorescence (IF) staining of slide-mounted FFPE mouse brain or spinal cord tissues, a two day protocol was used.

#### Day one:

Tissues were deparaffinised (30 min, 70 °C), followed by dehydration and rehydration

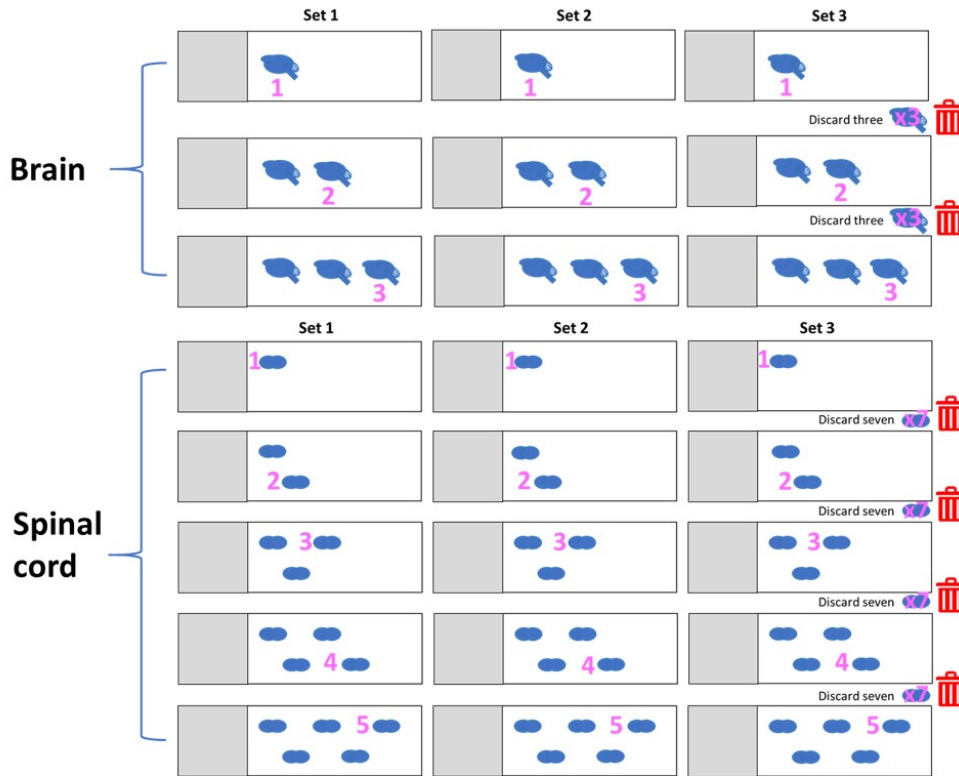


FIGURE 3.1: **Brain and spinal cord tissue section collection.** For brain section collection, three brain sections were cut and mounted onto a slide from each set followed by disposal of three sections. For spinal cord section collection, three spinal cord sections were cut and mounted onto a slide from each set followed by disposal of seven sections.

washes (Table 3.5). Tissues were then incubated in either preheated (96 °C) low pH or high EnVision<sup>TM</sup> FLEX Target Retrieval Solution (Dako) or antigen retrieval buffer (prepared) for 20 min, in a steaming waterbath (99 °C). The tissues were left to cool then washed three times for 5 min with PBS/T and gentle rocking. The slides were dried and a hydrophobic ring was drawn around each tissue section using a PAP pen (Sigma-Aldrich). Each brain section was blocked in 60  $\mu$ L blocking solution (5% normal goat serum in PBS/T), and each spinal cord section blocked in 30  $\mu$ L blocking solution (1 h, RT (room temperature)). Primary antibody solutions were prepared at various concentrations with blocking solution (table 3.7), and 60  $\mu$ L was applied to each brain section and 30  $\mu$ L applied to each spinal cord section. The tissues were incubated with the primary antibodies in a humidified chamber (overnight, 4 °C).

TABLE 3.5: Tissue washing steps for paraffin wax removal

Stage	Solution	Wash length
Dehydration	100 % xylene	10 min
Dehydration	100 % xylene	10 min
Dehydration	100 % ethanol	5 min
Dehydration	100 % ethanol	5 min
Rehydration	95 % ethanol	3 min
Rehydration	70 % ethanol	3 min
Rehydration	Water	3 min
Rehydration	Water	3 min

**Day two:**

Tissues were washed three times with PBS/T (5 min/wash with gentle rocking). Secondary antibody solutions at 1:250 dilution were prepared with blocking solution (table 3.7). The secondary antibody solutions were applied to the brain and spinal cord tissues, 60  $\mu$ L and 30  $\mu$ L, respectively, and the tissues were incubated in darkness in a humidity chamber (1 h, RT). Tissues were washed three times with PBS (5 min, in darkness with gentle rocking), slides were air dried (in darkness), and coverslipped with DAPI Prolong Gold Antifade Mountant.

To summarise, eight rounds of IF staining were performed following the two-day protocol. Six of this eight were optimisation rounds and two were for CRISPR-*CCNF*<sup>S621G</sup> mouse analysis. The various experimental combinations and conditions used in these rounds are listed in tables 3.6 and 3.7. In short, the first round of optimisation IF staining was a test to become accustomed to the IF protocol, the second round was used to determine which antigen retrieval buffer was optimal for staining on the CRISPR-*CCNF*<sup>S621G</sup> mouse model tissues so half of the samples were incubated in low pH antigen retrieval buffer (Dako) and half were incubated in high pH antigen retrieval buffer (Dako), and the third round was used to further ascertain the optimal concentration for mouse cyclin F (Santa Cruz) and rabbit TDP-43 (ProteinTech) antibodies on the CRISPR-*CCNF*<sup>S621G</sup> mouse model tissues so early slides (not whole sections) were used. Next, cyclin F blocking peptide (Santa Cruz) was applied to test the specificity of the mouse cyclin F (Santa Cruz) antibody to cyclin F protein, and then repeated with an increased concentration of cyclin F blocking peptide (1:40 as opposed to 1:100). A third cyclin F antibody (Lifespan Biosciences), specific to the mouse protein as opposed to human (the target of the previous two cyclin F antibodies), was trialled to establish if a better signal and image of cyclin F could be obtained.

TABLE 3.6: Summary of combinations and conditions used in each round of optimisation  
IF staining

Antigen retrieval buffer	Serum	Primary antibody	Conc.	Secondary antibody	Conc.	Samples
Low pH (Dako)	Goat	Rb cyclin F (Santa Cruz)	1:50	AlexaFluor 488 Goat anti mouse and AlexaFluor 647 Goat anti rabbit Plus	1:250	Four-month-old C57 mouse brain practice tissue
		Ms NeuN (Merck Millipore)	1:25			
		Rb cyclin F (Santa Cruz)	1:100			
		Ms NeuN (Merck Millipore)	1:50			
		Rb cyclin F (Santa Cruz)	1:200			
		Ms NeuN (Merck Millipore)	1:100			
Low and high pH (Dako)	Goat	Rb cyclin F (Santa Cruz)	1:50	AlexaFluor 488 Goat anti mouse and AlexaFluor 647 Goat anti rabbit Plus	1:250	CRISPR- <i>CCNF</i> <sup>S621G</sup> mouse #4 brain and spinal cord tissue
		Ms TDP-43 (Abnova)	1:100			
		Rb cyclin F (Santa Cruz)	1:100	AlexaFluor 647 Goat anti rabbit Plus	1:250	
		Ms cyclin F (Santa Cruz)	1:50	AlexaFluor 555		
		Ms cyclin F (Santa Cruz)	1:100	Goat anti mouse		
Low pH (prepared)	Goat	Ms cyclin F (Santa Cruz)	1:100	AlexaFluor 488 Goat anti mouse and AlexaFluor 647 Goat anti rabbit Plus	1:250	CRISPR- <i>CCNF</i> <sup>S621G</sup> mouse #17 brain and spinal cord tissue
		Rb TDP-43 (ProteinTech)	1:500			
		Ms cyclin F (Santa Cruz)	1:200			
		Rb TDP-43 (ProteinTech)	1:500			
Low pH (prepared)	Goat	Ms cyclin F (Santa Cruz)	1:200	AlexaFluor 488 goat anti mouse and AlexaFluor 647 Goat anti rabbit Plus	1:250	CRISPR- <i>CCNF</i> <sup>S621G</sup> mouse #3 brain and spinal cord tissues
		Rb TDP-43 (Protein Tech)	1:500			
		Ms cyclin F (Santa Cruz)	1:200			
		Rb TDP-43 (Protein Tech)	1:500			
		Ms cyclin F blocking peptide (Santa Cruz)	1:100			
		No primary				
Low and high pH (prepared)	Goat	Rb cyclin F (LifeSpan BioSciences)	1:50	AlexaFluor 488 goat anti mouse and AlexaFluor 647 Goat anti rabbit Plus	1:250	CRISPR- <i>CCNF</i> <sup>S621G</sup> mouse #15 brain and #4 spinal cord
		Ms NeuN (Merck Millipore)	1:100			
		Rb cyclin F (LifeSpan BioSciences)	1:100			
		Ms NeuN (Merck Millipore)	1:100			
		Rb cyclin F (LifeSpan BioSciences)	1:200			
		Ms NeuN (Merck Millipore)	1:200			
Low pH (prepared)	Goat	Ms cyclin F (Santa Cruz)	1:200	AlexaFluor 488 goat anti mouse and AlexaFluor 647 Goat anti rabbit	1:250	CRISPR- <i>CCNF</i> <sup>S621G</sup> mouse #15 brain and #4 spinal cord tissues
		Rb TDP-43 (Protein Tech)	1:500			
		Ms cyclin F (Santa Cruz)	1:200			
		Rb TDP-43 (Protein Tech)	1:500			
		Ms cyclin F blocking peptide (Santa Cruz)	1:40			
		No primary				

Further details on each antibody can be found in table 2.4

To investigate the presence of the ALS/FTD pathologies of TDP-43 mis-localisation and aggregation, ubiquitinated protein inclusions, and cyclin F changes and co-localisation with TDP-43 aggregates or other protein inclusions, half of the sections on one brain and spinal cord slide from each sample mouse, were stained with either mouse cyclin F (Santa Cruz) and TDP-43 (ProteinTech) or ubiquitin (Dako) and NeuN (Merck Millipore). Finally, a third low pH antigen retrieval buffer (Sigma-Aldrich) was used in IF staining to see if the clarity of cyclin F staining and imaging could be increased. Sections incubated in the Sigma-Aldrich antigen retrieval buffer were stained with TDP-43 (ProteinTech) and mouse cyclin F (Santa Cruz), or phosphoTDP-43 (CosmoBio) and mouse cyclin F (Santa Cruz), with the intention of observing the ALS/FTD pathology of phosphorylated TDP-43 aggregates. The specific regions of interest for pathological investigation in brain tissue sections included the motor cortex and hippocampus (part a) figure 3.2), whilst in the lumbar spinal cord tissue the ventral horn was of interest (part b) figure 3.2). ALS/FTD histopathologies have been identified in these regions in patients and animal models (Al-Chalabi et al., 2012), and therefore these regions, particularly the motor cortex and ventral horn — areas highly concentrated with motor neurons, are ideal for studying disease.

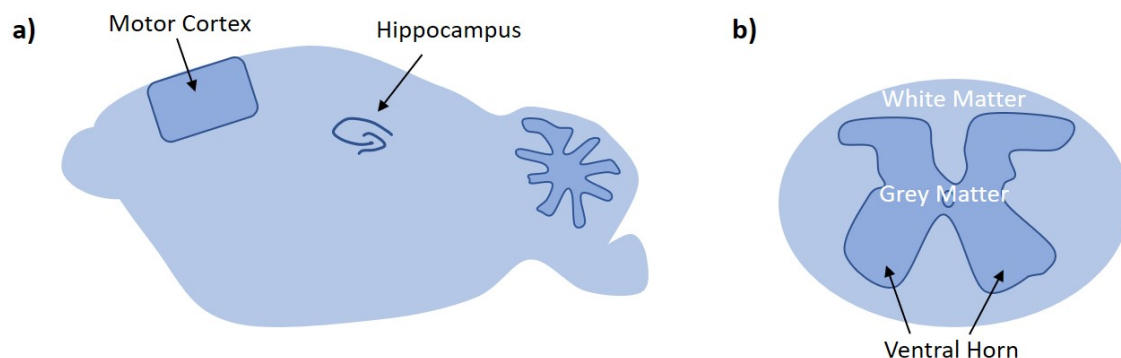


FIGURE 3.2: **Motor cortex, hippocampus, and ventral horn - regions of interest for histopathological analysis.** a) Representative illustration of a sagittal section of mouse brain tissue. Immunofluorescence staining for ALS/FTD histopathologies was performed on tissue at the level in the brain, where neurons in both the motor cortex and hippocampus could be imaged. Labelled arrows point to these regions. b) Representative illustration of a transverse section of mouse spinal cord tissue at the lumbar level. Immunofluorescence and Nissl (3.3.2) staining were performed at this level so motor neurons involved in limb function could be imaged.

TABLE 3.7: Summary of combinations and conditions used in each round of IF staining

Antigen retrieval buffer	Serum	Primary antibody	Conc.	Secondary antibody	Conc.	Samples
Low pH (prepared)	Goat	Ms cyclin F (Santa Cruz)	1:100	AlexaFluor 488 goat anti mouse and AlexaFluor 647 Goat anti rabbit	1:250	Brain and spinal cord tissue from each CRISPR- <i>CCNF</i> <sup>S621G</sup> mouse
		Rb TDP-43 (Protein Tech)	1:500			
		Ms NeuN (Merck Millipore)	1:200			
		Rb Ubiquitin (Dako)	1:500			
Low pH (Sigma-Aldrich)	Goat	Ms cyclin F (Santa Cruz)	1:100	AlexaFluor 555 goat anti mouse and AlexaFluor 488 Goat anti rabbit	1:250	
		Rb TDP-43 (Protein Tech)	1:500			
		Ms cyclin F (Santa Cruz)	1:100			
		Rb phosphoTDP-43 (CosmoBio)	1:500			

Further details on each antibody can be found in table 2.4

### 3.3.1.1 Confocal microscopy and analysis

All IF slides were visualised using the LSM880 confocal microscope (Zeiss) with 40x and 63x oil-immersion objective lenses, and images were captured with Zen 2.1 software (black edition). The antigen retrieval test set of slides were imaged with the same settings, as were the cyclin F antibody optimisation set of slides. During the first mouse cyclin F antibody analysis, the confocal microscope was set up such that DAPI and cyclin F (labelled with 488 nm secondary) were combined on the same track and TDP-43 (labelled with 647 nm secondary) was put onto a separate track. Confocal imaging that occurred after that point (blocking peptide, other cyclin F antibodies, ALS/FTD pathology IF staining, and Sigma-Aldrich antigen retrieval buffer IF staining) placed the antibodies with the closest excitation and emission wavelengths, on separate tracks to avoid signal cross-talk. In the ALS/FTD pathology IF staining experiments, the motor cortex and hippocampus in each brain section image and the ventral horn in each spinal cord section image were visually scanned for the presence of the ALS/FTD histopathologies mentioned previously. To distinguish if there was a difference in cyclin F expression between the three mouse cohorts, 20 spinal cord motor neurons in two spinal cord sections from each mouse and the slides that were incubated in Sigma-Aldrich antigen retrieval buffer, were imaged with the 63x objective lens and the same setting. The relative cyclin F staining intensity (in arbitrary units, a.u.) of each neuron was measured using Fiji (ImageJ version 1.52i) image processing software (Schindelin et al. (2012)) with a batch code (A.1.2.1). The average staining intensity per neuron in each mouse was calculated by averaging the relative intensity values from the 40 motor neurons measured, and the total staining intensity in each genotype was calculated by adding all the relative intensity values from the 120 motor neurons measured in each genotype (i.e. in each genotype: 3 mice x 40 motor neurons measured = 120 motor neurons)

### 3.3.2 Nissl staining

To trial the Nissl staining protocol, 19 thoracic spinal cord slides from WT(#4) mouse were selected, and deparaffinised and rehydrated as follows: xylene (5 min), xylene (5 min), 95% ethanol (3 min), 70% ethanol (3 min), Milli-Q<sup>®</sup> H<sub>2</sub>O (3 min). Tissues were stained in 1X cresyl violet solution (13 min, 60 °C oven), washed in Milli-Q<sup>®</sup> H<sub>2</sub>O (3 min), 70% ethanol (2 min), 95% ethanol (1 min) and dipped twice in 100% ethanol. Tissues were then washed in xylene (5 min) and coverslipped with DPX mounting media.

To see if lumbar spinal cord segments could be identified through Nissl staining, seven lumbar spinal cord slides from set one from WT(#4) mouse were selected and underwent the same protocol as above, except for 15 min stain in cresyl violet solution instead of 13 min.

For Nissl staining on lumbar segments three to five (L3-L5) from each CRISPR-*CCNF*<sup>S621G</sup> mouse, five slides carrying spinal cord tissues in these regions were selected. Slide selection was based on the shape of the spinal cord grey matter, observed under the Olympus CX23 light microscope, corresponding to L3-L5 in ‘The spinal cord: a Christopher and Dana Reeve Foundation text and atlas’ by [Anderson et al. \(2009\)](#). The tissues then underwent the previously described protocol with 15 min cresyl violet staining.

#### 3.3.2.1 Microscopy and motor neuron counting

Nissl stained spinal cord sections were imaged using the 5x and 10x objective lenses respectively, with the upright AxioImager.Z2 (Zeiss) microscope. ZEN 2 (blue edition) software was used to capture the images of both left and right sides of each tissue section.

To count the number of motor neurons present in each spinal cord section, only the motor neurons with clear Nissl staining, that were  $\geq 80 \mu\text{m}^2$  in size, and which sat below the highest point or top of the central canal in the ventral horn, were counted. This criteria was based on similar experiments conducted by [Zhao et al. \(2006, 2012\)](#) and [Devoy et al. \(2017\)](#). Fiji image processing software was utilised to determine whether or not a motor neuron fit this criteria. A batch processing code macro ([A.1.2.2](#)) was written and used to efficiently count the neurons that fit the set criteria. Threshold values used in the code were unique to each sample section and were either the automatic threshold generated or a slightly adjusted value that would detect visible neurons. The total number of motor neurons counted in both the left and right ventral horns from each mouse were compared by one-way ANOVA with multiple comparisons between each genotype ( $P < 0.05$ ).

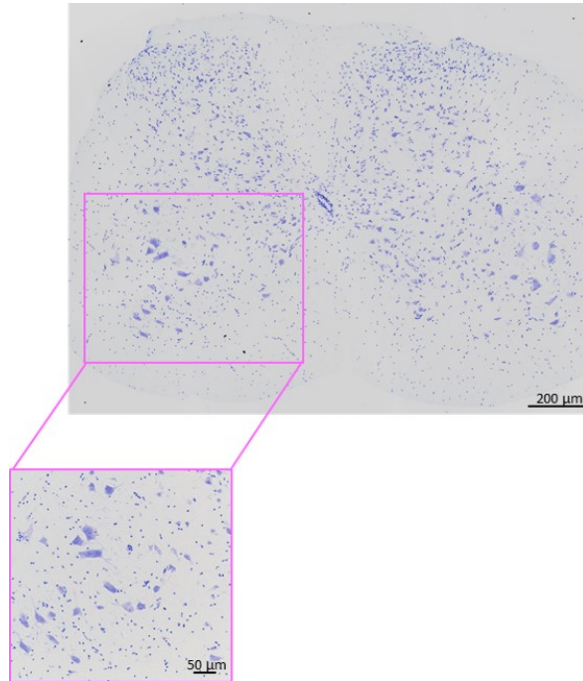


FIGURE 3.3: **Nissl stained ventral spinal cord region delimited for motor neuron counts.** Representative image of lumbar spinal cord segment L5 from WT mouse #7 (10x objective lens). Clearly stained motor neurons in both the left and right ventral horns below the highest point of the central canal, as delineated by the pink rectangle on the whole segment image, were counted.

## 3.4 CRISPR-*CCNF*<sup>S621G</sup> mouse model tissue protein analysis

### 3.4.1 Protein lysate collection

Total protein lysates were collected from fresh-frozen brain hemisphere tissue from each CRISPR-*CCNF*<sup>S621G</sup> and WT mouse by Ms Flora Cheng. Please refer to section [A.1.3.1](#) for the detailed protocol.

As part of *CCNF* antibody specificity testing in Western blot, protein lysates from HEK293T (human embryonic kidney) cells were collected. HEK293T cells (from American Type Culture Collection®) were cultured in DMEM supplemented with 10% FBS, in a T75 flask incubated at 37 °C in a humidified atmosphere with 5% CO<sub>2</sub>. For sub-culturing (every 3 days) and lysate collection once the culture reached 80% confluence, media was removed from the T75 flask, cells were washed with DPBS, were incubated with 1 mL warm trypsin (3 min, 37 °C) to dislodge them, then 5 mL warm DMEM supplemented with 10% FBS was added to the flask to neutralise trypsin activity. From this cell suspension, 200 μL was kept for sub-culturing whilst the remainder was transferred into a Falcon tube which was centrifuged at RT for 5 min at 1,000 rpm.

Supernatant was removed from the tube and the cell pellet was resuspended in DPBS. The number of cells in 200  $\mu\text{L}$  was quantified using the Sceptre<sup>TM</sup> 2.0 cell counter (Merck Millipore) and determined to be  $4.689 \times 10^5$  cells/mL. As 10 mL cell solution was initially removed from the T75 flask and 200  $\mu\text{L}$  was kept for sub-culturing this left 9.8 mL for lysate collection. So,  $4.689 \times 10^5$  cells/mL  $\times$  9.8 mL gave a total cell count of  $4.586 \times 10^6$  cells. The cells were pelleted again (5 min, 1,000 rpm, RT), the DPBS was poured off, and the pellet was resuspended in 250  $\mu\text{L}$  complete RIPA buffer. The suspension was transferred to 1.5 mL tube and mixed (45 min, 4 °C) on a rotator wheel (FINEPCR). The suspension was then centrifuged (10 min, 16,000 g, 4 °C), the supernatant (RIPA soluble fraction of protein lysate) was removed and collected.

Protein lysate from a neuro-2a cell culture was collected by Dr Shu Yang in a similar manner to the HEK293 cell protocol to provide another alternative lysate for antibody specificity testing.

To collect protein lysates from spleen, a small section of CRISPR-*CCNF*<sup>S621G</sup> mouse #4(WT) spleen was cut and weighed (0.165 g). Five times the weight of the spleen section in volume of RIPA buffer, was added to the spleen which was kept on ice. The spleen was sonicated (Sonic Rupto 250, Omni International): four rounds of 10 pulses at 30% power, with mechanical shearing with pipette tip in between. The lysate was ultracentrifuged (40 min, 45,000 rpm, 4 °C) and the supernatant was collected as protein lysate.

### 3.4.2 Mass spectrometry

The fractions of CRISPR-*CCNF*<sup>S621G</sup> mouse and WT brain protein lysate were analysed by mass spectrometry (MS) (1 h, Q-Exactive Plus mass spectrometer with UHPLC Dionex Ultimate 3000 RSLCnano), conducted by Dr Albert Lee and Ms Flora Cheng ([Lee et al., 2018](#)).

### 3.4.3 Protein analysis from mass spectrometry

The raw spectra files were processed by Dr Lee using Proteome Discoverer<sup>TM</sup> (version 2.3.0.523, ThermoFisher), to identify the total number of proteins in all samples and group them into each cohort. To verify the quality of the results, a principal component analysis (PCA) plot and sample abundance graphs were generated. I then performed the same quality verification steps to confirm the quality of the results (section [4.3.1.1](#)).

### 3.4.3.1 PANTHER

To begin with, all of the proteins identified from MS were filtered and sorted into lists using Microsoft Excel (version 1906, build 11727.20244). Proteins were filtered so that only those with high protein FDR (false discovery rate) confidence were selected for further filtering. The resulting proteins were then sorted using two stringent filtering criteria to reduce the large output. Firstly, “over-expression” criteria: “abundance ratio:(Hom/WT)” and “(Het/WT)”  $> 2$  (i.e. abundance ratios up-regulated), unique peptide count (number of different amino acid sequences identified in a peptide that are from a single protein group)  $\geq 2$ , and “abundance ratio: (Hom/WT)” larger than “(Het/WT)” (so increased function caused by mutant cyclin F could be investigated), were applied to the high FDR confidence proteins. Next, “under-expression” criteria: “unique peptides”  $\geq 2$ , “abundance ratio: (Het/WT)” and “(Hom/WT)”  $< 1$ , and “abundance ratio: (Hom/WT)” smaller than “(Het/WT)”, were applied to the high FDR confidence proteins. After each filtering criteria was applied, the ID’s for the proteins that fitted either were searched against *homo sapiens* on the PANTHER (protein analysis through evolutionary relationships) gene ontology (GO) web browser (Thomas et al. (2003), accessed <http://www.pantherdb.org/>). Here, the most common molecular functions were examined down to the level where individual genes/proteins were identified. These resulting protein IDs were then put into STRING (Search Tool for the Retrieval of Interacting Genes/Proteins) analysis (version 11, Szklarczyk et al. (2019), accessed [https://string-db.org/cgi/input.pl?sessionId=fhrt5G1u3DFe&input\\_page\\_active\\_form=multiple\\_identifiers](https://string-db.org/cgi/input.pl?sessionId=fhrt5G1u3DFe&input_page_active_form=multiple_identifiers)) to identify their direct and indirect protein-protein interactions. Additionally, the protein IDs that fitted each initial criteria were launched into GO enrichment analysis powered by PANTHER (Ashburner et al., 2000; Mi et al., 2018; The Gene Ontology Consortium, 2018), to gain knowledge on the biological processes they were involved in.

### 3.4.4 Western blot

To probe for and quantify specific proteins of interest, five Western blot experiments were run. The various antibody combinations, concentrations, and samples used in these experiments are noted in table 3.8. Prior to each Western blot experiment, the protein concentration of each lysate sample to be used, was measured via BCA assay (ThermoFisher) as described in A.1.3.1.

A two day Western blot protocol was followed for each run.

**Day one:**

Protein lysates were electrophoretically separated via SDS-PAGE. To do this, 15  $\mu\text{g}$  of each total protein lysate was combined with 5  $\mu\text{L}$  4X Laemmli sample buffer, 2  $\mu\text{L}$  10X NuPAGE<sup>®</sup> reducing agent, and Milli-Q<sup>®</sup> H<sub>2</sub>O to either a total volume of 20  $\mu\text{L}$  or 15  $\mu\text{L}$ , depending on the well size of the gel to be used. Sample protein (table 3.8) preparations were denatured (70 °C for 10 min), loaded into a midi or mini 4-15% criterion<sup>TM</sup> TGX<sup>TM</sup> precast gel next to 2  $\mu\text{L}$  precision plus protein<sup>TM</sup> dual colour standard, and the gel was run (95 V for 70 min or 105 V for 55 min) in 1X running buffer.

To set up the wet transfer, Immobilon<sup>TM</sup>-FL PVDF membrane was activated in 100% CH<sub>3</sub>OH for 15 s and washed in 1X transfer buffer (15 min, Bio-Rad or prepared), and the SDS-PAGE gel was equilibrated in transfer buffer (15 min). The gel was then firmly sandwiched into a wet transfer cassette with components pre-soaked in transfer buffer, in the following order from bottom to top: one sponge, two filter papers, activated Immobilon<sup>TM</sup>-FL PVDF membrane, gel, two filter papers, one sponge. A magnetic stirrer bar and freezer block were placed into the wet transfer tank filled with pre-chilled 1X transfer buffer, the tank was placed atop a magnetic plate, and the transfer was run (90 V, 1 h 30 min, 4 °C, or 90 V, 2 h, 4 °C) with the transfer buffer being gently stirred.

To confirm whether the transfer of proteins from the gel to the PVDF membrane was successful, the gel was covered in Coomassie stain for 30 min, then de-stained in 25% CH<sub>3</sub>OH (overnight, 4 °C), and the membrane was briefly incubated in Ponceau S solution until red protein bands were evident. The membrane was then imaged using the ChemiDoc<sup>TM</sup> XRS system (Bio-Rad), rinsed multiple times with Milli-Q<sup>®</sup> H<sub>2</sub>O until the Ponceau stain was mostly removed, and washed in 1X TBS (5 min).

Next, the membrane was blocked in blocking buffer for 1 h, at RT, with rocking. Primary antibody solution (refer to table 3.8 for combinations) was prepared in 1:1 OBB to TBS-T, with primary antibodies for target proteins of interest, and the membrane was incubated in the solution (overnight, 4 °C with gentle rocking).

**Day two:**

The Coomassie stained gel was imaged on the ChemiDoc<sup>TM</sup> XRS. The Western blot membrane was briefly rinsed with 1x TBS-T, then washed in TBS-T (5 min) and TBS (2 x 5 min). Secondary antibody solutions at 1:20,000 dilution in 1:1 OBB to TBS-T, were prepared with secondary antibodies against the corresponding host species of the primary antibody (refer to table 3.8 for combinations), and the membrane was incubated in the solution (1 h, darkness, RT, with rocking). The membrane was rinsed briefly with TBS-T, washed with TBS-T (5 min) and TBS (2 x 5 min), then rinsed with Milli-Q<sup>®</sup> H<sub>2</sub>O.

TABLE 3.8: Summary of combinations used for each Western blot

	Primary antibody	Conc.	Secondary IR dye	Conc.	Samples
1	Rb TDP-43 general protein tag (ProteinTech)	1:1,000	anti mouse 680 nm and anti rabbit 800 nm	1:20,000	All CRISPR- <i>CCNF</i> <sup>S621G</sup> mouse model cohort protein lysates
	Rb cyclin F (Santa Cruz)	1:500			
	Ms GAPDH (ProteinTech)	1:5,000			
	Rb ubiquitin (Dako)	1:500			
2	Rb TDP-43 general protein tag (ProteinTech)	1:1,000	anti mouse 680 nm and anti rabbit 800 nm	1:20,000	All CRISPR- <i>CCNF</i> <sup>S621G</sup> mouse model cohort protein lysates
	Rb cyclin F (Santa Cruz)	1:200			
	Ms GAPDH (ProteinTech)	1:5,000			
	Rb ubiquitin (Dako)	1:500			
3	Rb cyclin F (ThermoFisher)	1:500	anti mouse 800 nm (neglected to add anti rabbit 680 nm the first time)	1:20,000	CRISPR- <i>CCNF</i> <sup>S621G</sup> mouse #4(WT) protein lysate
	Ms GAPDH (ProteinTech)	1:6,000			
	Rb cyclin F (ThermoFisher)	1:750	anti mouse 800 nm		
	Ms GAPDH (ProteinTech)	1:6,000			
	Ms cyclin F (Santa Cruz)	1:100			
	Ms GAPDH (ProteinTech)	1:6,000			
	Ms cyclin F (Santa Cruz)	1:250			
	Ms GAPDH (ProteinTech)	1:6,000			
4	Ms cyclin F (Santa Cruz)	1:100	anti mouse 800 nm	1:20,000	Spleen protein lysate from CRISPR- <i>CCNF</i> <sup>S621G</sup> mouse #4(WT) and HEK293 cell protein lysate
	Ms GAPDH (ProteinTech)	1:6,000			
	Ms cyclin F (Santa Cruz)	1:500	anti mouse 800 nm and anti rabbit 680 nm		
	Ms GAPDH (ProteinTech)	1:6,000			
	Rb cyclin F (Santa Cruz)	1:500			
	Ms GAPDH (ProteinTech)	1:6,000			
5	Ms cyclin F (Santa Cruz)	1:100	anti mouse 800 nm	1:20,000	Neuro-2a cell protein lysate
	Ms GAPDH (ProteinTech)	1:6,000			
	Ms cyclin F (Santa Cruz)	1:500	anti mouse 680 nm and anti rabbit 800 nm		
	Ms GAPDH (ProteinTech)	1:6,000			
	Rb cyclin F (Santa Cruz)	1:500			
	Ms GAPDH (ProteinTech)	1:6,000			

Note: rb is an abbreviation for rabbit and ms is an abbreviation for mouse. Primary antibody concentrations were chosen based on product data sheets and prior lab use of the antibody.

### 3.4.4.1 Western blot imaging and analysis

After day two of the Western blot protocol, all membranes were imaged on the Odyssey CLx (LiCor) with Image Studio software, auto setting. Some membranes were only imaged wet and others were imaged both wet and dry in attempt to obtain brighter protein signals. To measure expression of the proteins of interest, Image Studio was used to draw a rectangle around each protein band and the signal intensity output was provided by the software. The signal intensity was then normalised to the constitutively expressed housekeeping protein, GAPDH, and one-way ANOVA with multiple comparisons ( $P < 0.05$ ) performed on the data using Graph Pad Prism (version 7).

### 3.4.5 Reverse transcription-quantitative polymerase chain reaction (RT-qPCR)

#### 3.4.5.1 RNA extraction

RNA was extracted from #15(WT) mouse spleen, thoracic and sacral spinal cord tissues from #15(WT) and CRISPR-*CCNF*<sup>S621G</sup> mice #16(heterozygous), and #17(homozygous), and spleen from #4(WT), #7(WT), and CRISPR-*CCNF*<sup>S621G</sup> mice #9(heterozygous), #14(heterozygous), #16(heterozygous), #3(homozygous), #8(homozygous), #17(homozygous), following an adapted RNeasy<sup>®</sup> mini kit part one and two protocol. Tissues were transferred into a lysing matrix tube (MP biomedical) with 1 mL QIAzol lysis reagent and homogenised using the FastPrep-24<sup>TM</sup> tissue homogeniser (MP biomedical), run for 20 s (spinal cord tissues) or 40 s (spleen tissue). Samples were left to sit at RT for 5 min, then 200  $\mu$ L chloroform was added to each. Samples were shaken vigorously (15 s), left to sit at RT (3 min) and centrifuged at 13,000 rpm for 15 min at 4 °C, to separate tissue RNA, lipids and DNA into three phases. Around 500  $\mu$ L of clear upper aqueous RNA phase was transferred to new 1.5 mL tubes, 500  $\mu$ L 70% ethanol was added to each, followed by thorough mixing via vortex. Half of each sample was transferred to an RNeasy spin column, centrifuged (15 s, 10,000 rpm) and the flow through discarded. This step was repeated for the remaining half of each sample.

For DNase digestion in RNeasy spin columns, 350  $\mu$ L buffer RW1 was added to each RNeasy spin column, which was then centrifuged (15 s, 10,000 rpm), flow through was discarded, 80  $\mu$ L DNase I incubation mix (10  $\mu$ L DNase I stock solution and 70  $\mu$ L buffer RDD) was added directly to the columns, which were then incubated (15 min, RT). A further 350  $\mu$ L buffer RW1 was added to each RNeasy spin column, the columns were centrifuged (15 s, 10,000 rpm), and flow through discarded.

For RNA cleanup, steps 4-6 from RNeasy<sup>®</sup> mini kit part 2 were followed. 500  $\mu$ L buffer RPE was added to each RNeasy spin column, centrifuged (15 s, 10,000 rpm), and flow through discarded. This was then repeated with 2 min centrifugation. RNeasy spin columns were placed into new 2 mL collection tubes, centrifuged (1 min, full speed) and flow through and tube discarded. To elute RNA, each RNeasy spin column was placed in a new 1.5 mL collection tube, 30  $\mu$ L RNase free water was applied directly to the column membrane and the column was centrifuged (3 min, 10,000 rpm). The quantity and purity of the RNA samples was measured using the NanoDrop 2000 spectrophotometer (ThermoFisher), after which, they were frozen at -80 °C.

#### 3.4.5.2 cDNA synthesis

Each RNA sample was synthesised into cDNA following the SuperScript<sup>®</sup> III First-Strand Synthesis System for RT-PCR (Invitrogen) kit protocol (figure 3.4).

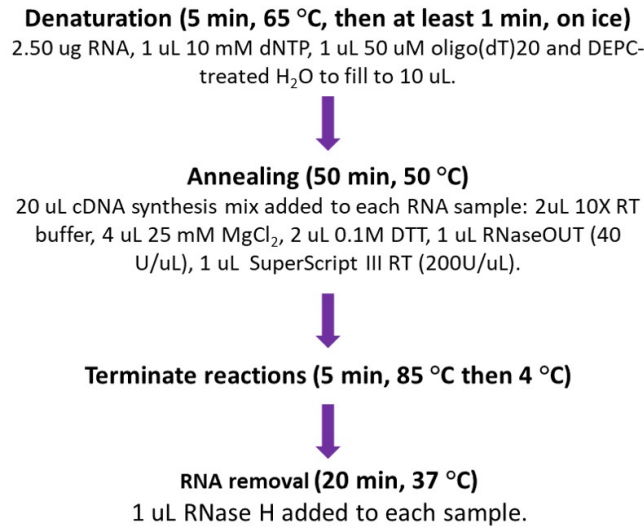


FIGURE 3.4: cDNA synthesis protocol.

All cDNA synthesis reactions were then stored at -30 °C until quantitative PCR (qPCR).

### 3.4.5.3 Quantitative polymerase chain reaction (qPCR)

To test the applicability of the *CCNF* VIC primer, #15(WT) spleen cDNA was run through qPCR. Reaction mix (left table 3.9) was added to eight wells of a 96-well optical reaction plate, followed by the addition of #15(WT) spleen cDNA template (1 pg to 100 ng in nuclease-free H<sub>2</sub>O) or nuclease-free H<sub>2</sub>O for a control (plate layout in right table 3.9).

TABLE 3.9: Test qPCR reaction mixture and plate layout with reaction combinations

Reagent	Volume ( $\mu$ l)		1
TaqMan Fast Advanced Master Mix (2X)	10.0	A	<i>ACTB</i> FAM + <i>CCNF</i> VIC + #15 spleen cDNA
Nuclease-free H <sub>2</sub> O	4.0	B	<i>ACTB</i> FAM + <i>CCNF</i> VIC + #15 spleen cDNA
<i>ACTB</i> FAM primer	1.0	C	<i>ACTB</i> FAM + #15 spleen cDNA
<b>and/or</b>		D	<i>ACTB</i> FAM + #15 spleen cDNA
<i>CCNF</i> VIC primer	1.0	E	<i>CCNF</i> VIC + #15 spleen cDNA
Total	15.0 or 16.0	F	<i>CCNF</i> VIC + #15 spleen cDNA
		G	<i>ACTB</i> FAM + <i>CCNF</i> VIC + H <sub>2</sub> O (control)
		H	<i>ACTB</i> FAM + <i>CCNF</i> VIC + H <sub>2</sub> O (control)

The reaction plate was sealed with optical adhesive film, centrifuged briefly and the qPCR reaction was run (table 3.10) on the ViiA™ 7 RT-PCR system (ThermoFisher). Data was exported to Microsoft Excel (version 1906, build 11727.20244) and  $\Delta$ Ct (Ct (cycle threshold) mean normalised to the endogenous (reference) gene *ACTB*),  $\Delta\Delta$ Ct

(normalised Ct value compared to normalised WT Ct value), and fold expression ( $2^{-\Delta\Delta Ct}$ , fold expression normalised to *ACTB* and relative to WT control, [Livak and Schmittgen \(2001\)](#)), and average fold expression, were calculated.

TABLE 3.10: qPCR conditions.

Temperature	Time	Cycles	Step
50 °C	2 min	1X	Hold
95 °C	2 min	1X	Hold
		40X	PCR:
95 °C	1 sec		Denature
60 °C	20 sec		Anneal/extend

After the spleen qPCR trial, triplicates of the three CRISPR-*CCNF*<sup>S621G</sup> mouse spinal cord samples (#15, #16, #17) were run as per the reaction mixture in table 3.9 and conditions in table 3.10, as a preliminary experiment to explore if a difference between the cohorts could be detected. Finally, qPCR was performed on triplicates of all nine mouse spleen cDNA samples with *ACTB* FAM and *CCNF* VIC primers, and  $\Delta Ct$ ,  $\Delta\Delta Ct$ ,  $2^{-\Delta\Delta Ct}$ , and average  $2^{-\Delta\Delta Ct}$  were calculated like prior. A one-way ANOVA with multiple comparisons ( $P < 0.05$ ) was performed on the  $2^{-\Delta\Delta Ct}$  values from each qPCR experiment.



“Let the cyclin F saga begin...”

- Winonah

# 4

## Results

The following chapter details the outcomes of each experimental strategy performed including [genotyping](#), [immunofluorescence staining](#), [Nissl staining](#), [mass spectrometry and \*in silico\* analysis](#), [Western blotting](#), and [RT-qPCR](#).

### 4.1 CRISPR-*CCNF*<sup>S621G</sup> mouse model genotyping

To begin the project, the mouse cohorts were genotyped to validate the presence of the *Ccnf* S621G mutation in each CRISPR-*CCNF* cohort, as well as the natural gene in the WT mouse cohort. The shared identity between the human and mouse cyclin F sequences was examined by alignment of the human (*homo sapiens*, NP\_001752.2) and mouse (*mus musculus*, NP\_031660.3) cyclin F protein sequences to confirm homology at the location of the cyclin F mutation at peptide 621 (figure 4.1). Alignment of the two species' cDNA sequences reinforced this homology at codon 1861, meaning that the genotyping primers designed (table 3.1) would accurately amplify both mouse and human cyclin F, in the WT and heterozygous and homozygous cohorts, respectively.



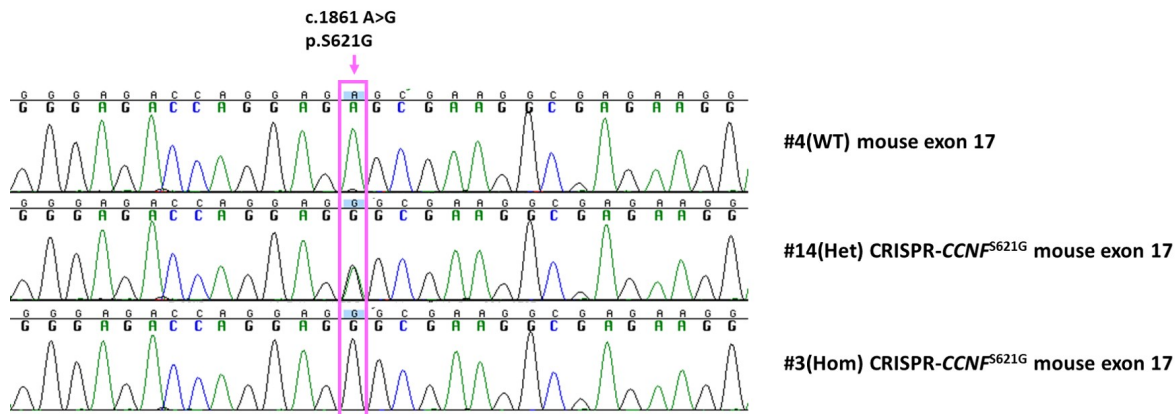


FIGURE 4.3: **Mouse genotypes were confirmed by sequencing.** WT, heterozygous and homozygous mouse DNA was amplified and Sanger sequenced using *CCNF* primers on exon 16. Peak colours indicate the identity of the nucleotide base(s) present and the pink box indicates nucleotide 1861, the location of the *Ccnf* mutation (c.1861 A<G). The chromatograms showed the correct matching genotype of each cohort: a tall, single peak at nucleotide 1861 represents homozygous variants (#4(WT) and CRISPR-*CCNF*<sup>S621G</sup> #3(Hom)), while double peaks with reduced height indicate heterozygous variants (CRISPR-*CCNF*<sup>S621G</sup> #14(Het)).

## 4.2 CRISPR-*CCNF*<sup>S621G</sup> mouse model histopathology

### 4.2.1 Immunofluorescence staining

#### 4.2.1.1 Antibody optimisations

First, antibody optimisation was performed to select the best cyclin F antibody and staining conditions. This was a crucial step because previous IF staining using cyclin F antibodies conducted by the Blair research group at Macquarie University had failed to provide specific staining in human tissues. This section contains a representative figure for each antibody that was optimised for IF staining, followed by a table summarising the observations and conclusions made for that antibody at each tested concentration. The antibodies trialled included: polyclonal rabbit cyclin F (Santa Cruz) (figure 4.4, table 4.1), monoclonal mouse NeuN (Merck Millipore) (figure 4.5, table 4.2), monoclonal mouse TDP-43 (Abnova) and polyclonal rabbit TDP-43 (ProteinTech) (figure 4.6, table 4.3), monoclonal mouse cyclin F (Santa Cruz) (figure 4.7, table 4.4), monoclonal mouse cyclin F blocking peptide (figure 4.8, table 4.5), and polyclonal rabbit cyclin F (LifeSpan BioSciences) (figure 4.9, table 4.6).

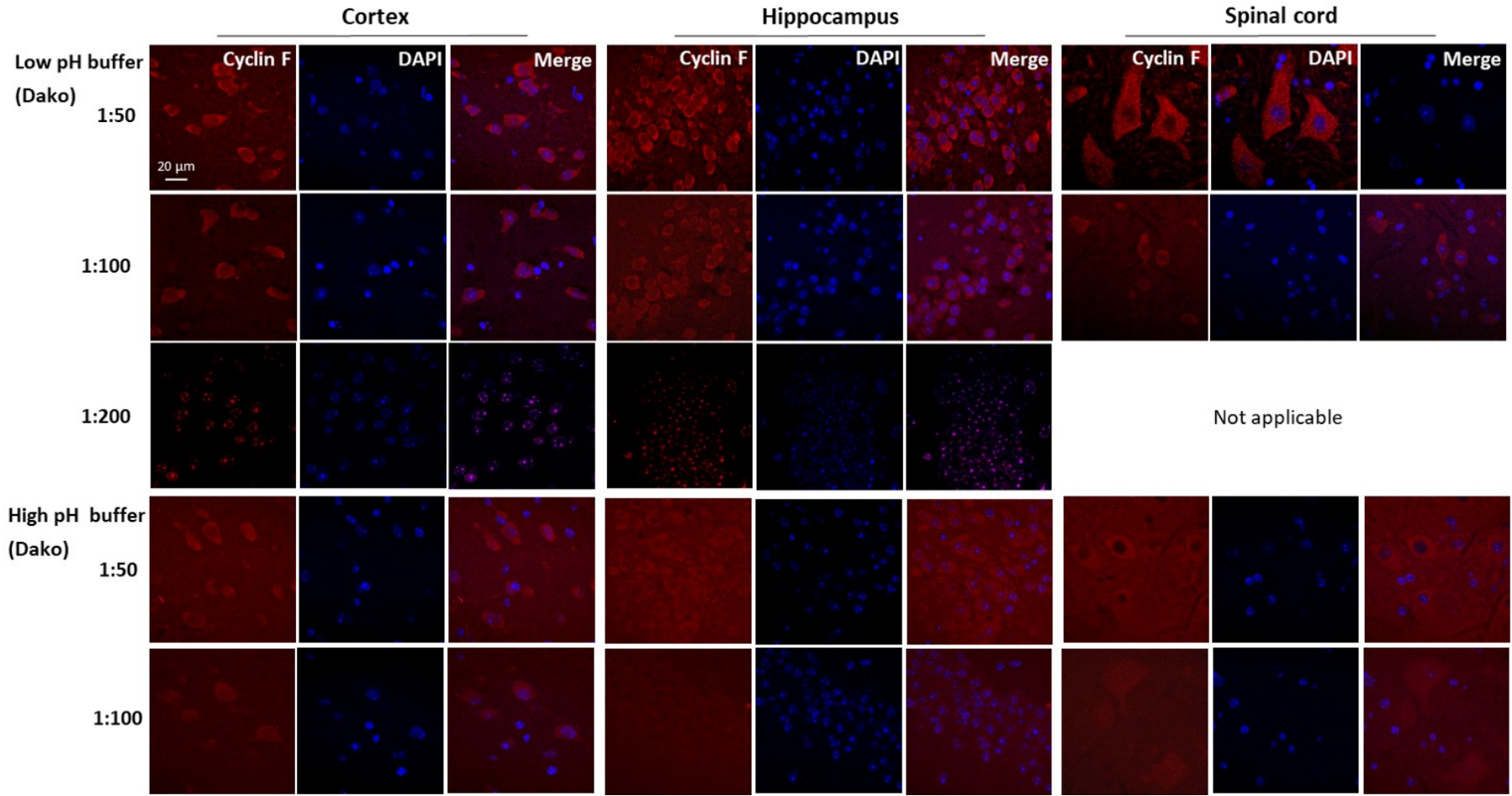


FIGURE 4.4: **Rabbit cyclin F (Santa Cruz) antibody optimisation.** Immunofluorescence staining images taken on LSM880 confocal microscope (Zeiss) with 63x oil objective lens. 1:50 and 1:100 rabbit cyclin F concentrations with low pH (Dako) antigen retrieval buffer gave the best images. N.B. “not applicable” means the particular tissue was either not stained in the given condition, or the location could not be imaged due to the section and slice of tissue used. Scale bar, 20  $\mu\text{m}$ .

TABLE 4.1: **IF antibody optimisation outcomes – Rb cyclin F (Santa Cruz)**

Conc.	Antigen retrieval buffer	Observation	Conclusion
1:50	Low pH (Dako)	Clear and bright cytoplasmic staining in spinal cord, hippocampal, and somatosensory cortex neurons, minimal overlap with DAPI in the nucleus, and less background staining compared to high pH antigen retrieval buffer equivalent.	Keep using low (Dako) pH antigen retrieval buffer and can increase dilution ratio to reduce background staining.
1:100		Brightness of cytoplasmic staining slightly reduced compared to 1:50 but still gave clear image, and better than when high (Dako) pH antigen retrieval buffer used.	Use 1:100 or 1:50 dilution and low (Dako) pH antigen retrieval buffer.
1:200		Signal intensity from staining too weak. Staining appeared mainly nuclear.	Need to use a higher concentration.
1:50	High pH (Dako)	High background staining reduced clarity of images. Could barely see cytoplasmic staining in neurons of the spinal cord, hippocampal, and somatosensory cortex.	High pH antigen retrieval buffer unsuitable for this antibody.
1:100		Staining very weak in hippocampal and spinal cord neurons, difficult to discern cells from background signal. Cortical cell staining only just visible.	This combination of antigen retrieval buffer and antibody concentration are unsuitable.



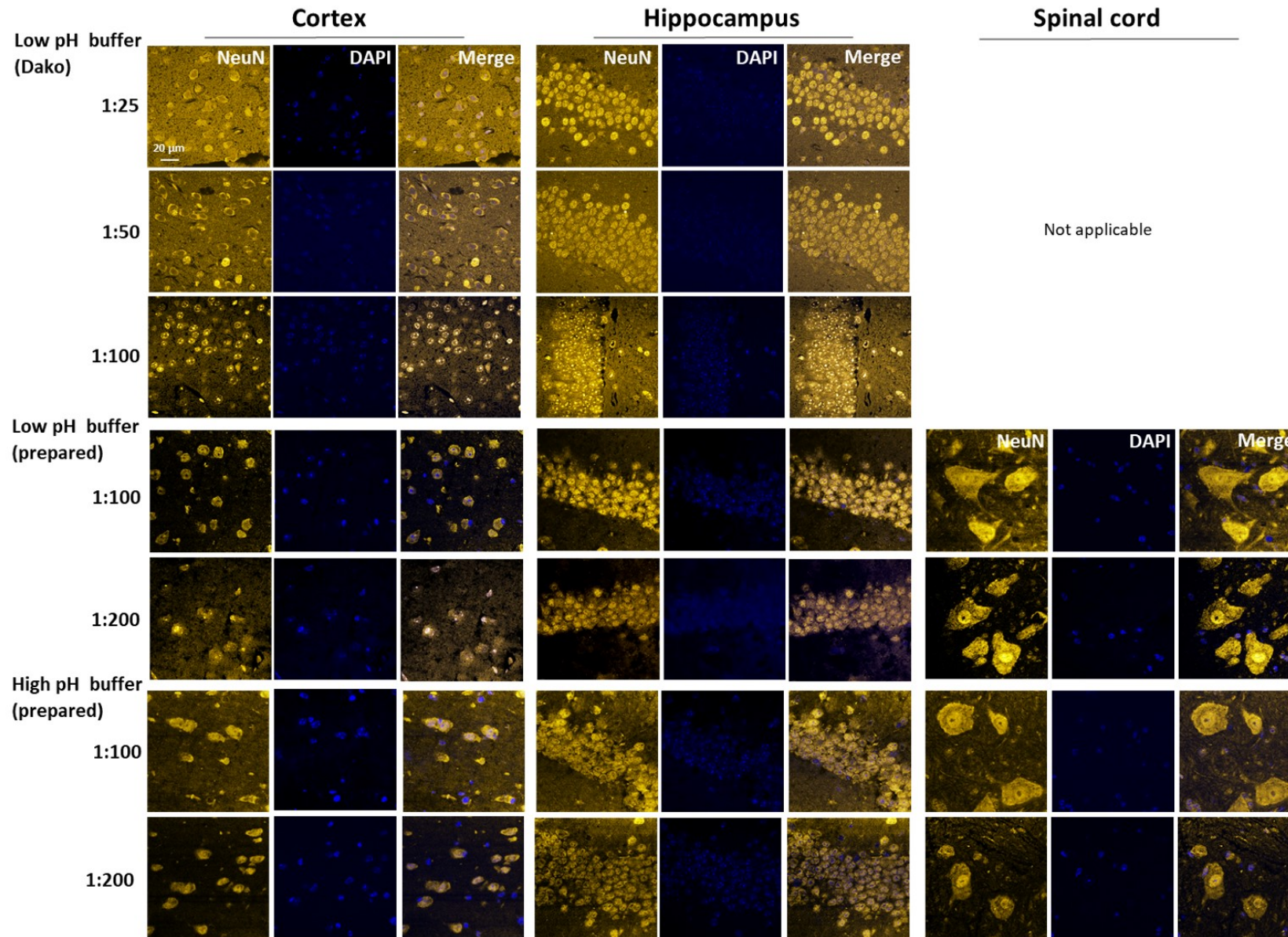


FIGURE 4.5: **Mouse NeuN (Merck Millipore) antibody optimisation.** Immunofluorescence staining imaged on LSM880 confocal microscope (Zeiss) with 63x oil objective lens. The low pH (prepared) buffer gave a crisper image compared to the high pH (prepared) buffer, and the 1:200 concentration gave the best balance of neuron brightness and reduced background signal. N.B. “not applicable” means the particular tissue was not stained in the given condition. Scale bar, 20  $\mu\text{m}$ .

TABLE 4.2: IF antibody optimisation outcomes – Ms NeuN (Merck Millipore)

Conc.	Antigen retrieval buffer	Observation	Conclusion
1:25	Low pH (Dako)	Staining of the cells and background tissue was too strong. The yellow fluorescence was localised to both the nucleus and cytoplasm in brain neurons.	Use reduced concentration of the antibody, the low pH antigen retrieval buffer does not appear to be an issue.
1:50		Very similar to 1:25 – too much background staining.	Use reduced concentration in future.
1:100		Background staining reduced but still too high.	Need to reduce the concentration further.
1:100	Low pH (prepared)	Good level of clear cytoplasmic and nuclear staining in the brain and spinal cord neurons. Background staining still not optimal in spinal cord and very similar to the high pH (prepared) antigen retrieval buffer equivalent.	Use reduced concentration of the antibody with low pH antigen retrieval buffer.
1:200		Minimal-to-no background staining in the brain and spinal cord. NeuN bright and localised mainly to nucleus in hippocampal neurons and both cytoplasm and nucleus in cortical and spinal cord neurons.	Continue using this concentration with low (prepared) pH antigen retrieval buffer as the clarity of staining in spinal cord and cortical neurons was better than when high pH buffer was used.
1:100	High pH (prepared)	Good level of cytoplasmic staining in cortical, hippocampal and spinal cord neurons, however background staining was increased compared to when low pH (prepared) antigen retrieval buffer was used. A full circle of nuclear staining in spinal cord neurons evident.	Good but use reduced concentration of the antibody to save money and reduce background staining. Can use low (prepared) or high (prepared) pH antigen retrieval buffer at this concentration as there was little difference between the two.
1:200		Brightness of staining similar to when low pH antigen retrieval buffer used. Circular nuclear staining more evident at this concentration when compared to 1:100.	Good antibody concentration to use again, ideally with low (prepared) pH antigen retrieval buffer.

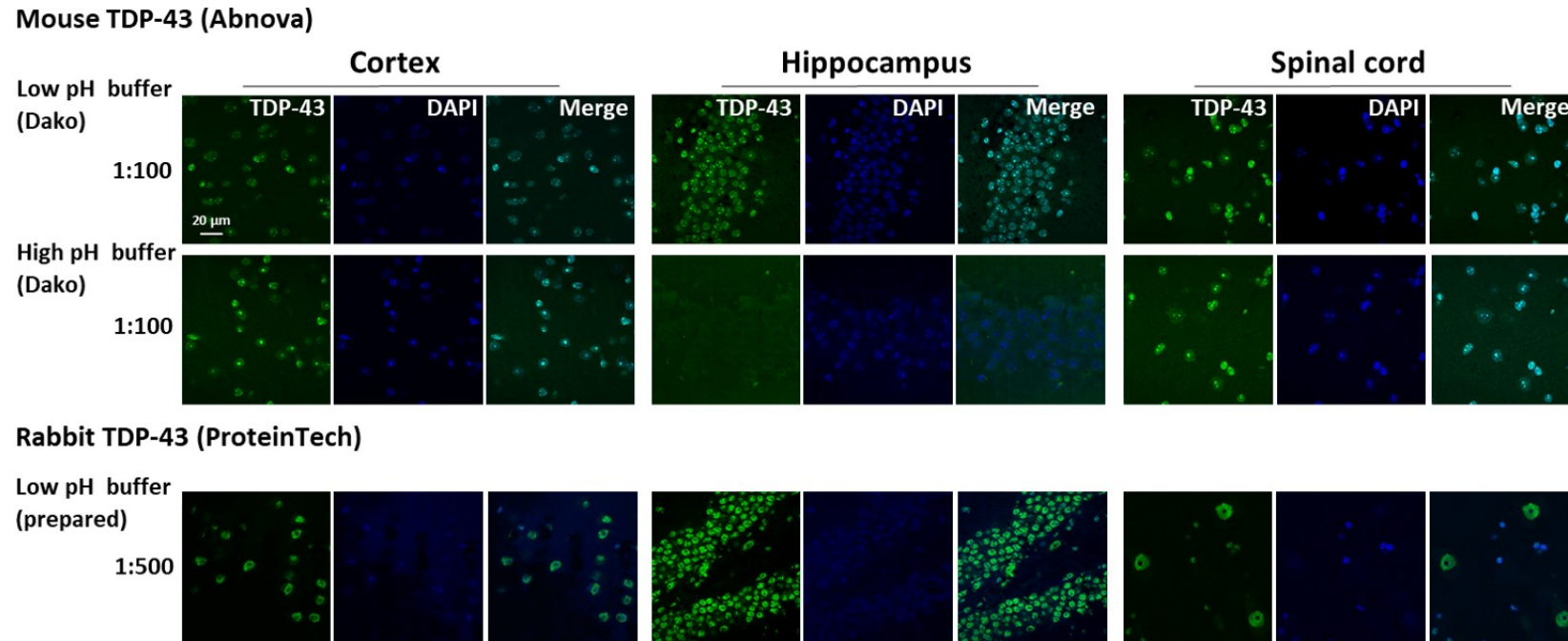


FIGURE 4.6: **Mouse TDP-43 (Abnova) and rabbit TDP-43 (ProteinTech) antibody optimisation.** Images taken on LSM880 confocal microscope (Zeiss) with 63x oil objective lens. Scale bar, 20  $\mu\text{m}$ .

TABLE 4.3: **IF antibody optimisation outcomes – Ms TDP-43 (Abnova) and Rb TDP-43 (ProteinTech)**

Antibody	Conc.	Antigen retrieval buffer	Observation	Conclusion
Ms TDP-43 (Abnova)	1:100	Low pH (Dako)	Staining consisted of bright nuclear specks, but TDP-43 and DAPI staining directly overlapped in the merge image indicating that the signals may be overlapping.	Put DAPI and the secondary antibody with closest excitation and emission wavelengths on separate tracks for future imaging to prevent signals overlapping.
	1:100	High pH (Dako)	Very poor staining in the hippocampus, average staining in the cortex and spinal cord with a slight background signal compared to the low pH (Dako) antigen retrieval buffer.	Use low pH (Dako) antigen retrieval buffer when using antibody again, and put DAPI and the secondary antibody with closest excitation and emission wavelengths on separate tracks when imaging, to prevent signals overlapping.
Rb TDP-43 (Protein-Tech)	1:500	Low pH (prepared)	Bright nuclear staining in cells in the cortex, hippocampus, and spinal cord. Distinct nuclear ring of staining seen in spinal cord. No background staining.	Use this antibody at 1:500 with low pH antigen retrieval buffer.

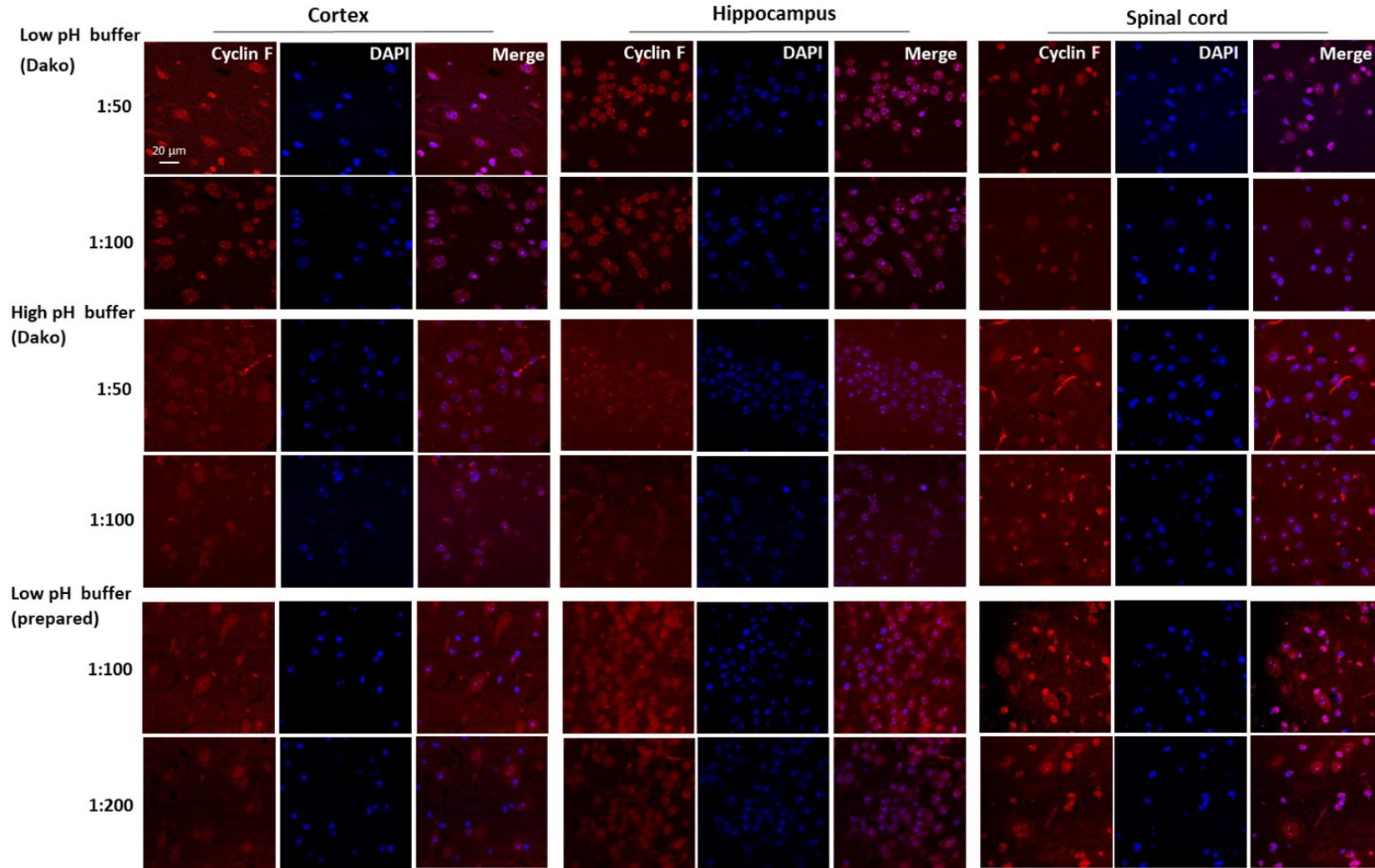


FIGURE 4.7: Mouse cyclin F (Santa Cruz) antibody optimisation. Images taken on LSM880 confocal microscope (Zeiss) with 63x oil objective lens. Scale bar, 20 μm.

TABLE 4.4: **IF antibody optimisation outcomes – Ms cyclin F (Santa Cruz)**

Conc.	Antigen retrieval buffer	Observation	Conclusion
1:50	Low pH (Dako)	Bright predominantly nuclear staining in hippocampal neurons but a mix of nuclear and cytoplasmic in cortical and spinal cord neurons. Overall brighter staining and reduced background signal compared to high (Dako) pH antigen retrieval buffer equivalent.	Keep using low (Dako or prepared) pH antigen retrieval buffer, could use decreased concentration to reduce background further and conserve antibody.
1:100		Brightness of staining reduced but stronger in cortex and hippocampus than in high (Dako) pH antigen retrieval buffer equivalents.	Continue using 1:100 concentration with low (Dako or prepared) pH antigen retrieval buffer.
1:50	High pH (Dako)	Staining not as bright or distinct compared to low pH equivalent.	Do not use high pH antigen retrieval buffer with this antibody.
1:100		Very low level of staining.	Concentration too low with the high (Dako) pH antigen retrieval buffer. Do not use high pH antigen retrieval buffer with this antibody.
1:100	Low pH (prepared)	Image clarity decreased compared to when the low (Dako) pH antigen retrieval buffer was used, but good signal intensity. Cyclin F staining a mix of nuclear and cytoplasmic.	Low pH antigen retrieval buffer ideal for this antibody. Dako better than prepared.
1:200		Slightly reduced level of brightness compared to 1:100.	Use 1:100 concentration.

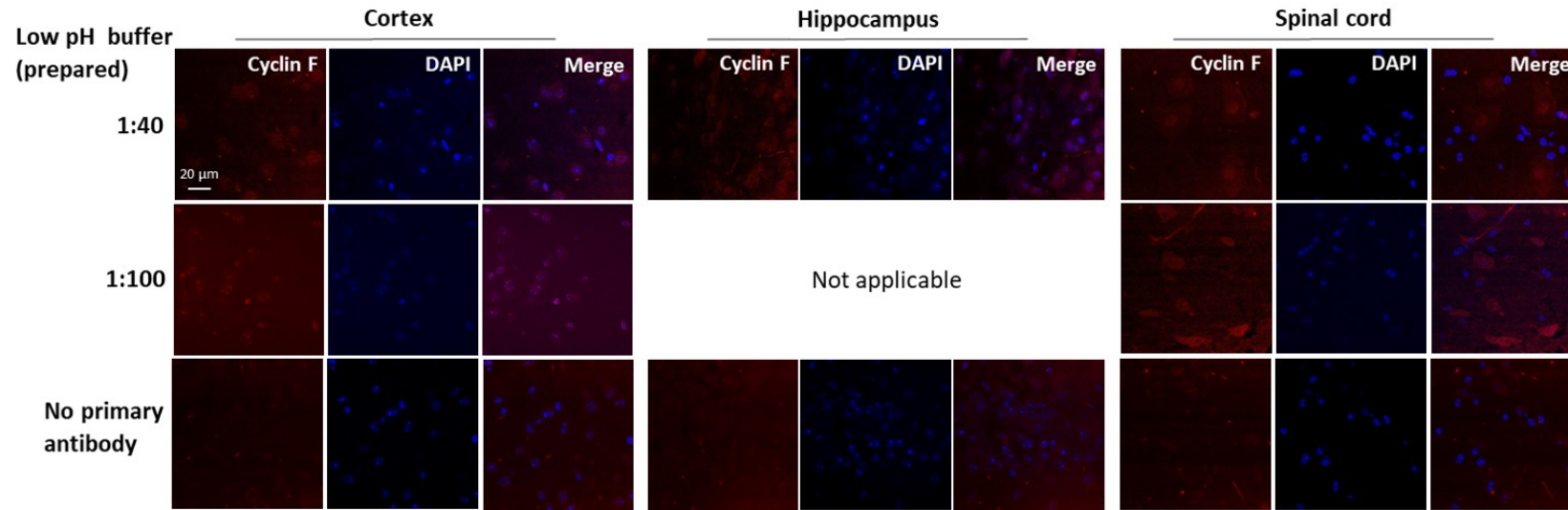


FIGURE 4.8: **Mouse cyclin F blocking peptide (Santa Cruz) antibody optimisation.** Images taken on LSM880 confocal microscope (Zeiss) with 63x oil objective lens. N.B. “not applicable” means the particular tissue location could not be imaged due to the section and slice of tissue used. Scale bar, 20  $\mu$ m.

TABLE 4.5: **IF antibody optimisation outcomes – Ms cyclin F blocking peptide (Santa Cruz)**

Conc.	Antigen retrieval buffer	Observation	Conclusion
1:40	Low pH (prepared)	Cyclin F signal greatly reduced in all tissue sections. Still had a small amount of background auto-fluorescence.	The 1:40 concentration of blocking peptide successfully blocked Ms cyclin F antibody (Santa Cruz) binding to the mouse cyclin F protein.
1:100		Background cyclin F signal moderately reduced, substantial variation of blocking effect seen between tissue sections difficult to interpret whether or not blocking was successful.	Concentration of blocking peptide not high enough to completely prevent cyclin F staining but revealed that Ms cyclin F antibody (Santa Cruz), targeted to human protein, had some affinity for the mouse cyclin F protein.

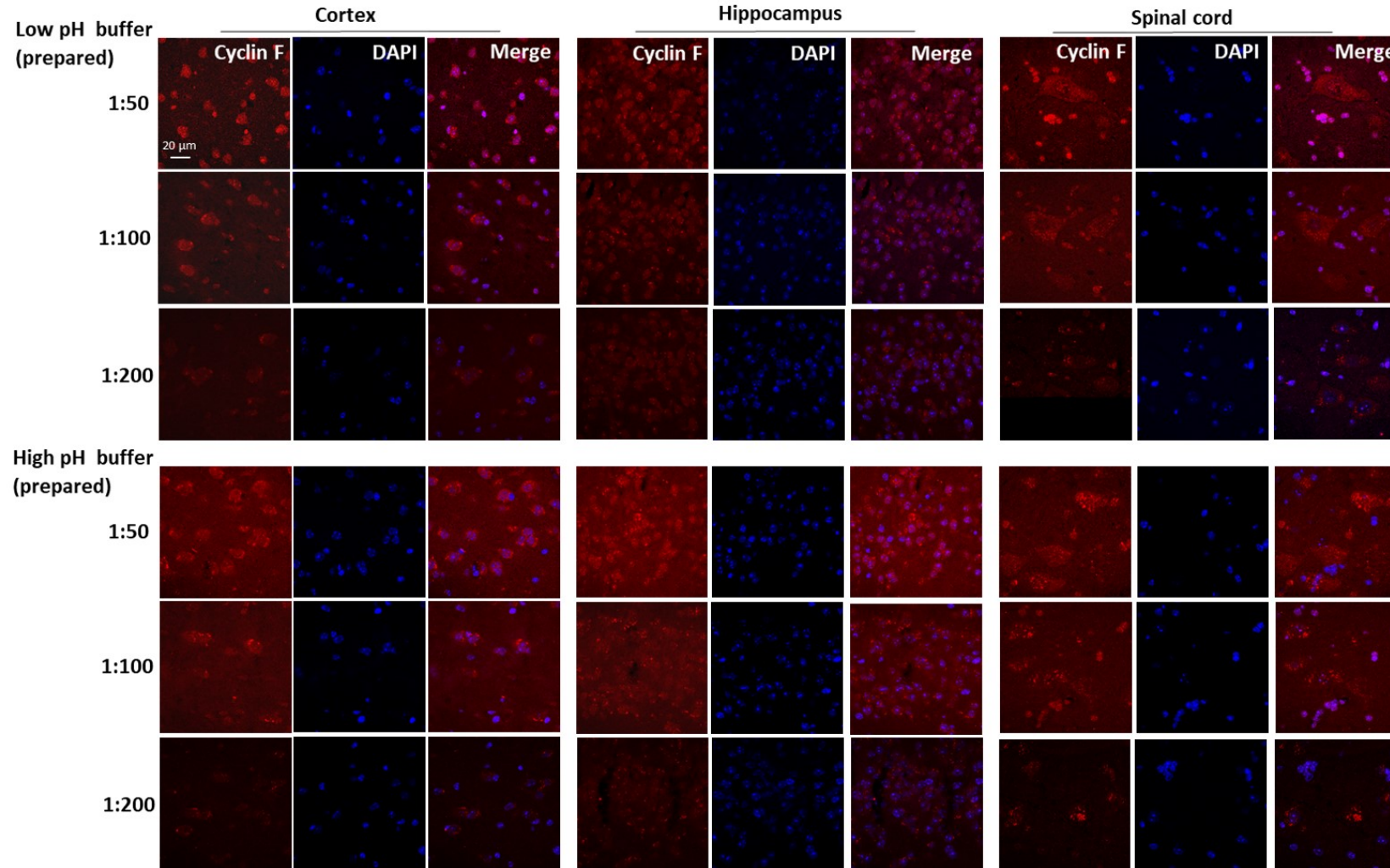


FIGURE 4.9: **Rabbit cyclin F (LifeSpan BioSciences) antibody optimisation.** Immunofluorescence staining images taken on LSM880 confocal microscope (Zeiss) with 63x oil objective lens. The low pH (prepared) antigen retrieval buffer combined with 1:50 concentration of the rabbit cyclin F antibody produced the clearest image out of all the variations tested. Scale bar, 20  $\mu\text{m}$ .

TABLE 4.6: IF antibody optimisation outcomes – Rb cyclin F (LifeSpan BioSciences)

Antibody	Conc.	Antigen retrieval buffer	Observation	Conclusion
Rb cyclin F (LifeSpan Biosciences)	1:50	Low pH (prepared)	Strong predominantly cytoplasmic staining in spinal cord, nuclear and cytoplasmic staining in hippocampal and cortical neurons as an overlap with DAPI was seen in some cells. Cell boundaries not completely clear-cut due to background staining.	In an effort to preserve antibody and reduce background staining, use lower concentration in future staining.
	1:100		Good level of staining, slightly reduced compared to 1:100. Some tissue sections stained well, others did not – there was quite a lot of variation. Again, spinal cord staining was cytoplasmic, and hippocampal and cortical staining was a mix of nuclear and cytoplasmic.	Use this concentration and the low pH (prepared) antigen retrieval buffer if using antibody in the future.
	1:200		Staining level was too low and made it difficult to identify cells clearly. However, there was no background staining.	Use higher concentration (i.e. 1:100) if using the antibody again in the future.
	1:50	High pH (prepared)	Overall level of staining appeared to be the similar to when the low (prepared) pH antigen retrieval buffer was used, but there was increased background signal. Staining was somewhat punctate.	Use decreased concentration to reduce background signal and preserve antibody, and use low pH (prepared) antigen retrieval buffer if using the antibody again.
	1:100		Variation in staining levels observed, more commonly weak than strong, and background signal still visible.	Consider using this concentration or a slightly increased concentration with low pH antigen retrieval buffer if using the antibody in the future.
	1:200		Difficult to see cyclin F in most images but no background staining present.	This concentration was not ideal so do not use it again in the future.

To summarise the antibody optimisation results, rabbit cyclin F (Santa Cruz) antibody gave good cytoplasmic staining when low pH antigen retrieval buffer was used, but the antibody was discontinued by Santa Cruz and the mouse cyclin F (Santa Cruz) antibody gave better overall staining in each tissue type. The mouse cyclin F (Santa Cruz) antibody produced a mix of cytoplasmic and nuclear staining with more prominent cytoplasmic staining in spinal cord tissue compared to the brain tissue, and was brightest when low pH antigen retrieval buffer was used. When a blocking peptide against it was used at 1:40 concentration, cyclin F staining decreased greatly illustrating the specificity of the antibody. Consequently, the mouse cyclin F (Santa Cruz) antibody at 1:100 concentration was selected to be used on all samples as it provided better and more consistent staining overall compared to rabbit (Santa Cruz) and mouse (LifeSpan BioSciences) antibodies, although less optimal when compared to the bright and crisp staining obtained with the optimised TDP-43 (1:500, ProteinTech) and NeuN (1:200, Merck Millipore) antibodies. While the low pH (Dako) antigen retrieval buffer gave the clearest imaging results, cost

constraints precluded its use in the main study. Instead, the low pH (prepared) antigen retrieval buffer was selected for IF investigation of ALS/FTD pathology as it provided the least overall background fluorescence.

#### 4.2.1.2 Investigation of ALS/FTD pathology

To investigate the presence of ALS/FTD pathology in the CRISPR-*CCNF*<sup>S621G</sup> model mice, three regions of interest – the motor cortex, hippocampus, and spinal cord, were studied in comparison to that in WT mice. A total of 54 brain and 90 spinal cord sections across nine mice were examined. Specifically, 27 brain and 45 spinal cord tissue sections were assessed for TDP-43 aggregates and mis-localisation and co-localisation with cyclin F; 13 brain and 22 spinal cord tissue sections were assessed for ubiquitin inclusions; and 14 brain and 23 spinal cord sections were assessed for the presence and/or aggregates of phosphorylated TDP-43.

##### **Cyclin F and TDP-43 staining**

The mouse tissues were first examined for the location of cyclin F and aggregation and/or mis-localisation of TDP-43. In the cortex and hippocampal neurons (figures 4.10 and 4.11), cyclin F was present in the nucleus and cytoplasm, while in the spinal cord it was mostly cytoplasmic (figure 4.12). No cyclin F positive aggregates were evident in any tested tissue. No neurons in the motor cortex, hippocampus, or spinal cord, displayed the presence of TDP-43 aggregates or cytoplasmic mis-localisation of the protein in WT, heterozygous, or homozygous mice. As TDP-43 remained in the nucleus, it was also seen to co-localise with cyclin F in the brain, shown in purple-green in the merge images.

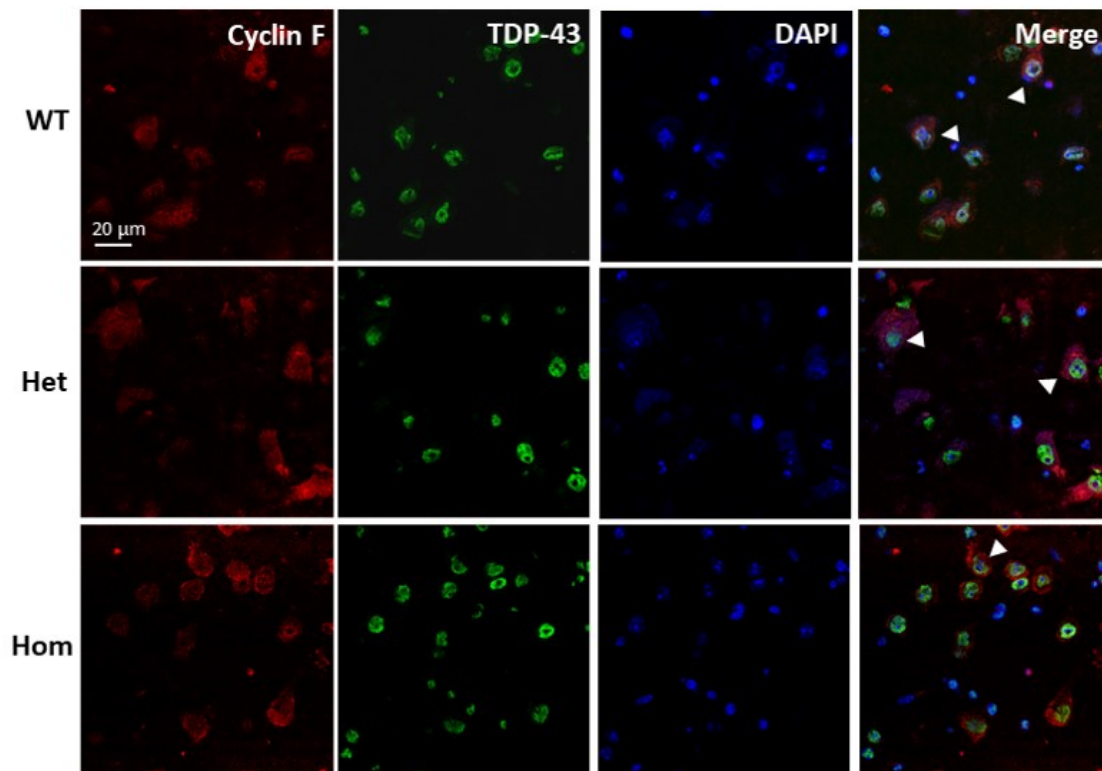


FIGURE 4.10: **TDP-43 does not aggregate in, or mis-localise to, the cytoplasm of motor cortex neurons in CRISPR-*CCNF*<sup>S621G</sup> mice.** Cortex stained with Ms cyclin F (1:100, Santa Cruz) and Rb TDP-43 (1:500, ProteinTech). The pattern of TDP-43 staining was ring-like around the inner edge of the nucleus and there were no aggregates. Cyclin F was located in both the nucleus and cytoplasm. White arrowheads point to TDP-43 and cyclin F co-localisation in the nucleus. Images taken on LSM880 confocal microscope (Zeiss) with 63x oil objective lens. Scale bar, 20 μm. n=3 biological replicates.

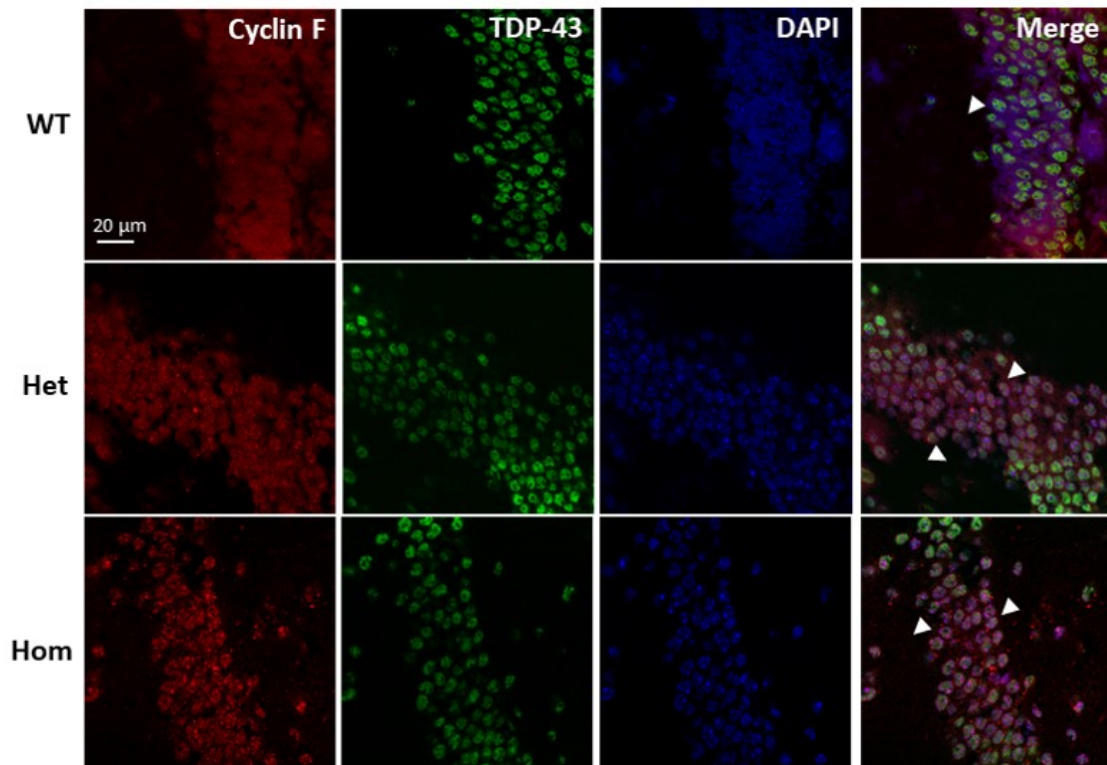


FIGURE 4.11: **TDP-43 remains nuclear in the hippocampus of CRISPR-*CCNF*<sup>S621G</sup> mice, where it co-localises with cyclin F.** Hippocampus stained with Ms cyclin F (Santa Cruz) and Rb TDP-43 (Protein Tech). The pattern of TDP-43 staining was diffuse throughout the nucleus, and cyclin F was located in both the nucleus and cytoplasm. White arrowheads point to TDP-43 and cyclin F co-localisation in the nucleus. Images taken on LSM880 confocal microscope (Zeiss) with 63x oil objective lens. Scale bar, 20 μm. n=3 biological replicates.

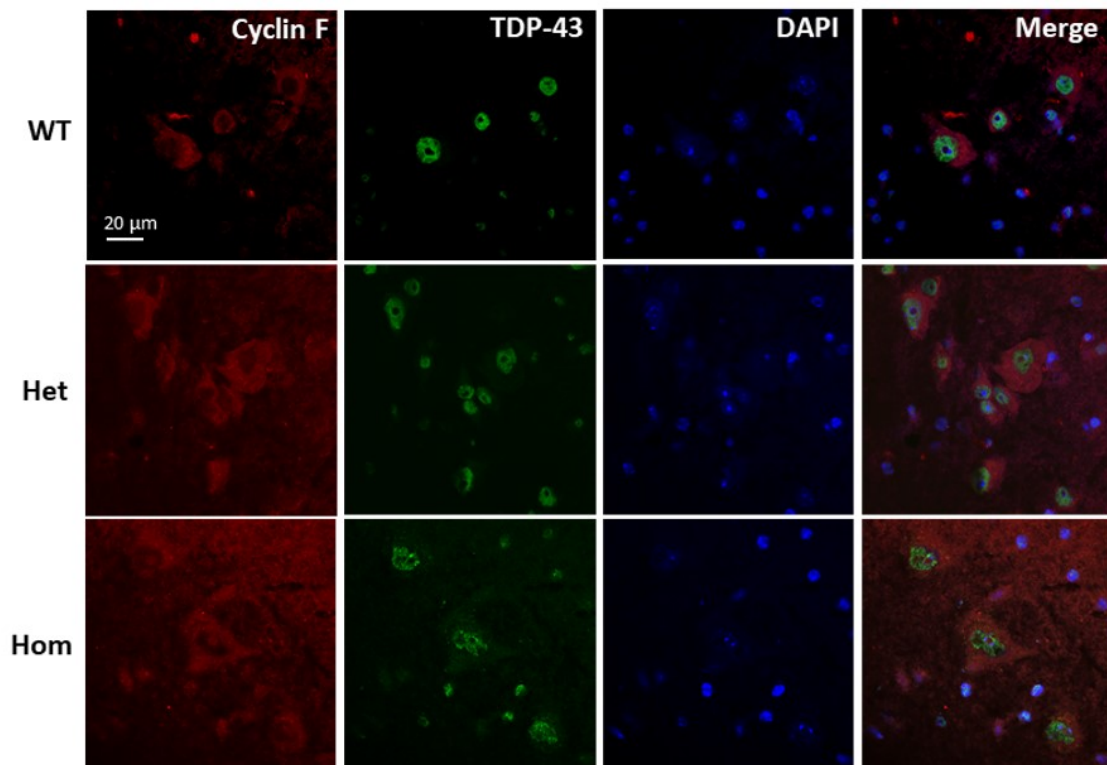


FIGURE 4.12: **No difference in TDP-43 or cyclin F staining in the spinal cord of WT and CRISPR-*CCNF*<sup>S621G</sup> mice.** Spinal cord stained with Ms cyclin F (Santa Cruz) and Rb TDP-43 (Protein Tech). Cyclin F was predominantly cytoplasmic and remained that way in all genotype samples. TDP-43 remained nuclear in a ring-like pattern around the inner edge of the nucleus. Images taken on LSM880 confocal microscope (Zeiss) with 63x oil objective lens. Scale bar, 20  $\mu\text{m}$ . n=3 biological replicates.

#### **Phosphorylated TDP-43 staining**

In addition to the TDP-43 tissue pathology described above, the presence of hyperphosphorylated TDP-43 deposits was also investigated in all mice. In all three tissue regions of interest, phosphorylated TDP-43 was not present (figures 4.13, 4.14, and 4.15). This was expected, based on the observation that there were no changes in normal TDP-43 localisation. Cyclin F was predominantly present in the nucleus but was also diffuse in the cytoplasm of cortical, hippocampal and spinal cord neurons.

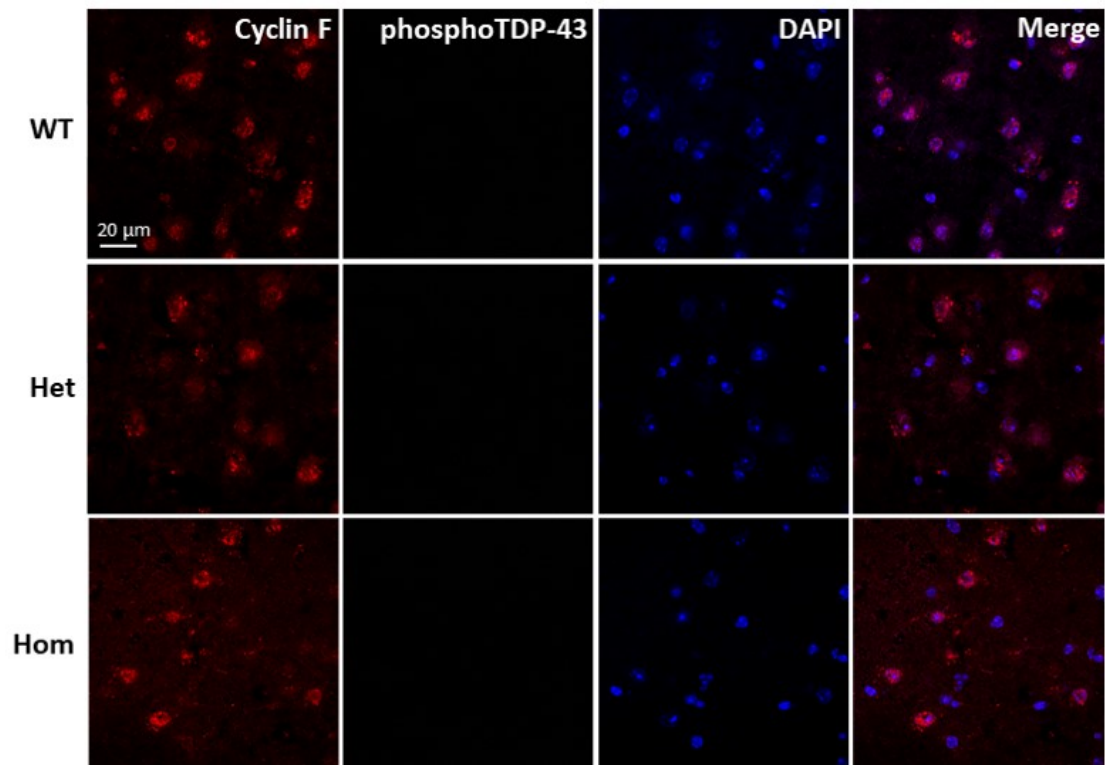


FIGURE 4.13: **Phosphorylated TDP-43 was not detected in cortical tissue from CRISPR-*CCNF*<sup>S621G</sup> mice.** Cortex stained with Ms cyclin F (1:100, Santa Cruz) and Rb phosphoTDP-43 (1:500, CosmoBio). Cyclin F was mainly present in the nucleus, evidenced by the magenta colour in the merge image. PhosphoTDP-43 was not detected. Images taken on LSM880 confocal microscope (Zeiss) with 63x oil objective lens. Scale bar, 20  $\mu\text{m}$ . n=3 biological replicates.

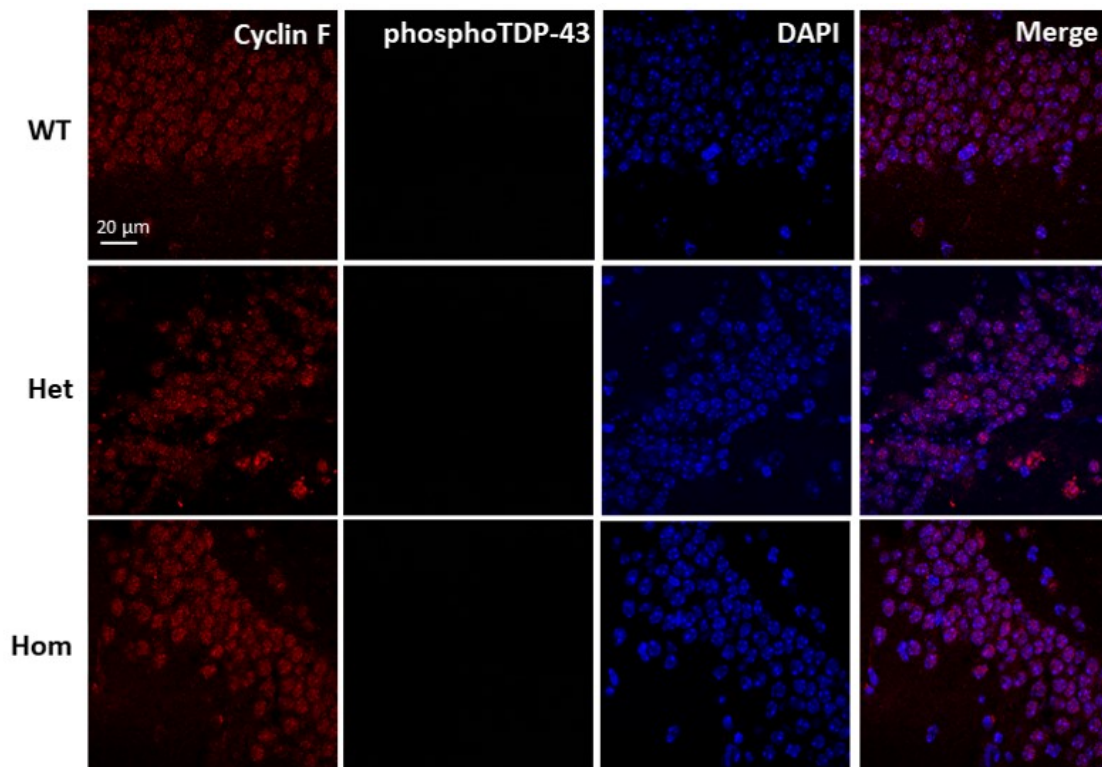


FIGURE 4.14: **Phosphorylated TDP-43 was not identified in hippocampal neurons from CRISPR-*CCNF*<sup>S621G</sup> mice.** Hippocampal tissue stained with Ms cyclin F (1:100, Santa Cruz) and Rb phosphoTDP-43 (1:500, CosmoBio). Cyclin F was mainly present in the nucleus, evidenced by the magenta colour in the merge image. PhosphoTDP-43 was not detected. Images taken on LSM880 confocal microscope (Zeiss) with 63x oil objective lens. Scale bar, 20  $\mu\text{m}$ . n=3 biological replicates.

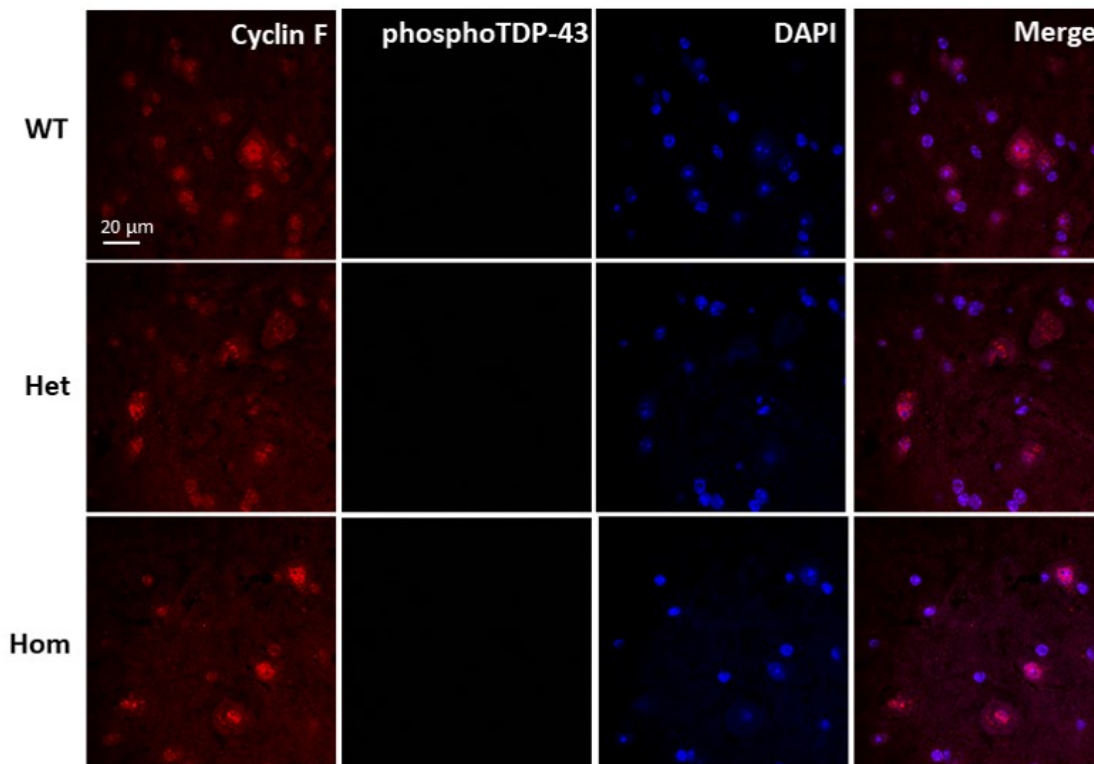


FIGURE 4.15: **Phosphorylated TDP-43 was not detected in spinal cord tissue from CRISPR-*CCNF*<sup>S621G</sup> mice.** spinal cord tissue stained with Ms cyclin F (1:100, Santa Cruz) and Rb phosphoTDP-43 (1:500, CosmoBio). Cyclin F was present in the nucleus (magenta colour in the merge image, the result of overlap with DAPI), and also diffuse in the cytoplasm. PhosphoTDP-43 was not detected. Images taken on LSM880 confocal microscope (Zeiss) with 63x oil objective lens. Scale bar, 20  $\mu$ m. n=3 biological replicates.

### Ubiquitin staining

The mouse NeuN (Merck Millipore) antibody was used to delineate neurons more clearly by IF staining. This antibody detects the neuron-specific, DNA-binding protein, NeuN, which is present in both the nuclei (principally) and cytoplasm of neurons in the central and peripheral nervous systems ([Gusel'nikova and Korzhevskiy, 2015](#)). The levels of ubiquitin-tagged proteins are abnormally elevated in neurodegenerative disease, especially ALS/FTD ([Neumann et al., 2006](#); [Williams et al., 2016](#)). These proteins may then build up to form inclusions that can be skein-like (fibrillous), round, or Lewy body-like (round and dense), and are largely located within motor neuron perikarya ([He and Hays, 2004](#)). The rabbit ubiquitin (Dako) antibody, which detects polyubiquitin-C protein, was used to reveal any ubiquitin build up and ubiquitin positive inclusions. The application of NeuN made it easier to locate neurons, particularly the large motor neurons, in the motor cortex and spinal cord, as the NeuN staining was bright and unambiguous. In motor neurons of the motorcortex (figure 4.16), ubiquitin staining was mostly diffuse with a small amount of cytoplasmic puncta seen in heterozygous and homozygous mice. These puncta were unlike that reported as pathological ([He and Hays, 2004](#)). In hippocampal

neurons this cytoplasmic puncta was non-existent and instead, the ubiquitin staining was diffuse in the nucleus, illustrated by the overlap of the purple (ubiquitin) and blue (DAPI) in the merged images (figure 4.17). In the spinal cord, ubiquitin staining in motor neurons was also diffuse with no skein-like or Lewy body-like inclusions (figure 4.18).

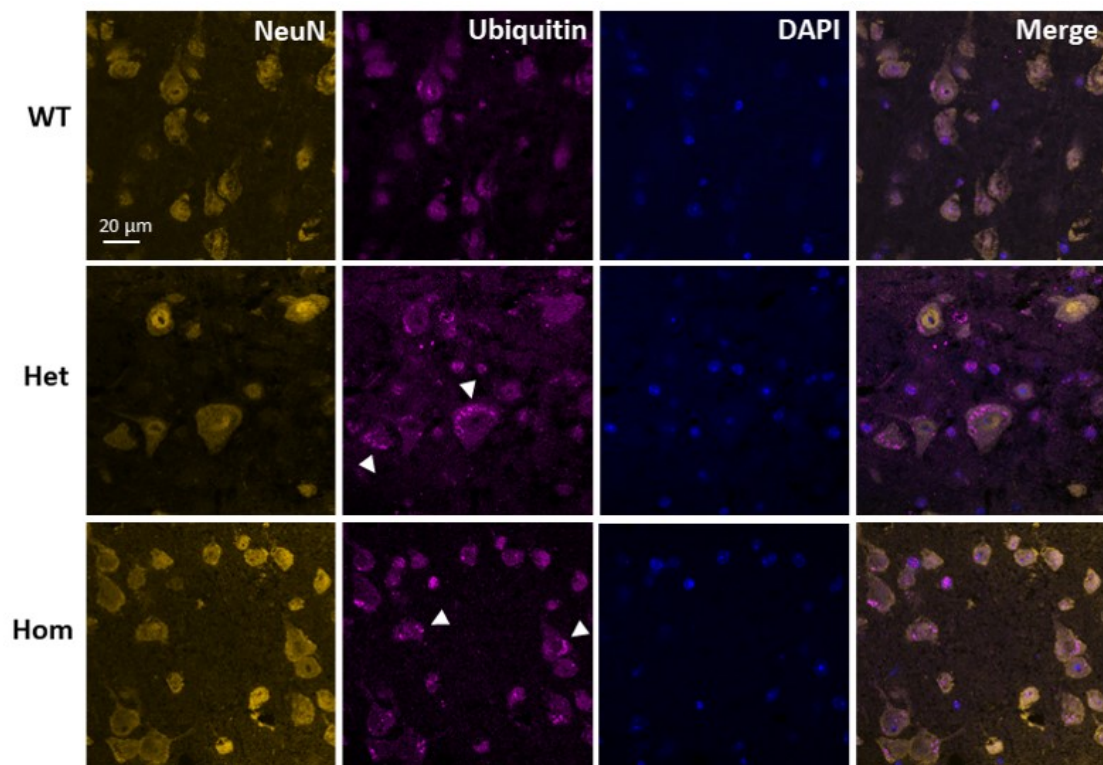


FIGURE 4.16: Diffuse ubiquitin and puncta in motor cortex neurons from heterozygous and homozygous CRISPR-*CCNF*<sup>S621G</sup> mice. WT, heterozygous, and homozygous CRISPR-*CCNF*<sup>S621G</sup> FFPE mouse motor cortex stained with Ms NeuN (1:200, Merck Millipore) and Rb ubiquitin (1:500, Dako). Ubiquitin staining was diffuse but there was also some cytoplasmic puncta indicated by the white arrowheads. Images taken on LSM880 confocal microscope (Zeiss) with x63 oil objective lens. Scale bar, 20  $\mu$ m. n=3 biological replicates.

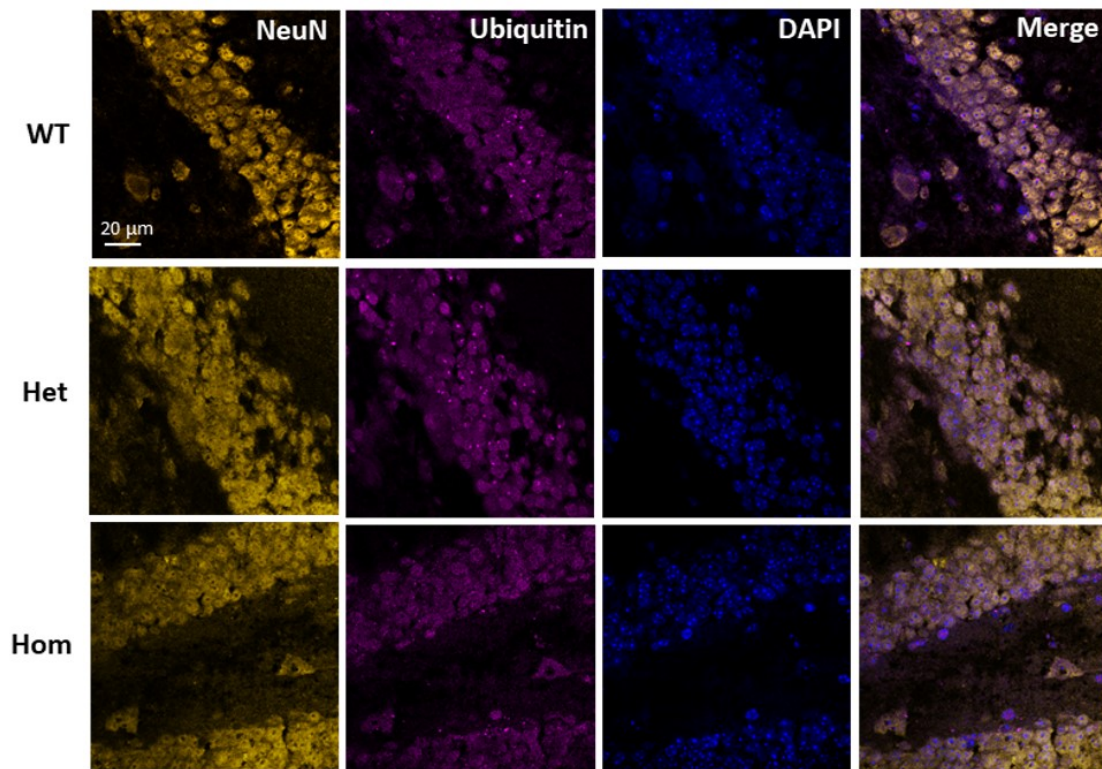


FIGURE 4.17: No ubiquitin-positive inclusions were detected in hippocampal neurons from CRISPR-*CCNF*<sup>S621G</sup> mice. WT, heterozygous, and homozygous CRISPR-*CCNF*<sup>S621G</sup> FFPE mouse hippocampi stained with Ms NeuN (1:200, Merck Millipore) and Rb ubiquitin (1:500, Dako). Ubiquitin staining was diffuse in the nucleus. Images taken on LSM880 confocal microscope (Zeiss) with x63 oil objective lens. Scale bar, 20 μm. n=3 biological replicates.

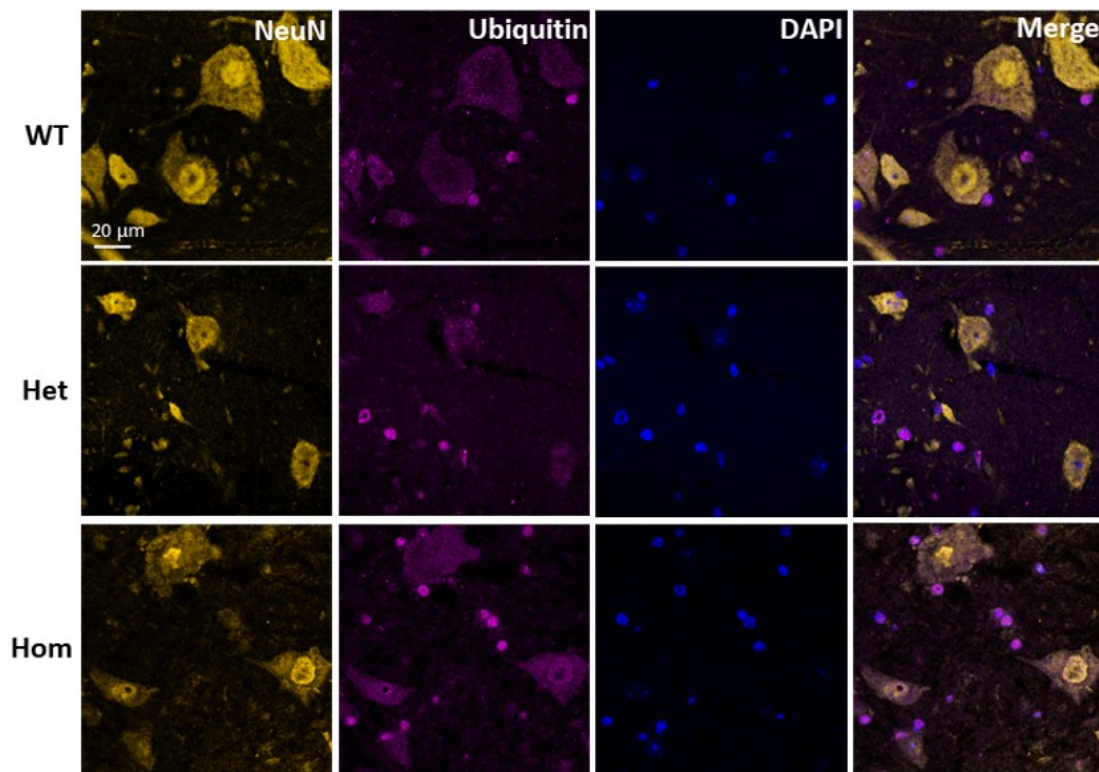


FIGURE 4.18: **Diffuse ubiquitin staining in spinal cord motor neurons from CRISPR-*CCNF*<sup>S621G</sup> mice.** WT, heterozygous, and homozygous CRISPR-*CCNF*<sup>S621G</sup> FFPE mouse spinal cord stained with Ms NeuN (1:200, Merck Millipore) and Rb ubiquitin (1:500, Dako). No ubiquitin puncta could be seen in spinal cord tissue from any genotype. The ubiquitin staining was diffuse in the nucleus and cytoplasm. Images taken on LSM880 confocal microscope (Zeiss) with x63 oil objective lens. Scale bar, 20  $\mu$ m. n=3 biological replicates.

#### Cyclin F expression in spinal cord

To investigate whether the S621G mutation led to changes in cyclin F protein level in the CRISPR-*CCNF*<sup>S621G</sup> mouse, the relative staining intensity of cyclin F (in arbitrary units, a.u.) was measured in 40 spinal cord motor neurons from each mouse using Fiji software. The average staining intensity per neuron and total staining intensity (section 3.3.1.1) was then compared across the three genotype cohorts (figure 4.19). This IF analysis approach was required because none of the cyclin F antibodies tested in this study accurately detected cyclin F from mouse tissue protein lysates in Western blot (4.3.2). There was no significant difference in the average cyclin F intensity per motor neuron between any of the cohorts (figure 4.19.a)), despite there being a decreasing trend in the homozygous CRISPR-*CCNF*<sup>S621G</sup> cohort. Also, no significant difference was seen when the total cyclin F staining intensities (from the 120 motor neurons measured) were compared between each genotype (figure 4.19.b)).

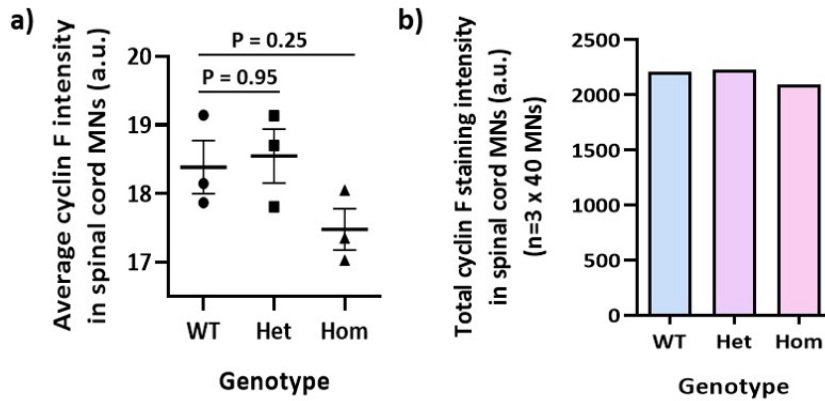


FIGURE 4.19: **Cyclin F expression was not altered in spinal cord motor neurons of mice with S621G mutation.** a) Column scatter plot of average cyclin F intensity per spinal cord motor neuron (MN), calculated from brightness of cyclin F staining in 40 motor neurons post IF staining with mouse cyclin F (1:100, Santa Cruz) primary antibody. One-way ANOVA ( $n=3$ ) with post-hoc Tukey's test was used to investigate significant differences between genotypes, mean (SEM),  $*P<0.05$ . No significant difference resulted. b) Total intensity of cyclin F staining post IF from 120 spinal cord motor neurons in each genotype ( $n=3$  biological replicates x 40 motor neurons).

## 4.2.2 Nissl staining

Severe motor neuron loss in the ventral horn of the spinal cord is a typical pathological feature in pure ALS and ALS/FTD patients (Mancuso and Navarro, 2015; Ng et al., 2015; Ragagnin et al., 2019; Vance et al., 2009). To find out whether the presence of mutant cyclin F affected motor neuron numbers in the lumbar spinal cord, 25 lumbar spinal cord sections from each WT, CRISPR-*CCNF*<sup>S621G</sup> heterozygous, and CRISPR-*CCNF*<sup>S621G</sup> homozygous mouse, were stained with cresyl violet solution (specific to Nissl substance in neurons) and the large motor neurons in the ventral horn were counted and compared between the cohorts.

### Optimisation of Nissl staining

The Nissl staining protocol was initially trialled to determine the optimal staining conditions. Two incubation times in cresyl violet solution, 13 and 15 min, were used. The 13 min incubation resulted in faint staining and the 15 min incubation showed strong staining (figure 4.20). Thus, the incubation time in cresyl violet was increased to 15 minutes for later Nissl staining experiments.

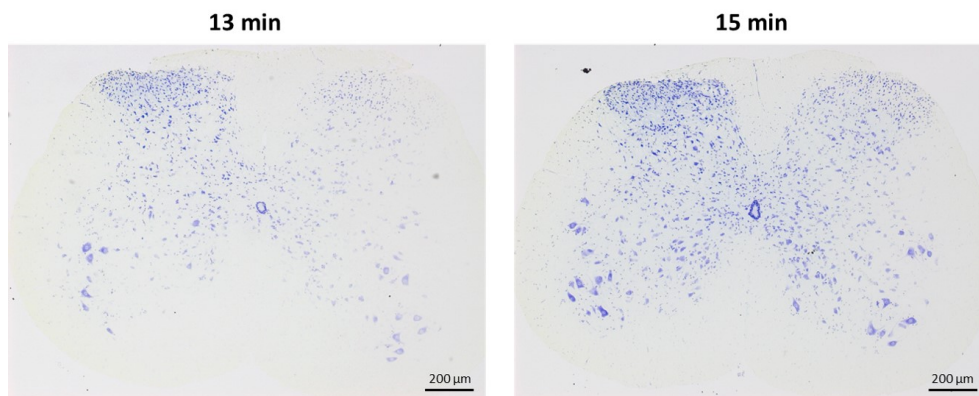


FIGURE 4.20: **Nissl stain time comparison.** The optimal time to stain spinal cord tissue in cresyl violet solution (1X) was determined to be 15 min (right-hand side image) as neurons took up the stain better. Scale bar, 200  $\mu\text{m}$ .

Nissl staining was performed on lumbar spinal cord sections as per section 3.3.2, and the number of motor neurons were quantified using Fiji image processing software. It was found that the WT cohort had the greatest total number of spinal cord motor neurons, followed by the heterozygous, and then the homozygous cohort. One-way ANOVA with multiple comparisons, resulted in a statistically significant difference between WT and homozygous counts (P-value 0.019) and between heterozygous and homozygous counts (P-value 0.027) (figure 4.21). A representative image of half a Nissl stained lumbar spinal cord section from each genotype are present in figure 4.22.

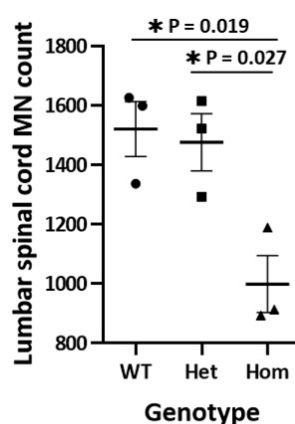


FIGURE 4.21: **Total number of lumbar spinal cord motor neurons was significantly reduced in homozygous mice compared to WT and heterozygous mice.** Column scatter plot with data points of the number of motor neurons counted in 25 spinal cord sections from L3-5, in three biological replicates per genotype. Statistical significance calculated through one-way ANOVA with multiple comparisons. Error bars represent mean  $\pm$  SEM. \*P<0.05.

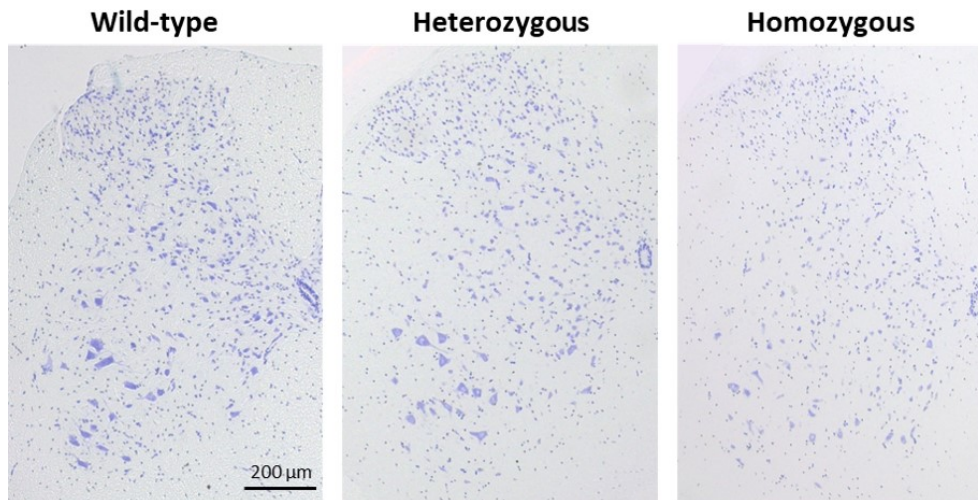


FIGURE 4.22: **Nissl stained spinal cord sections showed that homozygous CRISPR-*CCNF*<sup>S621G</sup> mice had significantly less lumbar spinal cord motor neurons than their WT and heterozygous counterparts.** From left to right, half a Nissl stained lumbar spinal cord section from a WT mouse, a heterozygous CRISPR-*CCNF*<sup>S621G</sup> mouse, and a homozygous CRISPR-*CCNF*<sup>S621G</sup> mouse. These images represent the significant loss of lumbar spinal cord motor neurons identified in the homozygous mice compared to the other genotypes. Motor neuron numbers were counted from both the left and right ventral horns of 25 Nissl stained lumbar spinal cord sections from each mouse.

### 4.3 Proteomic analysis in CRISPR-*CCNF*<sup>S621G</sup> mouse

#### 4.3.1 Mass spectrometry and protein analysis

To identify overall protein species and expression level changes associated with mutant *CCNF*, protein lysates from the mouse cohorts had previously been subjected to MS. To begin analysis of the protein data gathered from MS, Proteome Discoverer<sup>TM</sup> software was used to generate a PCA plot of relatedness of protein profiles between the mouse samples, protein abundance plots containing the spread of the amount of proteins in each sample, and volcano plots of significantly decreased and increased protein expression versus expression fold change between genotypes. Analysis of the results by PANTHER, GO, and STRING, then looked at “under-” and “over-expressed” proteins and the functional groups and biological processes they fall into.

##### 4.3.1.1 Proteomic data analysis

As a quality check of the samples, PCA plots of the protein profiles from each mouse were created to ensure similar profiles within cohorts. The PCA plot displayed both the biological replicates and the heterozygous and homozygous mouse protein profiles that

clustered (figure 4.23 a)). The box-and-whisker plot of the protein abundance values for all of the protein profiles showed a similar spread of protein abundances in each sample and similar numbers of outliers (figure 4.23 b)).

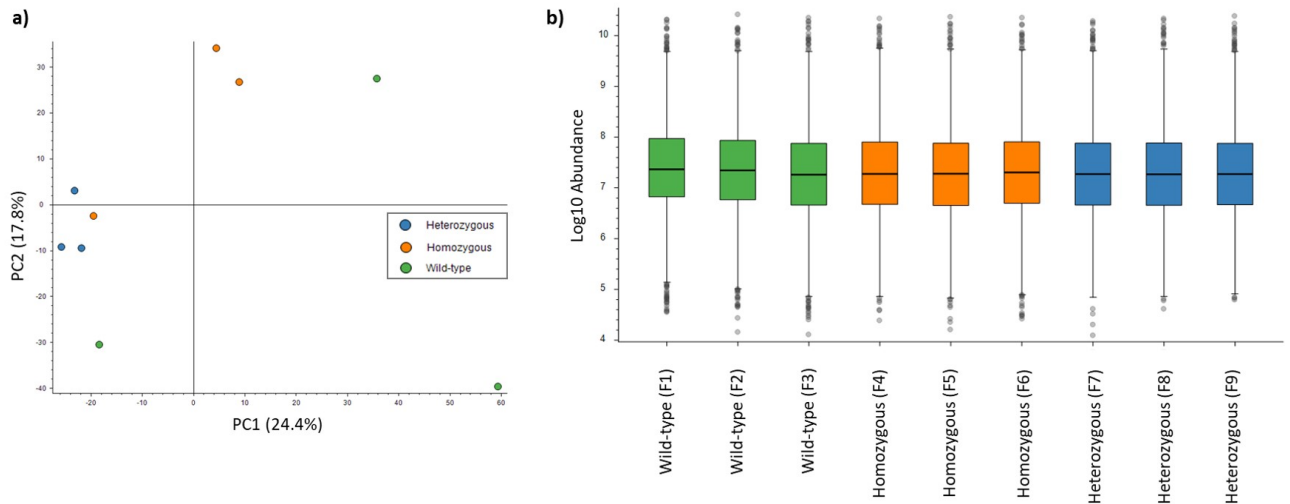


FIGURE 4.23: **Quality check of MS from brain protein lysates.** a) PCA plot showing biological similarity between samples. Blue circles represented the proteome profiles from heterozygous CRISPR-*CCNF*<sup>S621G</sup> mice, orange circles represented the proteome profiles from homozygous CRISPR-*CCNF*<sup>S621G</sup> mice, and green circles represented the proteome profiles from WT mice. b) Box-and-whisker plots of protein abundance (log<sub>10</sub> abundance) in each brain protein lysate sample from WT and heterozygous and homozygous CRISPR-*CCNF*<sup>S621G</sup> mice.

To compare protein expression profiles between genotypes, volcano plots were generated with a high FDR confidence and a significance threshold for change in expression set as  $P \leq 0.05$ . Both the heterozygous and homozygous mutant CRISPR-*CCNF*<sup>S621G</sup> mouse protein lysate profiles showed more proteins with increased expression than decreased expression when compared to WT. Comparison of the heterozygous cohort protein profile with the WT cohort profile identified 272 proteins that met the two criteria for being significantly decreased ( $P\text{-value} \leq 0.05$  and  $\log_2$  fold-change  $\leq -1.00$ ) relative to WT (figure 4.24 a)). Three-hundred proteins were decreased with a  $P\text{-value} \leq 0.05$ , and 485 had a  $\log_2$  fold-change  $\leq -1.00$ . The expression of 329 proteins was significantly increased meeting the two over-expression criteria ( $P\text{-value} \leq 0.05$  and  $\log_2$  fold-change  $\geq 1.00$ ) (figure 4.24 a)). Three-hundred and ninety-two proteins had increased expression ( $P\text{-value} \leq 0.05$ ), whilst 506 proteins had a  $\log_2$  fold-change  $\geq 1.00$  (figure 4.24 a)).

Comparison of the homozygous cohort with the WT cohort identified 204 proteins with significantly decreased expression, 219 with a  $P\text{-value} \leq 0.05$ , and 385 with a  $\log_2$  fold-change  $\leq -1.00$  (figure 4.24 b)). Four-hundred and fourteen proteins had significantly increased expression relative to WT, 462 proteins had a  $P\text{-value} \leq 0.05$ , and 551 proteins had a  $\log_2$  fold-change  $\leq -1.00$ .

The comparison of the heterozygous cohort protein profile to the homozygous cohort

showed that a greater number of proteins were significantly decreased than increased (figure 4.24 c). Two-hundred and seventy-nine proteins had significantly decreased expression, 298 had reduced expression (P-value  $\leq 0.05$  but not a great enough fold-change), and 406 had a  $\log_2$  fold-change  $\leq -1.00$ . In the heterozygous mice, 160 proteins had significantly increased expression when compared to the homozygous protein profile, 184 were increased (P-value  $\leq 0.05$ ), and 241 had a  $\log_2$  fold-change  $\geq 1.00$ .

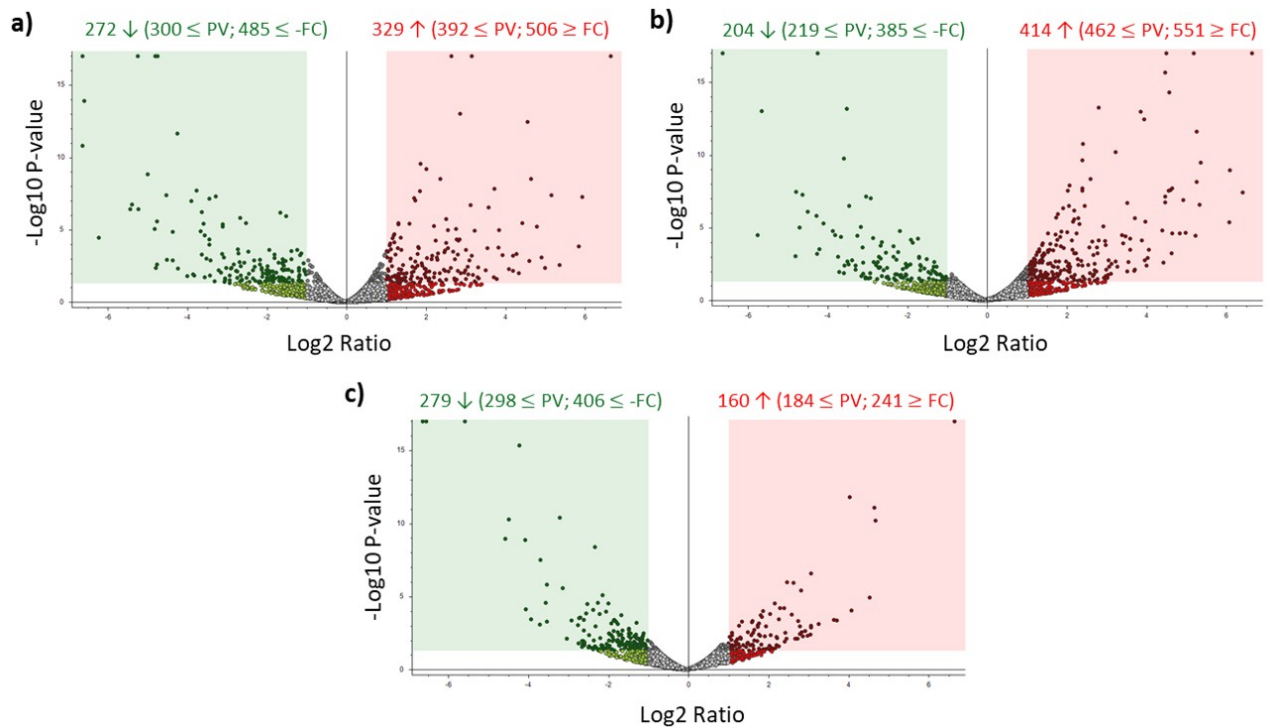


FIGURE 4.24: **Overview of protein expression changes identified in CRISPR-*CCNF*<sup>S621G</sup> brain protein lysates by MS.** Volcano plots providing graphical representation of protein expression profile comparisons. Each protein is represented by a circle. Dark green circles present in the green box on the plot are proteins that meet the two decreased-expression criteria (P-value  $\leq 0.05$  and  $\log_2$  fold-change  $\leq -1.00$ ), whilst dark red circles in the red box are proteins that meet the two increased-expression criteria (P-value  $\leq 0.05$  and  $\log_2$  fold-change  $\geq 1.00$ ). The light green and light red circles represent proteins that have  $\log_2$  fold-change  $\leq -1.00$  and  $\geq 1.00$ , respectively. a) Heterozygous protein profile compared to WT. b) Homozygous protein profile compared to WT. c) Heterozygous protein profile compared to homozygous. PV stands for P-value  $\leq 0.05$ , FC stands for  $\log_2$  fold-change either  $\leq -1.00$  or  $\geq 1.00$ .

#### 4.3.1.2 Filtering and prioritising proteomic data

Without filtering, the total number of proteins identified by MS in each genotype were 3541 in WT, 3517 in homozygous, and 3612 in heterozygous (table in figure 4.25). Three-thousand three-hundred and forty-nine proteins were shared in all three genotypes, whilst 87 proteins were unique to WT, 39 unique to heterozygous, and 89 unique to homozygous mice (venn circle in figure 4.25). There were more proteins in common between

heterozygous and homozygous mice (99) than between heterozygous and WT (30), and homozygous and WT mice (75).

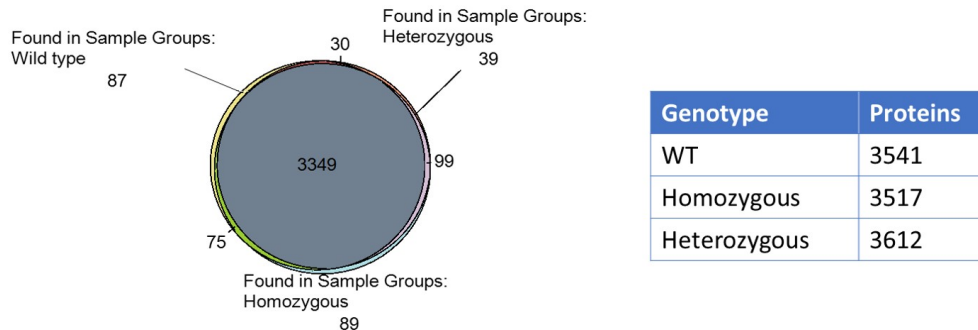


FIGURE 4.25: **Total protein numbers from MS on WT and heterozygous and homozygous CRISPR-*CCNF*<sup>S621G</sup> brain protein lysates.** The circle on the left represents the overlap of all the proteins detected in MS between the three genotype cohorts. Three thousand, three hundred and forty-nine proteins were shared between all cohorts. The table on the right displays the total number of proteins detected in each genotype (n=3 biological replicates).

The MS data was examined for expression of cyclin F. However, cyclin F was not detected in any of the three mouse cohorts, likely due to low expression level, as MS is known to detect proteins that are more highly expressed. Other proteins of interest in the ALS/FTD field, including those reported as associated with *CCNF*-linked ALS/FTD, were also screened in the proteomic data set (table 5.1).

The filtering and stringent selection criteria that were applied to the 4,079 proteins detected by MS reduced the numbers into purposeful and workable groups (methods section 3.4.3.1). The first filter of “high protein FDR confidence” decreased the number of proteins to 3,760. Next, the “over-expression” filter (3.4.3.1) was applied to assess the possibility that mutation of cyclin F leads to an increase of function in other proteins and therefore any protein changes would be more heightened in the homozygous CRISPR-*CCNF*<sup>S621G</sup> mice compared to the heterozygotes. There were 90 proteins that met the “over-expression” criteria. The “under-expression” filter was applied to investigate whether mutant cyclin F induced a decrease in function of other proteins, which would result in a greater down-regulation of proteins in CRISPR-*CCNF*<sup>S621G</sup> homozygous mice compared to heterozygotes. When the “under-expression” filter was applied to the 3,760 “high FDR confidence” proteins, the number of proteins was reduced to 564.

#### 4.3.1.3 Protein classification, gene ontology, and network analysis

Functional classification of the 90 “over-expression” proteins using PANTHER software identified 71 functional protein hits, which were sorted into 7 molecular function categories: “binding”, “catalytic activity”, “molecular function regulator”, “molecular transducer activity”, “structural molecule activity”, “transcription regulator activity”, and

“transporter activity” (figure 4.26). The most abundant category “binding” (29 hits, 41% total “over-expressed” proteins) was selected and as the level 2 category it held 12 more specific binding categories. The “protein binding” category had the most hits (11) and so it was selected as the level 3 category. As cytoskeletal proteins are highly abundant, they consequently commonly appear in MS results and act as contaminants (Radulovic and Godovac-Zimmermann, 2011). It was for this reason that despite “cytoskeletal proteins” being the largest level 4 category, it was not examined further. The resulting genes from the next largest level 4 categories “cell adhesion molecule binding” and “enzyme binding” were investigated and are noted in table 4.7.

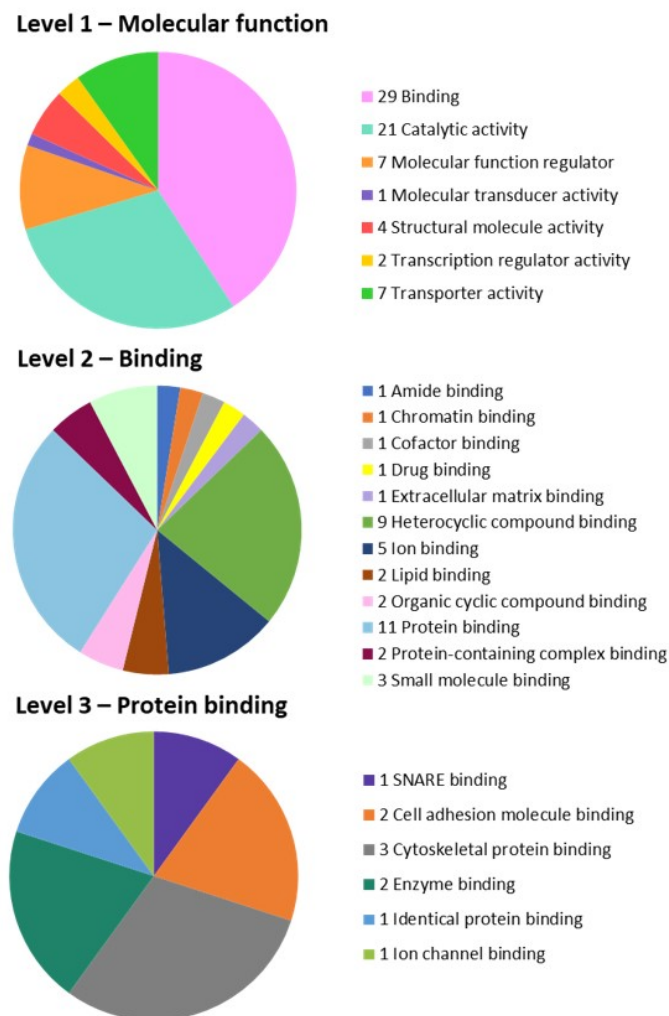


FIGURE 4.26: **Functional classification of unregulated (“over-expressed”) proteins in the CRISPR-*CCNF*<sup>S621G</sup> model – PANTHER analysis.** When the PANTHER software was used to analyse the 90 proteins that had increased expression in the CRISPR-*CCNF*<sup>S621G</sup> mice, they were broken down into categories in four levels of molecular functions. The categories with the greatest number of proteins were: level 1 - molecular function, level 2 - binding, level 3 - protein binding, level 4 - cell adhesion molecule binding, and enzyme binding.

Three of the final four “over-expressed” proteins *AFDN*, *ARVCF*, and *GAPVD1* have not been strongly associated with ALS/FTD before. However, *CDC42* has been investigated in FTD (Saraceno et al., 2018), and its potential influence in neuronal development, neuronal survival, and neurodegeneration studied (Stankiewicz and Linseman, 2014).

TABLE 4.7: “Over-expression” results from lowest level of PANTHER molecular function analysis.

Category	Gene symbol	Abundance ratio: (Het/WT)	Abundance ratio: (Hom/WT)
Cell adhesion	<i>AFDN</i>	2.932	3.899
molecule binding	<i>ARVCF</i>	18.261	22.020
Enzyme binding	<i>CDC42</i>	3.636	3.728
	<i>GAPVD1</i>	27.538	41.126

GO analysis of the 90 “over-expression” proteins identified six biological process categories (table 4.8).

TABLE 4.8: “Over-expressed” biological processes in CRISPR-*CCNF*<sup>S621G</sup> mice.

GO biological process
Complete localisation within membrane
Membrane organisation
Positive regulation of transport
Cellular protein localisation
Cellular component assembly
Organelle organisation

The 564 proteins with reduced expression that met the “under-expression” criteria were broken down into eight levels of molecular function categories (figure 4.27). At the highest level, “catalytic activity” was the largest category (232 proteins, 41% total “under-expressed” proteins). When it was investigated at the next level, “hydrolase activity” with 95 proteins, was the largest category. At this third level, 43 proteins had “hydrolase activity, acting on acid anhydrides”. From levels 4 to 6, the proteins could not be separated into different groups and numbers reduced. Lastly, at level 7 the proteins were separated based on their nucleoside-triphosphatase activity, with the level 8 category “GTPase activity” being the largest (26 proteins).



FIGURE 4.27: **Functional classification of “under-expressed” proteins in the CRISPR-*CCNF*<sup>S621G</sup> model – PANTHER analysis.** The proteins with decreased expression in the CRISPR-*CCNF*<sup>S621G</sup> model could be categorised into seven levels of molecular function. At each level, the category with the largest number of protein hits was selected to be investigated further.

The 26 resulting proteins from PANTHER analysis with “GTPase activity” are listed in table 4.9. Notable targets include *GNAI2*, *TBC1D15*, and the *RAB* genes.

TABLE 4.9: Final “under-expression” results from PANTHER molecular function analysis - GTPase activity

Gene symbol	Abundance ratio: (Het/WT)	Abundance ratio: (Hom/WT)
<i>ADPRH</i>	0.915	0.699
<i>ARHGAP1</i>	0.945	0.913
<i>GNA11</i>	0.772	0.589
<i>GNA13</i>	0.906	0.656
<i>GNAI2</i>	0.965	0.773
<i>GNAI3</i>	0.952	0.671
<i>GNAQ</i>	0.96	0.797
<i>GNAS</i>	0.904	0.86
<i>GNB4</i>	0.976	0.854
<i>RAB12</i>	0.963	0.962
<i>RAB35</i>	0.738	0.516
<i>RAB3GAP1</i>	0.986	0.907
<i>RAB9B</i>	0.301	0.224
<i>RHEB</i>	0.732	0.57
<i>RHOT1</i>	0.876	0.855
<i>RIC8; RIC8A</i>	0.778	0.41
<i>RRAGC</i>	0.738	0.54
<i>SEC23A</i>	0.917	0.744
<i>SEPT11</i>	0.939	0.826
<i>SEPT2</i>	0.795	0.556
<i>SEPT3</i>	0.929	0.838
<i>SEPT4</i>	0.742	0.68
<i>SEPT5</i>	0.881	0.782
<i>SEPT7</i>	0.869	0.813
<i>TBC1D15</i>	0.255	0.233
<i>TBC1D9B</i>	0.169	0.144

With the workable number of 26 proteins, protein network analysis was performed using STRING software (figure 4.28). Four clusters of proteins were identified from the STRING network — guanine nucleotide-binding protein cluster, ras-related protein cluster, septin cluster, and GTP binding protein cluster. A network made from four proteins (gene symbols *RAB35*, *TBC1D15*, *RHOT1*, and *ARHGAP1*) connects two of the protein clusters (ras-related protein cluster, guanine nucleotide-binding protein cluster). Reactome

pathways such as signal transduction (HSA-162582), signal amplification (HSA-392518), regulation of insulin secretion (HSA-422356), rab regulation of trafficking (HSA-9007101), haemostasis (HSA-109582), membrane trafficking (HSA-199991), GPCR downstream signalling (HSA-388396), and protein metabolism (HSA-392499), were strongly connected to the down-regulated proteins, having five or more of the proteins associated with them.

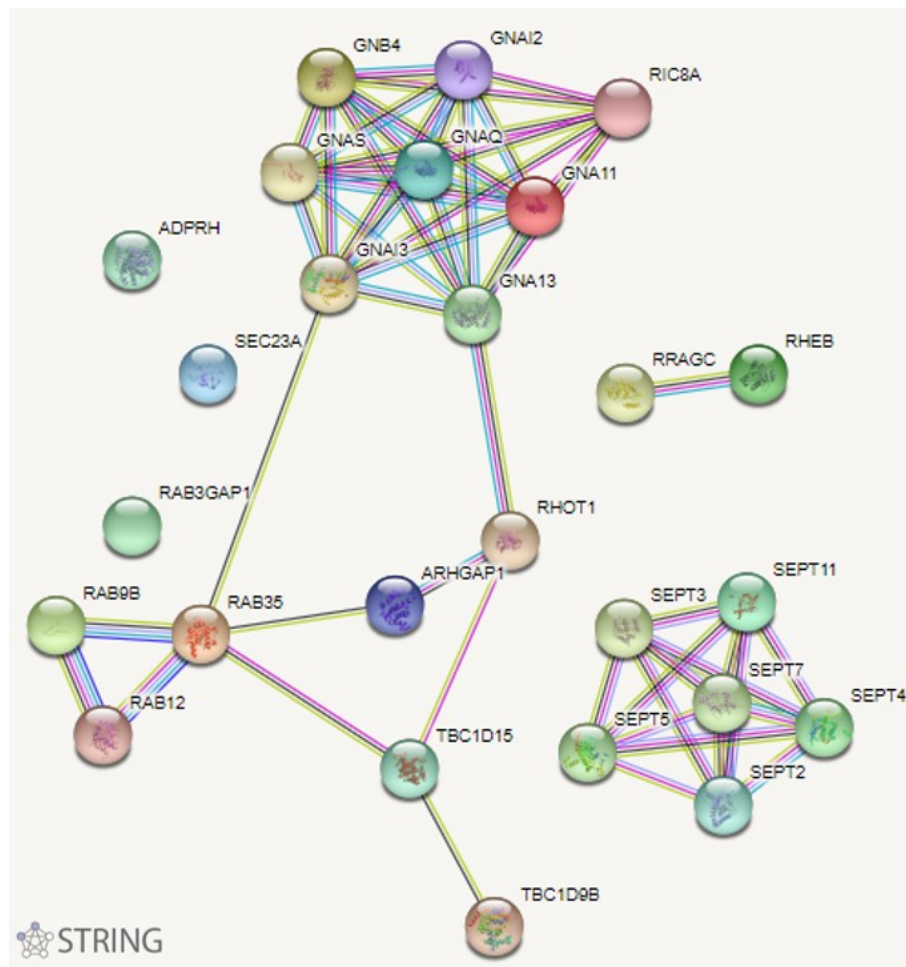


FIGURE 4.28: Network between the “under-expressed” proteins in CRISPR-*CCNF*<sup>S621G</sup> mice. The “under-expressed” proteins identified in brain protein lysates from CRISPR-*CCNF*<sup>S621G</sup> mice could be linked into an interaction network that was created using STRING (Search Tool for the Retrieval of Interacting Genes/Proteins). The network illustrated four clusters of proteins.

GO analysis of the 564 “under-expressed” proteins identified 88 associated biological process categories (A.2.1.1), 29 of which were relevant to ALS/FTD or mutant *CCNF* and mutant cyclin F protein (table 4.10).

TABLE 4.10: **GO biological processes associated with ALS relevant “under-expressed” proteins**

Positive regulation of autophagosome assembly
Positive regulation of neuron projection development
Synaptic signalling
Intracellular signal transduction
Neuron projection morphogenesis
Protein targeting
Response to oxidative stress
Regulation of actin filament organisation
Positive regulation of cytoskeleton organisation
Neutrophil degranulation
Negative regulation of protein kinase activity
Regulation of vesicle-mediated transport
Positive regulation of protein complex assembly
Peptidyl-serine phosphorylation
Mitotic prometaphase
Positive regulation of cell morphogenesis involved in differentiation
Ribonucleoprotein complex assembly
Establishment of protein localisation to endoplasmic reticulum
Regulation of extent of cell growth
Actin filament organisation
Translational initiation
Cytoskeleton-dependent cytokinesis
Protein folding
Positive regulation of attachment of spindle microtubules to kinetochore
IRE1-mediated unfolded protein response
Regulation of microtubule polymerisation
COPII vesicle coating
Regulation of mRNA processing
mRNA splicing, via spliceosome

### 4.3.2 Western blot

Western blot experiments were carried out to quantify and compare the level of cyclin F protein and the expression of other proteins of interest, in the brains of WT and CRISPR-*CCNF*<sup>S621G</sup> heterozygous and homozygous mice.

The first Western blots, using cyclin F and TDP-43 antibodies, were performed to validate if there were protein level changes in any of the WT and/or CRISPR-*CCNF*<sup>S621G</sup> heterozygous and homozygous mouse brain lysates (section 3.4.4). The initial Western

blot was unsuccessful as the Ponceau stained membrane (for detection of total proteins on the membrane) indicated incomplete transfer (figure A.1). The Western blot was repeated, and the Ponceau stained membrane showed protein transfer was successful (figure 4.29.b)). However, no clear cyclin F band at 87 kDa (the protein's molecular weight) or 110 kDa (reported antibody detection size) was observed (figure 4.29.a)). Instead, bands were seen at around 140 kDa, and 60 kDa. It was possible that the band at 140 kDa could have been cyclin F but validation through further experiments was required. Strong bands for TDP-43 at 43 kDa and GAPDH at 36 kDa were present in all samples. TDP-43 expression level in each sample was calculated by normalising the signal intensity from the TDP-43 band, to that from the loading control, GAPDH. Statistical analysis through one-way ANOVA with multiple comparisons was performed on the relative TDP-43 signal intensities and the data plotted in a column scatter plot (figure 4.29.c)). There was no statistically significant difference in relative TDP-43 intensity between the genotypes, signifying that mutant cyclin F protein did not affect TDP-43 expression.

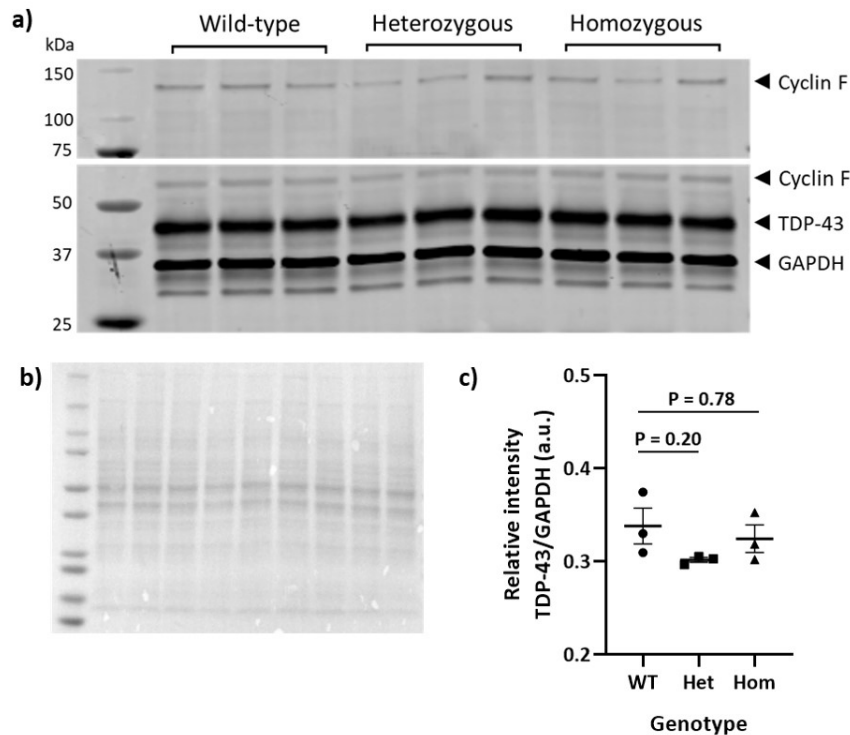
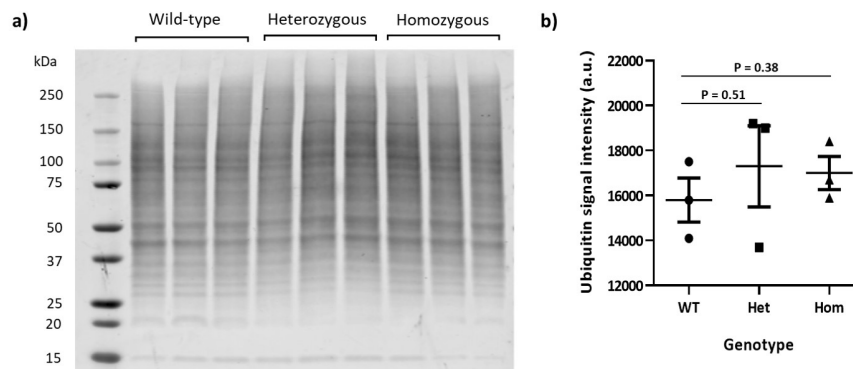


FIGURE 4.29: **TDP-43 protein expression level was not altered in CRISPR-*CCNF*<sup>S621G</sup> mice.** a) Western blot image (Odyssey CLx) from round 2 Western blot of every (from L→R) WT (#4, #15, #7), heterozygous (#14, #16, #9), and homozygous (#3, #8, #17) mouse brain protein lysate sample, stained for cyclin F (rabbit, 1:500, Santa Cruz), TDP-43 (rabbit, 1:1,000, ProteinTech), and loading control GAPDH (mouse, 1:5,000, ProteinTech). Black arrowheads point to TDP-43 at 43 kDa, GAPDH at 36 kDa, and potential cyclin F bands at 140 kDa and 60 kDa. Marker: precision plus protein<sup>TM</sup> dual colour standard ladder (Bio-Rad). b) Ponceau S stained membrane displayed uniform protein transfer across the lanes. c) Column scatter plot of relative TDP-43 protein expression of each sample and genotype. One-way ANOVA with multiple comparisons showed no significant reductions or increases between genotypes. Error bars represent mean ± SEM.

Next, a ubiquitin antibody was used to see whether there was an increase in ubiquitinated proteins, one of the pathological hallmarks of ALS, in the CRISPR-*CCNF*<sup>S621G</sup> mice. The ubiquitin stain showed a characteristic smear in all of the samples (figure 4.30.a)), and quantification of ubiquitin staining intensity revealed no significant difference in ubiquitin signal between the three genotypes (figure 4.30.b)). This suggested that there was no major change in ubiquitin protein levels related to the presence of mutant cyclin F.



**FIGURE 4.30: Ubiquitin levels unaffected by mutant cyclin F protein.** a) Western blot image (Odyssey CLx) from Western blot of every (from L→R) WT (#4, #15, #7), heterozygous (#14, #16, #9), and homozygous (#3, #8, #17) mouse brain protein lysate sample, stained for ubiquitin (rabbit, 1:500, Dako). Dark ubiquitin smear present down each lane from around 250 kDa to 20 kDa in reference to the precision plus protein<sup>TM</sup> dual colour standard ladder (Bio-Rad). b) Column scatter plot of ubiquitin signal intensity of each sample and genotype. One-way ANOVA (n=3 biological replicates) with multiple comparisons showed no significant reductions or increases between genotypes. Error bars represent mean  $\pm$  SEM.

Given the previously inconclusive staining of cyclin F, an optimisation strategy was used for subsequent Western blots including assessment of multiple cyclin F primary antibodies. To conserve mouse protein lysate samples, only one lysate sample from #4(WT) was loaded on each gel in repeat alongside the protein ladder, the Western blot membrane was cut into strips, and each strip stained separately with: mouse cyclin F (1:100 or 1:250, Santa Cruz), and rabbit cyclin F (1:500 or 1:750, ThermoFisher). Different imaging approaches (wet and dry blots) were also used, as manufacturer technical notes suggested that imaging the blots dry could enhance the antibody signal ([Li-Cor Biosciences, 2019](#)). No cyclin F band was detected at the expected size when the mouse cyclin F (1:100, Santa Cruz) was applied and the blot was imaged wet. However, when it was imaged dry, there was a faint band at 110 kDa, possibly indicating low expression of cyclin F (figure 4.31.a). This faint band was absent on the blot that used 1:250 concentration of the mouse cyclin F (Santa Cruz) antibody (figure 4.31.b). The rabbit cyclin F (ThermoFisher) at either 1:500 and 1:750 did not produce a cyclin F band (figure 4.31.c) and d)). As GAPDH bands were strong in the previous Western blot, the GAPDH concentration was decreased to 1:6,000 in subsequent blots. This reduction still produced clear GAPDH bands at 36 kDa when the #4(WT) blot strips were imaged both wet and dry (figure 4.31).

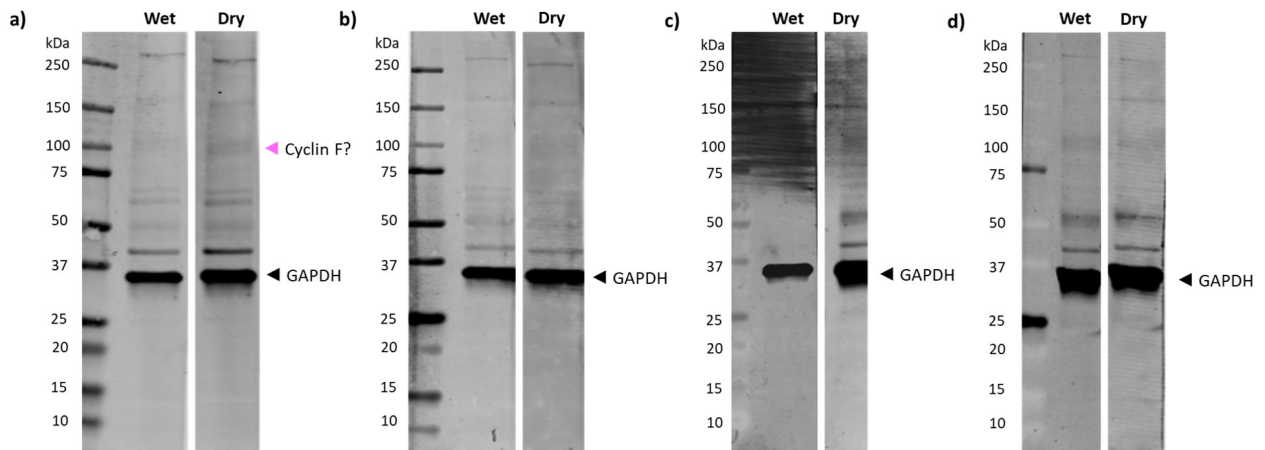
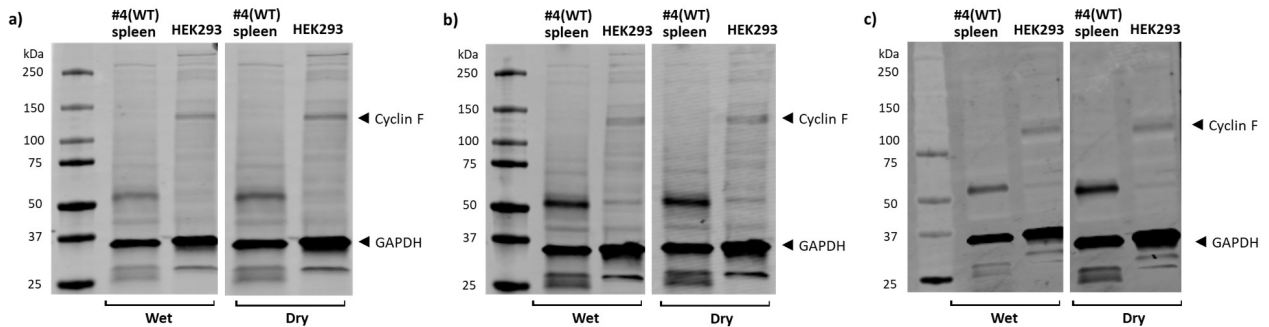


FIGURE 4.31: **No specific cyclin F band was detected in mouse brain lysate when using Santa Cruz or ThermoFisher cyclin F antibodies.** Images of wet (left) and dry (right) Western blot strips of #4(WT) mouse brain protein lysate stained with various cyclin F antibodies and combinations. a) Mouse cyclin F (1:100, Santa Cruz) and mouse GAPDH (1:6,000, ProteinTech). Pink arrowhead points to the slight darkening at 110 kDa, which could be cyclin F, in the dry image. b) Mouse cyclin F (1:250, Santa Cruz) and mouse GAPDH (1:6,000, ProteinTech). c) Rabbit cyclin F (1:500, ThermoFisher) and mouse GAPDH (1:6,000, ProteinTech). d) Rabbit cyclin F (1:750, ThermoFisher) and mouse GAPDH (1:6,000, ProteinTech). Images taken using Odyssey CLx (Li-Cor) and display the loading control, GAPDH, at 36 kDa. Precision plus protein<sup>TM</sup> dual colour standard ladder (Bio-Rad) used as a reference in all.

The lack of a clear cyclin F band could have been due to low cyclin F expression in mouse CNS tissues or incompatibility of the antibodies to Western blot with mouse tissue lysate. To test this and to test if the antibodies would work with lysate from a human cell line, a fourth Western blot was performed on mouse non-CNS tissue lysate and human cell line (HEK293) lysate. Spleen tissue lysate was selected, as cyclin F is more highly expressed in the spleen than the brain (Uhlén et al. (2015), <https://www.proteinatlas.org/ENSG00000162063-CCNF/tissue>). As shown in figure 4.32, in the HEK293 lysates, a band was consistently seen at 140 kDa when each antibody (mouse (1:100 and 1:500, Santa Cruz), and rabbit (1:500, Santa Cruz)) was used. This may have been cyclin F, but further validation is required to confirm this. None of the cyclin F antibodies produced a definitive cyclin F band in the #4(WT) mouse spleen lysate. Again, protein signals were stronger in blots imaged dry and clear GAPDH bands were present in both HEK293 and #4(WT) mouse spleen protein lysates. Non-specific bands were also present around 25, 30, and 55 kDa in #4 mouse spleen lanes, and around 30 kDa in HEK293 lanes.



**FIGURE 4.32: Cyclin F was unidentifiable in mouse spleen protein lysate by Western blot but speculatively apparent in HEK293 lysate.** Images of wet (left) and dry (right) Western blot strips of #4(WT) mouse spleen and HEK293 protein lysates stained with various cyclin F antibodies and combinations. a) Mouse cyclin F (1:100, Santa Cruz) and mouse GAPDH (1:6,000, ProteinTech). b) Mouse cyclin F (1:500, Santa Cruz) and mouse GAPDH (1:6,000, ProteinTech). c) Rabbit cyclin F (1:500, Santa Cruz) and mouse GAPDH (1:6,000, ProteinTech). Images taken using Odyssey CLx (Li-Cor) and display the loading control, GAPDH (36 kDa), and potential cyclin F (140 kDa). Precision plus protein<sup>TM</sup> dual colour standard ladder (Bio-Rad) used as a reference in all.

A final Western blot experiment was performed to determine whether the cyclin F antibodies simply did not work with mouse tissue lysates, and whether cyclin F bands at 87 kDa and 110 kDa (as claimed in the manufacturers data sheet) could be obtained. Lysates from the mouse cell line, neuro-2a, were used. The mouse cyclin F (Santa Cruz) antibody did not demonstrate a band at the expected size, but the rabbit cyclin F antibody did generate two bands at around 100 to 120 kDa. However, non-specific bands were also evident.

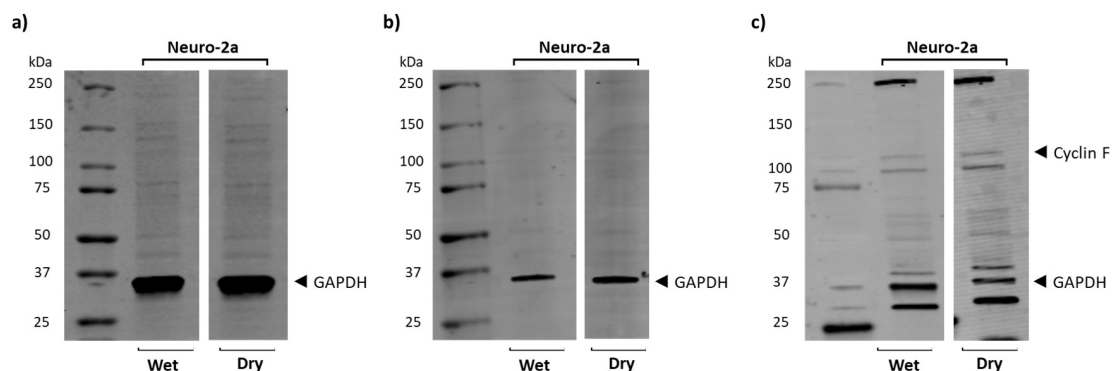


**FIGURE 4.33: Mouse cyclin F (Santa Cruz) antibody.** Images of wet (left) and dry (right) Western blot strips of neuro-2a protein lysates stained with various cyclin F antibodies and combinations a) Mouse cyclin F (1:100, Santa Cruz) and mouse GAPDH (1:6,000, ProteinTech). b) Mouse cyclin F (1:500, Santa Cruz) and mouse GAPDH (1:6,000, ProteinTech). c) Rabbit cyclin F (1:500, Santa Cruz) and mouse GAPDH (1:6,000, ProteinTech). Images taken using Odyssey CLx (Li-Cor) and display the loading control, GAPDH (36 kDa), and speculated cyclin F (140 kDa). Precision plus protein<sup>TM</sup> dual colour standard ladder (Bio-Rad) used as a reference in all.

To summarise the Western blot experiments, various cyclin F antibodies were applied to Western blots with protein lysates from CRISPR-*CCNF*<sup>S621G</sup> mice brain and spleen tissue, and from HEK293 and neuro-2a cells, to test antibody specificity. The most promising indication of a cyclin F band around 100 to 110 kDa was in Neuro-2a lysate, when rabbit cyclin F (1:500, Santa Cruz) was used. In other blots, the “cyclin F” band always sat higher than expected, at 140 kDa, which was seen in mouse brain lysate when rabbit cyclin F (1:500, Santa Cruz) was used and in HEK293 lysate when rabbit and mouse cyclin F (Santa Cruz) antibodies were used. It was also established that imaging blots dry gave stronger protein band signals compared to when imaged wet. As the results did not provide a definitive cyclin F band in mouse tissue lysate, it was evident the antibodies were not compatible, and the study moved onto an alternative quantitative approach using RT-qPCR.

### 4.3.3 RNA extraction and RT-qPCR

The cyclin F IF staining of spinal cord tissue suggested that the S621G mutation did not affect *CCNF* expression. This could not be accurately or reliability reproduced by Western blot, so RT-qPCR was used to quantify *CCNF* expression. No further brain, and only three spinal cord tissue samples were available from the CRISPR-*CCNF*<sup>S621G</sup> mice, so quantification of *CCNF* in these three spinal cord tissues and in all the mouse spleen tissues was performed. Cyclin F expression in spleen tissue is greater than that in both brain and spinal cord tissue (Uhlén et al. (2015), <https://www.proteinatlas.org/ENSG00000162063-CCNF/tissue>), so it was expected that the RT-qPCR results would yield values greater than that from the brain and spinal cord. However, the focus of analysis was the difference in cyclin F expression between genotypes not tissue types, so the type of tissue used would not affect the overall outcome as the mutation was stably integrated into the CRISPR-*CCNF*<sup>S621G</sup> mice genomes and therefore be ubiquitously expressed.

RNA was extracted from the spinal cord and spleen samples as described in section 3.4.5.1. Analysis of the RNA with a NanoDrop 2000 spectrophotometer (ThermoFisher), demonstrated that all the absorbance 260/280 nm (A260/280) ratios were close to 2.00, indicating high RNA purity (table 4.11). The RNA concentrations for all samples, except spleen #7(WT) and spinal cord #15(WT), indicated typical yields for the tissue type (for example 3,600 ng/ $\mu$ L RNA from mouse spleen) stated in the RNeasy<sup>®</sup> Mini Handbook.

TABLE 4.11: Nucleic acid concentrations and purity of mouse spleen RNA.

RNA sample	Nucleic acid (ng/ $\mu$ L)	A260/280
Spleen #4(WT)	3,094.80	2.11
Spleen #7(WT)	494.00	2.09
Spinal cord #15(WT)	22.01	2.06
Spleen #15(WT)	2,566.1	2.11
Spleen #9(Het)	5,238.30	2.07
Spleen #14(Het)	3,712.40	2.09
Spinal cord #16(Het)	355.0	2.07
Spleen #16(Het)	4,434.10	2.10
Spleen #3(Hom)	3,502.20	2.08
Spleen #8(Hom)	2,863.80	2.06
Spinal cord #17(Hom)	290.7	2.07
Spleen #17(Hom)	4,476.60	2.09

cDNA was reverse transcribed from this RNA and qPCR performed as described in section 4.3.3. To optimise qPCR, a single spleen-derived sample #15(WT) underwent qPCR using a *Ccnf* specific Taqman<sup>TM</sup> assay and a reference control *ACTB* (Beta actin) assay. The *ACTB* (actin) assay utilised a FAM-tagged primer and the *CCNF* (cyclin F) assay a VIC-tagged primer. Amplification was successful, demonstrating sufficient nucleic acid template, with Ct (cycle threshold) values for the *CCNF* duplicates less than or equal to 30. Multiplex qPCR with both the *ACTB* (FAM) and *CCNF* (VIC) primers generated similar *CCNF* Ct values to when *CCNF* (VIC) primers were used on their own. As such, multiplex qPCR was performed for subsequent assays.

The preliminary qPCR data (table 4.12), obtained in triplicate for each genotype, are listed in table 4.13. All of the Ct values were less than or equal to 30, which indicated that there was sufficient template within each sample. The preliminary fold-change expression data from each sample showed that *CCNF* expression was reduced in the heterozygous mice and increased in the homozygous mice when compared to WT mice.

TABLE 4.12: qPCR data and calculation terminology

qPCR data term	Symbol	Meaning
Cycle threshold value	Ct	The number of PCR cycles that occur before the amplified transcript fluorescent signal is greater than the background level.
Mean cycle threshold	Ct mean	Average of the Ct triplicates.
Delta Ct mean	$\Delta Ct$	$Ct(CCNF)_{\text{mean}} - Ct(ACTB)_{\text{mean}}$ .
Difference between delta Ct experimental mean value and delta control (WT) mean value	$\Delta\Delta Ct$	$\Delta Ct - \text{average of } \Delta Ct(\text{WT})$ . Difference between the change in <i>CCNF</i> Ct mean and change in <i>ACTB</i> Ct mean.
Fold expression	$2^{-\Delta\Delta Ct}$	Fold change in <i>CCNF</i> expression relative to WT.
Average fold expression	Average $2^{-\Delta\Delta Ct}$	Fold expression $\div$ the # of sample or biological replicates.

TABLE 4.13: Preliminary qPCR data

Sample	Ct	Ct mean	$\Delta Ct$	$\Delta\Delta Ct$	Fold expression	Average fold expression
Spinal cord #15 (WT)						
TriPLICATE 1 (CCNF)	29.86	29.92	7.87	0.06	0.96	1.00
TriPLICATE 1 (ACTB)	22.229	22.107				
TriPLICATE 2 (CCNF)	30.13		8.02	0.21	0.86	
TriPLICATE 2 (ACTB)	21.991					
TriPLICATE 3 (CCNF)	29.76		7.54	-0.27	1.21	
TriPLICATE 3 (ACTB)	22.102					
Spinal cord #16 (Het)						0.61
TriPLICATE 1 (CCNF)	25.81	26.17	8.36	0.55	0.68	
TriPLICATE 1 (ACTB)	17.454	17.651				
TriPLICATE 2 (CCNF)	26.32		8.74	0.93	0.53	
TriPLICATE 2 (ACTB)	17.582					
TriPLICATE 3 (CCNF)	26.37		8.46	0.65	0.64	
TriPLICATE 3 (ACTB)	17.916					
Spinal cord #17 (Hom)						1.78
TriPLICATE 1 (CCNF)	27.67	27.865	6.91	-0.90	1.87	
TriPLICATE 1 (ACTB)	20.763	20.887				
TriPLICATE 2 (CCNF)	28.25		7.24	-0.57	1.49	
TriPLICATE 2 (ACTB)	21.014					
TriPLICATE 3 (CCNF)	27.67		6.79	-1.02	2.03	
TriPLICATE 3 (ACTB)	20.883					

The qPCR on spleen cDNA from all samples from each genotype revealed no significant difference in *CCNF* expression between the WT, heterozygous, and homozygous *CCNF* genotypes. Minor decreases in average fold change *CCNF* expression were seen in heterozygous and homozygous when compared to WT (figure 4.34). The raw qPCR data values and calculated results for  $\Delta Ct$ ,  $\Delta\Delta Ct$ , and fold expressions are located in table 4.14. Amplification was low for *ACTB* in sample #7(WT) (high Ct value). Also, only a single low Ct value compared to the other WT Ct values, was obtained for #4(WT) *CCNF*. As such, the #7(WT) results were not included in further analyses. The Ct mean values were variable between the two samples in WT and in heterozygous mouse samples (figure 4.34.a). This may explain why the average fold-change expression of *CCNF* in the WT cohort was greater than 1.

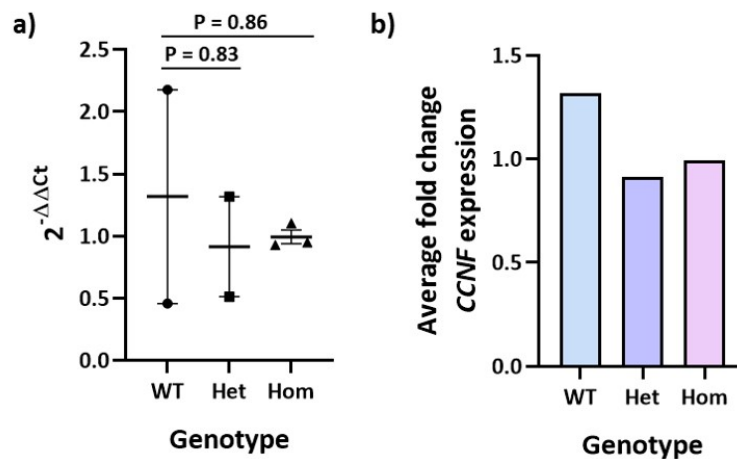


FIGURE 4.34: qPCR showed that the S621G mutation did not significantly alter *CCNF* gene expression in mouse spleen tissues. a) Column scatter graph (mean, SEM) of WT, and heterozygous and homozygous CRISPR-*CCNF*<sup>S621G</sup> mouse spleen protein lysate *CCNF* fold expression ( $2^{-\Delta\Delta Ct}$ ). There was no statistically significant difference (one-way ANOVA with multiple comparisons,  $P < 0.05$ ) in *CCNF* fold expression between any of the mouse cohorts. Error bars represent mean  $\pm$  SEM. b) Bar chart of average fold change *CCNF* expression in WT, and heterozygous and homozygous CRISPR-*CCNF*<sup>S621G</sup> mouse spleen protein lysates. n=3 biological replicates in triplicate.

TABLE 4.14: Spleen tissue qPCR data

Sample	Ct	Ct mean	$\Delta$ Ct	$\Delta\Delta$ Ct	Fold expression	Average fold expression
Spleen #4 (WT)						1.319
Triplicate 1 (CCNF)	28.911	28.764	10.768	1.124	0.459	
Triplicate 1 (ACTB)	18.004	17.996				
Triplicate 2 (CCNF)	29.301					
Triplicate 2 (ACTB)	18.278					
Triplicate 3 (CCNF)	28.081					
Triplicate 3 (ACTB)	17.705					
Spleen #7 (WT)			Not included in analysis			
Triplicate 1 (CCNF)	Undetermined	16.598				
Triplicate 1 (ACTB)	35.166	36.872				
Triplicate 2 (CCNF)	16.598					
Triplicate 2 (ACTB)	36.012					
Triplicate 3 (CCNF)	Undetermined					
Triplicate 3 (ACTB)	39.438					
Spleen #15 (WT)						
Triplicate 1 (CCNF)	26.600	26.433	8.521	-1.124	2.179	
Triplicate 1 (ACTB)	18.074	17.912				
Triplicate 2 (CCNF)	26.265					
Triplicate 2 (ACTB)	17.672					
Triplicate 3 (CCNF)	26.435					
Triplicate 3 (ACTB)	17.990					
Spleen #9 (Het)			Not included in analysis			0.916
Triplicate 1 (CCNF)	Undetermined	n/a				
Triplicate 1 (ACTB)	Undetermined	36.243				
Triplicate 2 (CCNF)	Undetermined					
Triplicate 2 (ACTB)	Undetermined					
Triplicate 3 (CCNF)	Undetermined					
Triplicate 3 (ACTB)	36.243					
Spleen #14 (Het)						
Triplicate 1 (CCNF)	29.480	29.301	10.604	0.959	0.514	
Triplicate 1 (ACTB)	19.046	18.698				
Triplicate 2 (CCNF)	29.287					
Triplicate 2 (ACTB)	18.351					
Triplicate 3 (CCNF)	29.137					
Triplicate 3 (ACTB)	18.696					
Spleen #16 (Het)						
Triplicate 1 (CCNF)	26.504	26.542	9.247	-0.398	1.318	
Triplicate 1 (ACTB)	17.378	17.295				
Triplicate 2 (CCNF)	26.593					
Triplicate 2 (ACTB)	17.232					
Triplicate 3 (CCNF)	26.528					
Triplicate 3 (ACTB)	17.275					

Table 4.14 continued...

Spleen #3 (Hom)						
Triplicate 1 (CCNF)	30.270	30.086	9.749	0.104	0.930	0.995
Triplicate 1 (ACTB)	20.354	20.337				
Triplicate 2 (CCNF)	29.415					
Triplicate 2 (ACTB)	20.265					
Triplicate 3 (CCNF)	30.572					
Triplicate 3 (ACTB)	20.391					
Spleen #8 (Hom)						
Triplicate 1 (CCNF)	29.885	28.891	9.718	0.073	0.951	
Triplicate 1 (ACTB)	19.266	19.174				
Triplicate 2 (CCNF)	28.730					
Triplicate 2 (ACTB)	19.034					
Triplicate 3 (CCNF)	28.059					
Triplicate 3 (ACTB)	19.221					
Spleen #17 (Hom)						
Triplicate 1 (CCNF)	27.741	27.671	9.500	-0.144	1.105	
Triplicate 1 (ACTB)	18.083	18.171				
Triplicate 2 (CCNF)	27.359					
Triplicate 2 (ACTB)	18.226					
Triplicate 3 (CCNF)	27.913					
Triplicate 3 (ACTB)	18.203					

Samples were not included in analysis when two or more replicates failed.

The failure of qPCR with spleen-derived samples #7(WT) and #9(Het) may have been due to the degradation of RNA prior to cDNA synthesis. To assess cDNA quality and quantity, all cDNA samples were assessed using a QIAxpert spectrophotometer (table 4.15). This demonstrated that the purity of cDNA from #7(WT) and #9(Het) was low with A260/280 nm ratios of 1.3 and 1.39, respectively. Their absorbance curves were also flat compared to the other samples. Other cDNA samples provided A260/280 nm ratios greater than 1.71 (an A260/280 ratio of 1.8 is considered very high purity). Similarly, the cDNA concentrations from #7(WT) and #9(Het) were lower than their counterparts, at 88.4 ng/ $\mu$ L and 117.1 ng/ $\mu$ L, respectively.

TABLE 4.15: Mouse spleen cDNA quantity and quality.

cDNA Sample	Concentration (ng/ $\mu$ L)	A260/280
#4(WT)	900.4	1.76
#7(WT)	88.4	1.3
#15(WT)	781.1	1.71
#9(Het)	117.1	1.39
#14(Het)	686.1	1.72
#16(Het)	1,151.6	1.76
#3(Hom)	869.1	1.76
#8(Hom)	1,350.6	1.72
#17(Hom)	889.9	1.75



*"With every job when it's complete, there is a sense of bitter-sweet."*

- Mary Poppins

# 5

## Discussion

### Study recap

This thesis provided the first biomolecular and histopathological assessment of a mammalian model carrying an ALS-linked *CCNF* mutation in its genome. It aimed to investigate the impact of *CCNF*<sup>S621G</sup> on the expression of *CCNF* and cyclin F, assess histopathological features that are characteristic of ALS and ALS/FTD, and interrogate proteomic data for changes associated with neurodegeneration. *CCNF* expression levels were assessed by RT-qPCR of RNA collected from mouse spinal cord and spleen. Cyclin F expression was investigated by measuring and comparing cyclin F staining in neurons through IF on spinal cord tissues from WT and heterozygous and homozygous CRISPR-*CCNF*<sup>S621G</sup> mice, and by probing for cyclin F on Western blots of brain protein lysates from all the mice. Hallmark ALS and ALS/FTD histopathologies were investigated in mouse brain and spinal cord tissues stained in IF experiments, and the number of motor neurons in the lumbar spinal cord of each mouse were counted after tissues underwent Nissl staining. Changes in other proteins within the mouse proteomes were additionally explored by filtering and analysis of MS data from brain protein lysates from each mouse sample. As well, TDP-43 and ubiquitin proteins were specifically probed and quantified in Western blots of mouse brain protein lysates. The outcomes of this study design will be discussed in the following sections.

## 5.1 Evaluation of ALS/FTD histopathology in the CRISPR-CCNF<sup>S621G</sup> mouse model

### 5.1.1 Immunofluorescence staining

#### 5.1.1.1 Antibody optimisation

The optimisation of antibodies is important prior to IF staining on valuable tissue and cell samples. There are many benefits to optimising antibodies. These include: confirming the specificity of an antibody to the protein of interest; minimising the likelihood of wasting valuable samples (for example human and animal model tissues); reducing experimental costs as the lowest concentration that still gives a favourable level of staining and minimal non-specific background signal is identified. In this thesis, it was necessary to optimise a cyclin F antibody as cyclin F was the key protein of interest, and staining of cyclin F in human and mouse tissue had been problematic in previous IF experiments carried out by the Blair research group at Macquarie University.

A rabbit cyclin F (Santa Cruz) antibody was first optimised for the IF staining protocol, leading to successfully stained cells (figure 4.4). A second IF antibody optimisation experiment compared the effectiveness of low and high pH antigen retrieval buffers on two cyclin F primary antibodies — rabbit (Santa Cruz) and mouse (Santa Cruz). Tissues must undergo antigen retrieval prior to IF staining, to disrupt the cross-links (methylene bridges) between proteins which formed during formalin fixation, and unmask the antigenic sites (epitopes) on the proteins so IF antibodies can bind to them (Emoto et al., 2005; Shi et al., 1991). The efficiency of this disruption of cross-linking and unmasking of epitopes is dependent on the pH of the antigen retrieval buffer. Mechanistically, the application of heat to antigen retrieval breaks the methylene bridges between proteins and opens up the peptide chain, exposing its hydrophobic and hydrophilic regions (Emoto et al., 2005). Next, the tissue is left to cool in the antigen retrieval buffer and it is this step where the pH of the buffer is important. Upon cooling in neutral pH antigen retrieval buffer, epitopes are concealed due to the hydrophobic and ionic forces that cause the unfolded polypeptides to become entangled, whereas in both low and high pH buffers, regions along the polypeptide become strongly positive or negatively charged (depending on the specific protein) resulting in electrostatic repulsion. This repulsion prevents entanglement of the unfolded polypeptides, therefore leaving the epitopes uncovered.

Low pH antigen retrieval buffer was chosen as its use resulted in images with greater clarity (better unmasking of epitopes) and less overall background fluorescence irrespective of the primary antibody, compared to the high pH buffer. Both the rabbit and mouse cyclin F (Santa Cruz) antibodies gave bright cell staining, but the mouse antibody was elected the better option as its overall staining was more specific to cyclin F (it was

monoclonal and therefore only bound to a single epitope), and manufacture of the rabbit antibody was discontinued. Furthermore, multiple concentrations of the mouse cyclin F (Santa Cruz) antibody were tested (note 1:50 and 1:200 also tested previously (figure 4.4)), and a final concentration of 1:100 was chosen for further IF staining as it reduced the non-specific background signal and reduced antibody use (and costs), whilst still generating a suitable level of cell staining. The immunogen for generating the mouse cyclin F (Santa Cruz) antibody was a short peptide from the C-terminus of the human cyclin F protein. To confirm the specificity of the mouse cyclin F (Santa Cruz) antibody, blocking peptide experiments were performed in which mouse cyclin F blocking peptide (Santa Cruz) was used at 1:100 and 1:40 concentrations. The signal from mouse cyclin F (Santa Cruz) primary antibody was reduced when 1:100 concentration of blocking peptide was added to the primary antibody solution, suggesting that the primary antibody was specific to cyclin F. However, there was still some cell and background staining. To verify the reduction seen was caused by the blocking peptide binding to the primary antibody, and preventing its binding to the cyclin F epitope, the concentration of the blocking peptide was increased to 1:40 (as per the five-fold higher concentration recommended in the peptide neutralization protocol (Santa Cruz, accessed [http://datasheets.scbt.com/protocols/protocol\\_11.pdf](http://datasheets.scbt.com/protocols/protocol_11.pdf))). At the increased concentration of 1:40, the cyclin F signal was remarkably reduced, suggesting that the staining was not artefactual and the primary cyclin F (Santa Cruz) antibody had specific affinity for cyclin F protein in the mouse tissues.

It was noted that even when no primary antibody was applied to the tissues, there was still an excitation signal present when the 488 nm laser was used. Brain tissue vasculature (Pyon et al., 2019) and some neurons within the cortex and hippocampus generate fluorescence when excited with a 488 nm wavelength (Spitzer et al., 2011). As well, the fixation of tissue in paraformaldehyde or other aldehyde-based fixatives can lead to increased tissue auto-fluorescence when exposed to light at 488 nm (Robertson et al., 2008). These were the likely causes for the additional background signal in the blocking peptide experiments and when no primary antibody was used. Robertson et al. (2008) recommended sectioning tissue thinner than 4  $\mu\text{m}$  so that the volume of tissue contributing to auto-fluorescence is minimised. However, taking sections of that thickness on a manual microtome is technically challenging and prone to tearing the fragile tissue. In future studies, access to an automated microtome should be sought, so the tissue can be sectioned thinner. Also, to reduce auto-fluorescence in future studies, the sodium borohydride tissue preparation protocol by Clancy and Cauller (1998) can be trialled, whereby tissue is immersed in 0.1%  $\text{NaBH}_4$  causing the reduction of the fluorescence inducing “amine-aldehyde compounds, into non-fluorescent salts”.

### 5.1.1.2 Identification of known ALS/FTD cellular pathologies

A major goal of this thesis was to review and compare the expression and distribution of cyclin F within neurons in brain and spinal cord tissue from WT and heterozygous and homozygous CRISPR-*CCNF*<sup>S621G</sup> mice, and assess the presence of characteristic ALS/FTD-like histopathologies (mis-localised TDP-43, hyper-phosphorylated and aggregates of TDP-43, and ubiquitinated protein inclusions). No differences in the location of cyclin F were identified when brain and spinal cord tissues from WT mice were compared to heterozygous and homozygous CRISPR-*CCNF*<sup>S621G</sup> mice. Cyclin F was present in the nucleus and cytoplasm of cortical and hippocampal neurons and mostly in the cytoplasm of spinal cord neurons. When over-expressed in neuro-2a cells, cyclin F also remained nuclear (Lee et al., 2018). The location of cyclin F in zebrafish over-expressing *CCNF*<sup>S621G</sup> has not been reported. TDP-43 pathology including mis-localisation to the cytoplasm and aggregation is seen in up to 97% of ALS and 45% of FTD cases (Ling et al., 2013), regardless of the presence or absence of a *TARDBP* mutation. But, there are also some cases of ALS, for example mutant *FUS* and *SOD1* cases, that do not have TDP-43 positive aggregates (Renton et al., 2013). In mouse models of ALS, TDP-43 inclusions are not a prerequisite but are prevalent in models with *C9orf72* and *TARDBP* mutations (Stephenson and Amor, 2017). Whilst there are no specifically defined or required characteristics for ALS mouse models, good models should be informative for the underlying disease (De Giorgio et al., 2019), and have one, or ideally both, “face and construct validity” (Morrice et al., 2018). The notion of “face and construct validity” are, that a model recapitulates aspects of the human disease phenotype, and that the disease is induced in a way that is known to cause disease in patients. As the CRISPR-*CCNF*<sup>S621G</sup> mice were created to carry the mouse equivalent of a human disease-causing *CCNF*<sup>S621G</sup> mutation, they had construct validity, but at six-months-old TDP-43 remained in a ring-like formation in the nucleus of neurons in the cortex, hippocampus, and spinal cord, in all of the mice, and no aggregates were identified in brain or spinal cord tissue. Williams et al. (2016) reported that an American patient carrying the *CCNF*<sup>S621G</sup> mutation had TDP-43 pathology, so it is viable that TDP-43 inclusions are a final product of disease (Lutz, 2018). In this way, inclusions would not appear until the end stage of disease which could be why they were not present in the six-month-old CRISPR-*CCNF*<sup>S621G</sup> mice, and that this aspect of face validity of the model could be gained in an older model cohort. Alternatively, TDP-43 inclusions may not be a pathological feature in the CRISPR-*CCNF*<sup>S621G</sup> mice, and there may be other aspects of the model with face validity. No single model will ever mimic all aspects of the human condition. It is therefore appropriate for multiple models mimicking different aspects of disease biology to be generated and studied.

Hyper-phosphorylated TDP-43 deposits have been noted in the brain and spinal cord of ALS/FTD patients (Ling et al., 2013; Neumann et al., 2006; Prasad et al., 2019). Excessive phosphorylation increases cytoplasmic and mitochondrial localisation and aggregation of proteins such as TDP-43. To give an example, researchers have found that if TDP-43 is phosphorylated by truncated casein kinase 1d, it is triggered to mis-localise and accumulate into insoluble aggregates (Lee et al., 2017). In spite of this, based on the knowledge that there were no changes in normal TDP-43 localisation, it was not an unforeseen result that there was no phosphoTDP-43 in the brain or spinal cord tissue from the CRISPR-CCNF<sup>S621G</sup> mice. A number of small ubiquitin puncta were present mainly in cortical and spinal cord motor neurons in tissue from heterozygous and homozygous CRISPR-CCNF<sup>S621G</sup> mice. As these puncta were only present in the CRISPR-CCNF<sup>S621G</sup> mice, they could be representative of very early stage formation of pathological aggregates (He and Hays, 2004).

### 5.1.2 Nissl staining and spinal cord motor neuron counts

Various studies of ALS and ALS/FTD mouse models have shown significantly reduced motor neuron numbers as a measure of disease, but the experimental parameters and procedures used varied between studies. Whilst all of the studies localise counting to the ventral horn in lumbar spinal cord vertebrae 3 – 5, and only include neurons with distinct staining, the size of the motor neurons that were counted was based on either cell diameter (Reaume et al., 1996; Zhao et al., 2006, 2012), area (D’Errico et al., 2013), or approximate size and shape (i.e. large and polygonal (Devoy et al., 2017; Marden et al., 2007)). The lumbar spinal cord is ideal for measurements in mice, as here the motor neurons relay signals to limb muscles (Anderson et al., 2009), the muscles that are vital for movement and whose function deteriorate in ALS. In this study, the criteria for selecting motor neurons to be counted in the lumbar spinal cord included an area of  $\geq 80 \mu\text{m}^2$ , with clear Nissl staining, and located below the highest point of the central canal in the ventral horn. The batch processing code (see Appendix A.1.2.2) used on Fiji software to efficiently count motor neurons that fitted these criteria, allowed a unique grey-scale threshold value to be set for each sample (if necessary) to detect motor neurons visible by eye. This was needed because the auto-threshold was not always biologically relevant and missed obviously large target motor neurons in several images. The resulting counts and statistical analysis that compared the three mouse genotypes revealed a significant decrease in motor neuron numbers in the spinal cord of homozygous CRISPR-CCNF<sup>S621G</sup> mice compared to heterozygous CRISPR-CCNF<sup>S621G</sup> (adjusted P-value 0.0273) and WT (adjusted P-value 0.0187) mice (figure 4.21). D’Errico et al. (2013) pointed out that it is interesting and relevant to consider whether changes in motor neuron numbers collected in this way can be accepted as legitimate losses of motor neurons, as decreases in motor

neurons may not be caused by actual loss and/or death of motor neurons but rather atrophy of motor neurons which therefore renders them smaller than the set size criteria. The accuracy of the batch code and the threshold values for detecting true motor neurons can then be questioned, particularly as no other characteristic ALS/FTD histopathologies were observed in the CRISPR-*CCNF*<sup>S621G</sup> mice. In accepting the result of a significant reduction in spinal cord motor neuron numbers in homozygous CRISPR-*CCNF*<sup>S621G</sup> mice compared to WT and heterozygous cohorts, it could be possible that the level of motor neuron reduction may not be sufficient to cause a motor deficit. [Yang et al. \(2016\)](#) reported that at the onset of paralysis in their transgenic PFN1<sup>C71G</sup> ALS model mice, the number of lumbar spinal cord motor neurons was reduced by approximately 40%, which was greater than that seen in homozygous CRISPR-*CCNF*<sup>S621G</sup> mice.

#### 5.1.2.1 Disease severity comparison

Some of the CRISPR-*CCNF*<sup>S621G</sup> mice were bred to homozygosity in an effort to maximise the effect of any putative loss- or gain-of-function arising from the mutation. A potential dose dependent effect of the mutation or heterozygous advantage would lead to a worse phenotype in homozygous mice. In this scenario, heterozygotes may have increased relative fitness as the normal *CCNF* allele could be playing a role in alleviating the effects of disease ([Wexler et al., 1987](#)), whilst the homozygotes are more vulnerable to subtle cellular changes. This may explain why the number of lumbar spinal cord motor neurons in the homozygous CRISPR-*CCNF*<sup>S621G</sup> mouse cohort was significantly decreased in comparison to both the WT and heterozygous CRISPR-*CCNF*<sup>S621G</sup> cohorts. As the other experimental assessments of pathology in this study did not identify a change between the mouse genotypes, with all the results put together, it was evident that at six-months-old, the CRISPR-*CCNF*<sup>S621G</sup> mouse model did not accurately represent what was pathologically seen in tissues from the majority of ALS/FTD patients. So, the mechanisms of how *CCNF*<sup>S621G</sup> affects motor neurons in the mammalian system remain to be determined.

As previously discussed, there are a number of histopathologies that are commonly identified in ALS/FTD patients. However, the ways in which the disease will present itself in different animal models is highly variable, with each animal model likely to convey different aspects of disease, if any. An array of histological techniques including immunofluorescence and Nissl staining, that have been thoroughly optimised, similar to that performed in this study, have a strong capacity to identify similarities between models and patients (for example small ubiquitin puncta ([figure 4.16](#)) and decreased numbers of lumbar spinal cord motor neurons ([figure 4.21](#))), which can then be further investigated.

## 5.2 *CCNF* expression level changes

Gene mutations have the potential to alter gene expression, particularly if they alter sequence that encode residues that are subjected to post-translational protein modifications, directly impacting expression or protein activity. The missense mutation resulting from the base substitution of adenine to guanine in *CCNF* (c.1861A>G) leads to substitution of an incorrect amino acid, glycine, instead of serine (p.S621G), in cyclin F protein. Serine residues contain a hydroxyl group which can act as a nucleophile and as such, undergo phosphorylation and o-glycosylation ([Strachan and Read, 2011](#)), whereas glycine groups do not have such groups. [Lee et al. \(2017\)](#) confirmed that S621 is indeed phosphorylated and the S621G substitution destroys that phosphorylation site, which was previously shown to regulate the Lys48-specific E3 ligase activity of the SCF complex. As a result, the lack of phosphorylation led to over-active cyclin F-mediated ubiquitylation and therefore hyper-ubiquitylation of proteins, a hallmark pathology of ALS. To further understand the influence of *CCNF*<sup>S621G</sup> on *CCNF* gene and cyclin F protein expression levels, several methods were applied: RT-qPCR was performed using spleen-derived RNA from each mouse; IF staining of cyclin F in spinal cord tissues; and Western blot of brain protein lysates that were probed for cyclin F. The data from these experiments were then compared to that from the WT cohort. In addition, changes in TDP-43 and ubiquitin levels were examined by Western blot and changes in other proteins were examined by analysing MS data.

### 5.2.1 The *CCNF*<sup>S621G</sup> mutation did not lead to loss of *CCNF* gene expression in CRISPR-*CCNF*<sup>S621G</sup> mouse model

#### 5.2.1.1 RT-qPCR

From the preliminary qPCR in which triplicates of spinal cord cDNA from #15(WT), #16(Het), and #17(Hom) were amplified, *CCNF* fold expression, an indication of transcription level, was reduced in the heterozygote (#16) compared to the WT(#15) mouse and increased in the homozygous(#17) mouse (table 4.13). One possible explanation for the contradictory *CCNF* expression trend, is that in the heterozygous mouse, mutant cyclin F could have had a dominant negative effect that led to down-regulation of gene expression. In comparison, the homozygous mouse which expressed only mutant *CCNF* transcripts, may have escaped self-regulation. The *TARDBP* gene has been found to self-regulate ([Ayala et al., 2011](#); [De Giorgio et al., 2019](#)), for example *TARDBP* mRNA levels were significantly up-regulated in a dose-dependent manner in spinal cord from mice heterozygous and homozygous for a C-terminal domain mutation in a study conducted by [Fratta et al. \(2018\)](#). The preliminary qPCR performed here was only completed on one sample from each cohort due to limited sample availability, and additional samples

should now be analysed to confirm and investigate the differential expression.

As the preliminary spinal cord qPCR study was performed with one mouse for each genotype, further samples were required for more definitive conclusions on *CCNF* gene expression. However, no further brain or spinal cord tissues were available, so RNA was instead extracted from all the mouse spleens. cDNA was generated from this spleen RNA, and when it was run through qPCR, Ct values for one of the WT(#7) and heterozygous(#9) samples could not be determined (table 4.14). These two samples also had very high *ACTB* Ct values and poor QIAxpert readings, suggesting their poor quality. This could be due to RNA degradation prior to cDNA synthesis, a condition which meant the oligo(dT) used in cDNA synthesis was unable to successfully amplify the RNA as it was dependent on annealing to a stable poly(A) tail on the RNA [Vermeulen et al. \(2011\)](#). The Ct mean values obtained for the remaining two samples in the WT and heterozygous cohorts that were used in analysis, were quite different from each other (figure 4.34.a), which could be why the calculated average fold expression of *CCNF* in the WT cohort was greater than 1.0. When comparing fold-change in expression and average fold-change expression values from disease samples to a control or WT, values >1.0 mean the gene is up-regulated in comparison to WT and values <1.0 mean the gene is down-regulated. The average fold expression of *CCNF* in the spleen of the heterozygous cohort was 0.916 and in the homozygous cohort was 0.995, indicating that expression of *CCNF* was slightly decreased, but no statistically significant difference in *CCNF* fold expression was found between the three mouse genotypes. This revealed that the transcription of *CCNF* was not significantly impacted by the S621G mutation. However, it was still possible that the activity of cyclin F protein, such as UPS-mediated protein degradation, could be decreased due to the substitution of the S621G residue.

## 5.2.2 The *CCNF*<sup>S621G</sup> mutation did not lead to loss of cyclin F protein expression in the *CCNF*<sup>S621G</sup> mouse model

### 5.2.2.1 Western blot

The expression levels of cyclin F in protein lysates collected from WT and CRISPR-*CCNF*<sup>S621G</sup> mouse brains and spleens, could not be confirmed or quantified by Western blot, despite attempts with the three different antibodies (mouse Santa Cruz, rabbit Santa Cruz, and rabbit ThermoFisher) at various concentrations. This was particularly unexpected for the spleen lysate given that cyclin F was reported to be expressed at higher levels in the spleen. The endogenous level of cyclin F expression may be insufficient to be detected by Western blot as there is a lack of sensitivity of the Western blot technique to proteins expressed at low levels. However, a band at 140 kDa was detected in brain protein lysates when the rabbit cyclin F antibody (Santa Cruz) was applied to the blot at

a concentration of 1:500. It remains to be determined whether the band at 140 kDa from the mouse brain lysate represents an isoform of cyclin F. To obtain a more conclusive answer, future studies can repeat the Western blot with rabbit cyclin F (1:500, Santa Cruz) with increased protein lysate loaded into the SDS-PAGE to see if the band was still present and clearer, and then using a second blot, apply a blocking peptide to rabbit cyclin F to see if the band is lost. The disappearance of the band would support the specificity of the rabbit cyclin F antibody to cyclin F and that the band at 140 kDa was cyclin F. In addition, if sufficient protein can be extracted from the gel band, it may be suitable for MS to confirm identity of the protein. Furthermore, it would confirm the observations of [Bai et al. \(1994\)](#), that most cyclins have a larger molecular weight in SDS-PAGE than their predicted weight. Alternatively, the cyclin F band could be sitting higher on the blot because the cyclin F protein may be bound to another protein or functional group. To investigate this, SDS-PAGE with greater denaturing properties could be run or again, the region in the gel could be cut out and the proteins identified by MS.

As cyclin F could be detected by IF staining, this technique was evidently more sensitive to less abundant proteins. Other attempts to validate the specificity of the antibodies to cyclin F, included probing for cyclin F in Western blots of protein lysate from the human and mouse cell lines, HEK293 and neuro-2a respectively. From these, a band around 100–110 kDa was seen in the neuro-2a lysate when rabbit cyclin F (1:500, Santa Cruz) was used. This was akin to information provided by the supplier (antibody data sheet), but different to what was seen with the mouse brain lysates and HEK293 lysate, which stained at 140 kDa with the same antibody. Other researchers have more accurately and successfully detected recombinant cyclin F with Western blot by tagging it with mCherry ([Hogan et al., 2017](#); [Lee et al., 2018](#); [Williams et al., 2016](#)), and [Hogan et al. \(2017\)](#) also detected cyclin F at around 100 kDa when the rabbit cyclin F Santa Cruz antibody was used on zebrafish protein lysates.

### **Western blot troubleshooting:**

Several technical challenges were encountered during the Western blot experiments conducted for this thesis. Incomplete transfer of proteins from electrophoresis gel to membrane was evident, with proteins left in the gel after wet transfer. The transfer time was increased in subsequent experiments to ensure that the lack of a clear cyclin F band in the expected size range was not due to poor protein transfer. Blots were also imaged wet and dry in an attempt to boost signal from IR dye-conjugated protein. Imaging blots dry gave the strongest protein band signals compared to those imaged wet.

### 5.2.2.2 Immunofluorescence staining

Quantifying the IF staining of cyclin F in cells from spinal cord tissue from WT and CRISPR-*CCNF*<sup>S612G</sup> mice was an alternative means of assessing cyclin F expression. The levels of cyclin F staining were not significantly different between the three genotypes. This was similar to that seen in zebrafish by [Hogan et al. \(2017\)](#), and aligned with the outcome from RT-qPCR where no significant difference in gene expression was observed. As there was both no change in *CCNF* gene expression and no change in cyclin F protein expression within the CRISPR-*CCNF*<sup>S621G</sup> mice, it was concluded that the S621G mutation did not impact gene transcription or translation in the mice at six-months-old.

As there was potential subjectivity by the observer in picking cells to measure cyclin F staining, a future alternative approach would be to remove observer bias by blinding them to the genotype of the samples, for both imaging and quantification of staining. Standardisation was provided through the use of the same microscope settings and batch code ([A.1.2.1](#)) for quantification. To further increase confidence in the data, a second observer should perform the same analysis to see if a similar conclusion is reached.

## 5.2.3 Other protein changes

### 5.2.3.1 Western blot

Western blot was also used to study the expression of the ALS-linked proteins, TDP-43 and ubiquitin. When ALS patients have been compared to healthy controls, expression of TDP-43 was found to be elevated ([Feneberg et al., 2018](#)). When the WT and CRISPR-*CCNF*<sup>S621G</sup> mouse brain protein lysates were assessed by Western blot, the levels of TDP-43 in each cohort showed no significant difference (figure [4.29](#)). As well, the level of ubiquitin did not differ between the cohorts (figure [4.30](#)). This was consistent with the lack of protein changes identified in tissues when IF staining was performed, and with a previous study ([Hogan et al., 2017](#)), where no significant difference in TDP-43 expression was observed in *CCNF*<sup>S621G</sup> zebrafish.

### 5.2.3.2 Mass spectrometry

Mass spectrometry was performed on mouse brain protein lysates to obtain information about overall protein changes (proteins expressed and expression levels) between the three mouse genotypes. As the tissue used in this study was from young adult mice (six-months-old) ([Flurkey et al., 2007](#); [Hagan, 2017](#)), it was anticipated that any proteomic changes that were relevant to ALS/FTD pathways may be early markers of disease. When looking at the total number of proteins and those that overlapped between genotypes (figure [4.25](#)), the heterozygous and homozygous cohorts had more proteins in common than with the WT, suggesting that the *CCNF*<sup>S621G</sup> mutation triggered common

mechanisms in heterozygous and homozygous mice. From the initial volcano plots that compared the overall protein expression profiles of each genotype, it was found that both the heterozygous and homozygous CRISPR-*CCNF*<sup>S621G</sup> protein lysate profiles had more proteins with significantly increased expression than decreased expression, when compared to WT (figure 4.24). When the highly stringent “over-expression” and “under-expression” filtering and sorting criteria were applied to the large data set, this reversed. There were more proteins identified with decreased expression (564 proteins) in the heterozygous and homozygous CRISPR-*CCNF*<sup>S621G</sup> protein profiles than increased expression (90 proteins). The rationale behind the “under-expression” filter was that if the effect of mutant cyclin F was to decrease protein expression in heterozygous mice, then a further decrease would be evident in homozygous mice. In applying the “over-expression” filter, it was accepted that proteins with very small increases in expression i.e. between 1.0 and 2.0, were lost and it is plausible that these proteins could also be of value to disease initiation. However, to make the data manageable, it was necessary to make the cut off value 2.0.

### **PANTHER, GO, and STRING**

PANTHER is an online bioinformatics tool that was used in this study to classify proteins that were identified by MS data and subsequent filtering, by molecular function. Those categories with the greatest number of differentially expressed proteins are more likely to implicate the molecular pathways that were substantially impacted by mutant cyclin F. Reducing the final 90 proteins from the “over-expression” filter through the PANTHER categories with the most proteins, resulted in two final categories. These categories, “cell adhesion molecule binding” and “enzyme binding”, each had two proteins within them, *AFDN* and *ARVCF*, and *GAPVD1* and *CDC42*, respectively (table 4.7). Proteins in the “cell adhesion molecule binding” category are defined as those that interact selectively and non-covalently with cell adhesion molecules (CAM). *AFDN* encodes the afadin protein that assists in cell-to-cell binding and junction formation, particularly during embryogenesis. *AFDN* is pathologically associated with acute leukaemias (Ikeda et al., 1999), and binds to the CAM, nectin (Ogita et al., 2010). *ARVCF* encodes a protein from the catenin family, Armadillo Repeat gene deleted in Velo-Cardio-Facial syndrome (ARVCF), which is involved in protein-to-protein interactions, communication of the external environment to cells, and cell development, and complexes with the CAM, cadherin (Fang et al., 2004). An autosomal dominant mutation in the gene causes Velo-Cardio-Facial syndrome. Proteins in the “enzyme binding” category are defined as those that interact selectively and non-covalently with any enzyme. The *GAPVD1* gene encodes the protein, GTPase activating protein (GAP) and VPS9 domains 1, which acts as a GTPase, GAP, and a guanine nucleotide exchange factor (GEF), being involved

with endocytosis (essential for activating Rab5 during engulfment of apoptotic cells ([Kitano et al., 2008](#))) and insulin receptor internalisation. Mutations in *GAPVD1* cause the Familial Idiopathic Steroid-Resistant Nephrotic Syndrome With Focal Segmental Hyalinosis disease. *CDC42* encodes cell division control protein 42, which is a Rho GTPase and acts like a switch or regulator for various molecular processes such as cytoskeleton remodelling, cell signalling polarity, adhesion membrane trafficking, and cell migration ([Govek et al., 2005](#); [Saraceno et al., 2018](#)). In FTD and Alzheimer's disease, it has been hypothesised that increased cortical levels of *CDC42* are related to synaptic compensation processes caused by a loss of neuronal function ([Saraceno et al., 2018](#)). The increased expression of *GAPVD1* in the CRISPR-*CCNF*<sup>S621G</sup> mice could indicate increased endocytosis, while increased *CDC42* could suggest a similar synaptic compensation effect, both potentially early markers for disease.

GO is the world's largest resource of gene and protein function data ([Ashburner et al., 2000](#); [The Gene Ontology Consortium, 2018](#)). GO was used in this study to uncover the biological processes associated with the proteins that were differentially expressed ("over-expression" and "under-expression" filtering) in the CRISPR-*CCNF*<sup>S621G</sup> mice. GO analysis of the 90 proteins that met the "over-expression" filter identified six biological process categories ("complete localisation within membrane", "membrane organisation", "positive regulation of transport", "cellular protein localisation", "cellular component assembly", and "organelle organisation") (table 4.8). "Positive regulation of transport" may reflect the increase in aberrant transport that is associated with mis-localisation of proteins seen in ALS/FTD ([Mancuso and Navarro, 2015](#); [Picher-Martel et al., 2016](#)), however this was not evident for the proteins that were assayed here in the CRISPR-*CCNF*<sup>S621G</sup> mice. Aberrant changes in "membrane and organelle organisation", and "cell component assembly" may be associated with degeneration. As proteins such as TDP-43 are known to mis-localise, aberrant changes in biological processes associated with "complete localisation within membrane" and "cellular protein localisation" may also reflect these disease features. Further proteomic studies are required, perhaps using known disease-affected brain regions, to gain meaningful outcomes and determine the relationship of mutant cyclin F to these biological changes.

PANTHER analysis of the 564 "under-expressed" proteins separated them into eight molecular function categories (figure 4.27). The largest molecular function category of "catalytic activity" was also the largest category of proteins reported from MS studies of neuro-2a cells 24 h post transfection with *CCNF*<sup>S621G</sup> ([Hogan et al., 2017](#)). Since cyclin F has known catalytic activity as an E3 ubiquitin ligase when it is part of the SCF complex ([D'angiolella et al., 2013](#)), aberrant "catalytic activity" may represent the impact of the S621G mutation on cyclin F-related function. When "catalytic activity" was investigated at the next level, "hydrolase activity" with 95 proteins, was the largest category —again, also reported by [Hogan et al. \(2017\)](#). Narrowing the number of molecular function

categories to a protein level, by selecting the category at each level with the largest number of proteins, gave the final PANTHER category “GTPase activity”, including *GNAI2*, *TBC1D15*, and the *RAB* genes. *GNAI2* is a G-protein subunit involved in signal transduction and was found to be down-regulated in the spinal cord of ALS/FTD patients (Iridoy et al., 2018); *TBC1D15* is a mitochondrial rab GTPase activating protein with a role in autophagosome biogenesis and possibly linked to Parkinson’s disease (Yamano et al., 2014; Zhang et al., 2005); and *RAB* genes encode 60 rab proteins that regulate intra-cellular membrane trafficking and vesicle formation. Defects in these rab-related biological processes are associated with neurodegeneration and the specific role these proteins play in ALS/FTD is actively being studied (Kiral et al., 2018; Parakh et al., 2018). The decreased expression of rab proteins could be an early sign of abnormal cellular trafficking and it would be valuable to monitor levels of rab proteins in future studies. Indeed, one such dysregulated protein was evident in the list, *TBC1D15*, which acts as an activator of rab proteins, particularly rab-7a which is involved in endocytosis. As *CCNF* is involved in regulating the proteasome and autophagy pathways of protein degradation and clearance (Ito et al., 2017), it was anticipated that other proteins in these protein quality control pathways may be differentially regulated. GO analysis of the 564 “under-expressed” proteins in the CRISPR-*CCNF*<sup>S621G</sup> mice identified 29 biological processes relevant to ALS/FTD (table 4.10). At least three of these processes (“positive regulation of autophagosome assembly”, “regulation of vesicle-mediated transport”, and “COPII vesicle coating”) are implicated in protein clearance pathways and are processes mediated by rab proteins (Parakh et al., 2018; Soo et al., 2015).

STRING analysis (figure 4.28) of the 26 “under-expressed” proteins from the final PANTHER level, “GTPase activity” (figure 4.27 and table 4.9), revealed four strongly associated Reactome pathways that could conceivably be related to early disease-related changes in the CRISPR-*CCNF*<sup>S621G</sup> mice. As *GNAI2* is a modulator of cell signalling, its decreased expression supports “decreased activity of the signal transduction” (HSA-162582) and “signal amplification” (HSA-392518) Reactome pathways. Intra- and inter-cellular signalling defects could represent early changes related to neurodegeneration and loss of cellular function. The decreased Reactome pathways of “rab regulation of trafficking” (HSA-9007101) and “membrane trafficking” (HSA-199991) also plausibly fit with the loss of cellular function in ALS through loss of interaction with effector proteins, and aligns with the decreased expression of *TBC1D15* and the 6 rab-related proteins implicated by PANTHER analysis.

Lastly, the proteomic data was compared with the proteins implicated by three previously published mutant cyclin F studies (Hogan et al. (2017); Lee et al. (2018); Williams et al. (2016)), as indicated in table 5.1. Microtubule associated protein 1 light chain 3 $\alpha$  encoded by *LC3* is necessary for the maturation of autophagosomes whose role is to degrade cellular wastes (Lee and Lee, 2016). The protein’s expression was decreased in

neuro-2a cells that expressed mutant *CCNF*, which implicates decreased autophagy function. In contrast, the protein's expression was increased in the CRISPR-*CCNF*<sup>S621G</sup> mice, and further studies would be required to assess whether the aberrant increase is associated with aberrant autophagy. As the major role of the chaperonin containing TCP1 subunit 8 protein encoded by *CCT8* is to assemble and transport newly synthesised proteins (Kim et al., 2017), its decreased expression may be relevant to the protein misfolding and mis-localisation that is prominent in ALS (Kim et al., 2017). As *CCT8* expression was decreased in both heterozygous and homozygous CRISPR-*CCNF*<sup>S621G</sup> mice, lower levels of the protein may indicate early changes in proteostasis. Reelin protein encoded by *RELN* is involved in brain development including positioning neurons, neuronal growth, maturation and synaptic plasticity (D'Arcangelo, 2014). It has not been previously associated with ALS or FTD, but was found to be increased by 40% in the cortex of patients with Alzheimer's disease when compared to controls (Botella-López et al., 2006). The aberrant increase of reelin in the CRISPR-*CCNF*<sup>S621G</sup> mice, warrants its assessment in further studies.

In this study, molecular and proteomic techniques of RT-qPCR, Western blot, and mass spectrometry reported no change in *CCNF* or cyclin F protein expression. Whilst Western blot proved challenging to optimise for the identification of the mutant cyclin F protein, it was valuable for the identification of more commonly studied proteins such as TDP-43. Mass spectrometry and successive *in silico* analyses rendered a huge output of information, including several proteins, pathways, and molecular functions that could be examined in the future. The combination of these mass spectrometry results with optimised Western blot and RT-qPCR, forms a powerful analytical pipeline whose results could paint a grander picture of what is altered as a result of *CCNF*<sup>S621G</sup>.



TABLE 5.1: Previously reported mutant *CCNF* associated proteins.

Paper	Gene symbol	Protein	Expression outcome in paper	Abundance ratio: (Het/WT)	Abundance ratio: (Hom/WT)	Discussion	
Lee et al. (2018)	<i>P62/SQSTM1</i>	Sequestosome 1	↑ (P = 0.0486) in neuro-2a cells expressing <i>CCNF</i> <sup>S621G</sup>	Not detected		Sequestosome 1 is a marker of autophagy activity and can become up-regulated when UPS function is impaired (Liu et al., 2016). The significantly increased expression in mutant <i>CCNF</i> neuro-2a cells could mean UPS function was disrupted in these cells but as it is was not detected in the CRISPR- <i>CCNF</i> <sup>S621G</sup> mice.	
	<i>LC3/MAP1LC3A</i>	Microtubule Associated Protein 1 Light Chain 3 α	↓ in neuro-2a cells expressing <i>CCNF</i> <sup>S621G</sup>	1.099	1.609	<i>LC3</i> expressed in opposite direction to that seen in neuro-2a cells. “Over-expression” filter would have removed as abundance ratios were <2.00.	
	<i>LAMP2A</i>	Lysosome-associated membrane glycoprotein 2	↑ (P = 0.0318) in neuro-2a cells expressing <i>CCNF</i> <sup>S621G</sup>	Not detected		The increased expression in neuro-2a cells suggests increased function of the autophagy pathway. As the protein was not detected in CRISPR- <i>CCNF</i> <sup>S621G</sup> mice, activation of the production of lysosomes was not increased and it was likely the UPS was still functioning as the major pathway for protein degradation (Alfaro et al., 2019).	
	<i>ATG7</i>	Ubiquitin-like modifier-activating enzyme ATG7	Present in Lys48 immunoprecipitate from neuro-2a cells expressing <i>CCNF</i> <sup>S621G</sup>	0.564	0.588	Decreased expression but not reduced further in homozygotes so it would have been removed in excel filtering as it was less likely to be biologically relevant. It could be worthwhile investigating these three proteins in an aged CRISPR- <i>CCNF</i> <sup>S621G</sup> mouse cohort to confirm their decreased expression, as levels of MAPT are increased in Alzheimer’s disease, Parkinsons and FTD (Rademakers et al., 2004), <i>HSP90</i> protein folding (Lackie et al., 2017)	
	<i>HSP90</i>	Heat shock protein 90		0.857	0.925		
	<i>MAPT</i>	Microtubule-associated protein tau		0.950	0.955		
	<i>CTLA4</i>	Cytotoxic T-Lymphocyte Associated Protein 4		Not detected			Protein acts as an immune-checkpoint by inhibiting activation of T-cells (Tai et al., 2012). Its presence in Lys48 immunoprecipitate is unclear as decreased protein expression would be suggestive of the presence of neuroinflammation in the neuro-2a cell, similar to that identified in FTD patients (Santos et al., 2014).
	<i>RELN</i>	Reelin		2.33	4.798		Expression increased in both heterozygotes and homozygotes with an even greater increase measured in homozygotes. So biologically, two mutant <i>CCNF</i> alleles were having a more pronounced impact on <i>RELN</i> whether it be through increasing gene expression or preventing protein degradation.

Table 5.1 continued

	<i>CCT8</i>	Chaperonin Containing TCP1 Subunit 8		0.859	0.70	Subunit of a chaperonin protein complex involved in assembly and transport of newly synthesised proteins (Kim et al., 2017). As there was a greater decrease in expression in the homozygous CRISPR mice, this was likely a biologically relevant change.
	<i>LRP5</i>	Low-Density Lipoprotein Receptor-Related Protein 5		Not detected		Functionally involved in signal transduction and bone formation (Gong et al., 2001). Its impact has not been assessed in ALS or neurodegeneration, and it is unclear how <i>CCNF</i> changes would affect its expression.
	<i>SHC1</i>	SHC-transforming protein 1		Not detected		An adapter protein that couples activated growth factor receptors to signal transduction pathways (Yulug et al., 1995).
Hogan et al. (2017)	<i>CASP3</i>	Caspase 3	↑ in neuro-2a cells expressing <i>CCNF</i> <sup>S621G</sup> 24 h post-transfection	1.342	2.628	Expression increased like it was in the neuro-2a cell. As the abundance ratio: (Het/WT) was not > 2.00, it will get removed in excel filtering.
	<i>RRM2</i>	Ribonucleoside-diphosphate reductase subunit M2	No expression change in neuro-2a cells expressing <i>CCNF</i> <sup>S621G</sup>	Not detected		Catalyses formation of precursors for DNA synthesis (Pavloff et al., 1992). No expression change aligns with no detection.
	CP110	Centriolar coiled-coil protein of 110 kDa		Not detected		Associates with cyclin F on centrioles in G2 of the cell cycle to ensure successful centrosome duplication (Chen et al., 2002). Likely that it was not expressed in the brain of the CRISPR mice as most cells in the brain are not actively undergoing mitosis.
	<i>NUSAP</i>	Nucleolar And Spindle Associated Protein		Not detected		Protein is a cell cycle regulated microtubule binding protein and a substrate of cyclin F (Emanuele et al., 2011). Its expression must not be affected by the <i>CCNF</i> <sup>S621G</sup> mutation as change was not detected in neuro-2a cells and it was not detected in the CRISPR mice.
	<i>CDC6</i>	Cell Division Cycle 6		Not detected		Regulates DNA synthesis and replication through its roles in initiation and acting as a checkpoint control ensuring the completion of DNA replication before mitosis begins (Borlado and Méndez, 2007), but as neurons are post-mitotic, protein expression was likely absent or too low for detection.
	<i>SLBP</i>	Histone RNA hairpin-binding protein		Not detected		Cyclin F assists in degrading histone RNA hairpin-binding protein in G2 of cell cycle, but as neurons are post-mitotic, protein expression was likely absent or too low for detection (Dankert et al., 2016).
Williams et al. (2016)	<i>RRM2</i>	Ribonucleoside-diphosphate reductase subunit M2	↑ RRM2 in neuro-2a (P = 0.020) and NSC-34 (P = 0.023) cells expressing <i>CCNF</i> <sup>S621G</sup>	Not detected		See function above. It is unclear why or how there would be increased expression as a result of the <i>CCNF</i> S621G mutation.

Abundance ratios come from the MS data output on WT and heterozygous and homozygous CRISPR-*CCNF*<sup>S621G</sup> mouse brain protein lysates.

## 5.3 Future directions - further analysis of the CRISPR-*CCNF*<sup>S621G</sup> mouse model

This section explores future strategies with which to analyse the CRISPR-*CCNF*<sup>S621G</sup> mouse model to further assess ALS/FTD-like features and its utility as a pre-clinical model.

### 5.3.1 Refinements

Various refinements to assays performed during this project may give better insight into pathological features. To follow on from the Western blot analyses performed during this project, SDS-PAGE could be further optimised including using greater quantity of brain protein lysate under more stringent denaturing conditions to confirm if a cyclin F band remains at 140 kDa or shifts to a predicted lower molecular weight. In addition, the top candidate protein hits from MS analysis (for example *TBC1D15*, *GNAI2* and *RELN*) can be analysed by Western blot to validate their expression. Also, additional tissue (especially brain and spinal cord) should be collected from other 6-month-old WT and CRISPR-*CCNF*<sup>S621G</sup> mice as they become available, to enable further RT-qPCR to validate the gene expression data obtained in this study. The proteomic analysis of the CRISPR-*CCNF*<sup>S621G</sup> mouse model by MS could be extended by performing two-dimensional gel electrophoresis followed by MALDI-TOF/TOF (Matrix Assisted Laser Desorption Ionisation – with tandem Time Of Flight). The two-dimensional gel electrophoresis would separate (based on isoelectric point and mass) and detect specific proteins of interest from others in the protein lysate (Brettschneider et al., 2010). These proteins of interest would be cut out of the gel, prepared, and then run through MALDI-TOF/TOF where they would be ionised and separated by their mass-to-charge ratio. Specific ions would then be selected for further analysis. The two techniques combined would provide information on *in situ* modifications of the specific proteins of interest (i.e. peptide information to the level where the entire sequence can be identified) and potentially uncover early disease new biomarkers (Ekegren et al., 2008).

To date, the effects of mutant cyclin F have not been characterised in ALS/FTD patient tissue. Ideally, the histopathologies of *CCNF*<sup>S621G</sup> patient tissues could be compared to that of the mouse model to identify shared features. IF staining with a cyclin F antibody could be performed similar to section 3.3.1.1 and the trends of cyclin F levels in CRISPR-*CCNF*<sup>S621G</sup> mouse tissue could be compared to that in mutant *CCNF* patient tissue. Comparison of mouse and patient data would further test the utility of the model, including validation of the mouse functional proteomic outputs, if the same differentially expressed proteins are identified. Another IF staining experiment that could be performed

on six-month-old CRISPR-*CCNF*<sup>S621G</sup> mouse tissue is dual staining of tissue with ubiquitin and cyclin F to see if they co-localise. An alternative mouse TDP-43 antibody could also be used in dual staining with ubiquitin to better assess the presence of any mis-folded TDP-43.

Morphological changes including changes in the size of the hippocampus and cortical width, can be measured to assess disease progression through hippocampal degeneration and cortical atrophy (Ke et al., 2015; Liu et al., 2016; White et al., 2018). For example, Ke et al. (2015) used immunohistochemistry (IHC) to stain sagittal brain sections from transgenic mice expressing the A315T *TARDBP* mutation (iTDP-43<sup>A315T</sup> mice), and compared the sizes of hippocampi and cortical widths at different time points. They found that both the size of the hippocampus and width of the cortex decreased over time which demonstrated age-related degeneration. They also carried-out IF staining with cortical layer markers, to find that the number of neurons in cortical layer V decreased with age and disease progression in the mice. To further analyse the brain, remaining brain tissue slides from this study could be stained with cresyl violet or TDP-43 by IHC, and the sizes of the hippocampi could be compared between the WT and heterozygous and homozygous CRISPR-*CCNF*<sup>S621G</sup> mice. As well, IF staining with neocortical laminar markers that explicitly target laminae II/III and V (for example Ctip2 or POU3F2) could be performed to measure neocortical width and the number of neurons in the cortical laminae. This would have the potential to provide early evidence for layer V changes which have been observed before in disease (Ke et al., 2015), and the specific presence and location of any degeneration in the brains of the CRISPR-*CCNF*<sup>S621G</sup> mice.

To further assess cyclin F expression data, and compare with that from IF staining (no difference in expression between the three mouse genotypes), repeat measurements could be taken on spinal cord tissues stained with cyclin F by IHC. Although IHC is more commonly used for localisation studies, it can be used to semi-quantitatively measure protein expression (Bauman et al., 2016). IHC could also be performed with a ubiquitin antibody to additionally clarify that there are no skein-like or lewy-body like inclusions present in tissue.

It was expected that cyclin F expression would be visualised and quantified by Western blot. As this did not work, another technique that could be employed in future studies to measure cyclin F expression, is ELISA (enzyme-linked immunosorbent assay). In this experiment, cyclin F antigens from the mouse brain protein lysates would adsorb to the base of wells in an optical reaction plate that have been coated with cyclin F antibody. Following this, the addition of a cyclin F-specific enzyme-linked secondary antibody and a fluorescence-generating substrate would enable quantitative detection of cyclin F (Schweitzer and Kingsmore, 2002). In the past, Fang et al. (2010) collected skin and spinal cord protein lysate from transgenic SOD1<sup>G93A</sup> mice, and successfully measured matrix metalloproteinases MMP-2 and MMP-9, oxidative damage marker 3-NT, and the

cytokines TNF- $\alpha$  and IL-1 $\beta$ , by ELISA. So, this technique should be applicable for measuring other proteins in lysates collected from other mouse models. Prior to a quantitative assay like ELISA, cyclin F can be concentrated using protein chromatography based on ligand affinity to cyclin F. One such specific technique is immunoprecipitation. During immunoprecipitation of cyclin F from protein lysates, cyclin F antigens in the sample bind to an anti-cyclin F antibody and the antibody-antigen complex can be immobilised when incubated with agarose or magnetic beads coated in a secondary antibody, the beads collected, and cyclin F dissociated from the beads (Corthell, 2014). In this way, cyclin F will be purified from the mix of proteins.

In this study, Nissl staining was used to label the lumbar spinal cord motor neurons for motor neuron counting and investigate spinal cord degeneration. It is possible that the size of motor neurons decreased in disease state and therefore influenced total motor neuron numbers in the automated counts performed. To confirm the validity of the motor neuron count data, a second tissue staining technique using a choline acetyltransferase (ChAT) antibody could be performed in future studies. ChAT antibodies are considered definitive and reliable markers for cholinergic neurons —functioning neurons that use the ChAT enzyme to synthesise the neurotransmitter, acetylcholine (Barber et al., 1984; Storm-Mathisen, 1977), and can therefore be used to quantify numbers of normally functioning neurons. ChAT staining can also be used to assess neuron morphology. ChAT labelling of motor neurons in mutant *SOD1*<sup>G86R</sup> transgenic mice has shown significant reductions in motor neuron numbers in comparison to WT (Morrison et al., 1996), verifying the technique’s utility in assessing ALS mouse models. Furthermore, Ebstein et al. (2019) counted ChAT labelled motor neurons in the lumbar spinal cord of knock-in TDP-43 mutant mice at 1, 1.5 and 2 years of age, and a similar time progression analysis could be performed on multiple CRISPR-*CCNF*<sup>S621G</sup> cohorts.

### 5.3.2 Compare data from six-month-old cohorts to an aged cohort

ALS and FTD are late onset diseases, with symptoms beginning at an average age of 55 - 65 years, and disease progressing at various rates (months to years) (Chio et al., 2009; McCann et al., 2017; Picher-Martel et al., 2016). An “old” or aged mouse is generally considered to be 18 - 24 months old (table 5.2), as their lifespan is around 2 - 3 years, with survivorship rapidly decreasing after 24 months-of-age (Flurkey et al., 2007; Hagan, 2017). As the six-month-old CRISPR-*CCNF*<sup>S621G</sup> mouse cohorts analysed in this thesis were young adults with relatively naive motor neurons, it is possible that they were too young for significant neurodegeneration, and explain why only one pathological assessment showed a significant result (figure 4.21: nissl staining showed a significantly decreased number of lumbar spinal cord motor neurons). The CRISPR-*CCNF*<sup>S621G</sup> mouse

model did not show other features of early disease onset, and more time may be needed for neurodegeneration to manifest in these mice (Renton et al., 2013; van Blitterswijk et al., 2012).

TABLE 5.2: Life stage equivalents in mice and humans.

Life stage	Mouse age	Human age
Adult	3 - 6 months	20 - 30 years
Middle-aged	10 - 14 months	38 - 47 years
Old	18 - 24 months	56 - 69 years

Data from Flurkey et al. (2007) and Hagan (2017).

Most ALS mouse models to date were generated by over-expressing ALS genes which often leads to acute phenotypes. It is possible that when expressed at physiological levels, the  $CCNF^{S621G}$  mutation will only lead to significant pathological changes at a later age in these mice. It would therefore be important to assess the CRISPR- $CCNF^{S621G}$  mouse model at an older age, and that experiments for example hippocampal degeneration and cortical atrophy measurements, evaluate and compare changes at different ages and/or disease stages. Al-Chalabi and Hardiman (2013) proposed a disease model in which every person is born with a level of genetic burden, and it is the combination of environmental risks and ageing, on top of this genetic burden, that dictate whether the ALS disease threshold is met and disease manifests. In this way, the motor neurons with increased susceptibility to degeneration, and subjected to insult over time, will more likely lead to disease. The existence of a key histopathological characteristic of ALS such as TDP-43 aggregation, in an aged cohort, would be a prime example of this aging effect. As it was not observed in the six-month-old CRISPR- $CCNF^{S621G}$  mice, it was unlikely that changes related to TDP-43 were an early indicator of disease in this mouse model, and would more likely be a by-product of abnormal proteostasis caused by errors in RNA processing and UPS function over time (Ling et al., 2013). The expression of mutant protein at endogenous levels in the CRISPR- $CCNF^{S621G}$  mouse model may be better at providing insight into the aging-related onset of neurodegenerative diseases.

## 5.4 Conclusion

This project was significant because it provided the first comprehensive histopathological characterisation of a CRISPR-Cas 9 generated  $CCNF$  mouse model carrying an ALS/FTD linked mutation in its genome. This was one of the first steps in assessing the utility of this model for basic and pre-clinical research in ALS. The goal was to assess the novel CRISPR- $CCNF^{S621G}$  mouse model in comparison with a WT cohort,

and establish whether  $CCNF^{S621G}$  would impact cyclin F expression, and induce both proteomic changes and characteristic ALS/FTD pathologies in the mammalian system, including those previously observed in zebrafish and cell models carrying the S621G mutation. It was hypothesised that the CRISPR- $CCNF^{S621G}$  mice would show histological and proteomic differences to a WT cohort, and that the model could therefore potentially be used to study the pathomechanisms associated with mutant  $CCNF$ . However, clear histopathological differences were not evident. Only one characteristic ALS/FTD-like histopathology, significantly decreased motor neurons in the lumbar spinal cord was exhibited in the homozygous CRISPR- $CCNF^{S621G}$  model cohort. The contribution of mutant cyclin F to initiation and progression of ALS-like features in mammals is still open to investigation. The utility of the CRISPR- $CCNF^{S621G}$  model at six-months-old is still uncertain, but more information is yet to be teased out of the proteomic data and additional experiments (outlined in section 5.3.1), especially those with aged cohorts and comparative patient tissues, will provide a more comprehensive assessment of this model. This study also highlighted the importance and value of optimising and standardising experimental procedures when studying a novel mouse model for the first time, and to validate results by performing a variety of different strategies to analyse the same pathological factor. The data from this assessment of the six-month-old CRISPR- $CCNF^{S621G}$  model will underpin the work of others who will continue to develop and assess models based on mutant cyclin F, to improve our understanding of the molecular and cellular origins and progression of ALS.

# A

## Appendix

### A.1 Methods

#### A.1.1 Genotyping

Below are the cDNA sequences of analogous exon 17 and 16, from mouse and human respectively.

TABLE A.1: Mouse (*mus musculus*) exon 17, NM\_007634.4.

GAAGCGAGAAAACAGCCT	24225060
TCAGGAGGACAGAGGCAGCTTTGTCACCCACCCACCGCAGAGCTATCGA	24225010
ATCAGGAGGAGACACTGCTAGGCAGCCTTCTGGACTGGAGCCTGGAGTGC	24224960
TGCTCTGGCTATGAGGGAGACCAGGAGAGCGAAGGCGAGAAGGAGGGTGA	24224910
TG	24224860

TABLE A.2: Human (*homo sapiens*) exon 16, NM\_001761.2.

GAAGCGGGAGAACAGCCTCCAGGAAGACAGAGGCAGCTTCGTTACCACC	2505444
CCCCTGCGGAGCTGTCCAGCCAGGAGGAGACGCTGCTGGGCAGCTTCCT	2505494
CGACTGGAGCCTGGACTGCTGCTCTGGCTATGAAGGCGACCAGGAGAGTG	2505544
AGGGCGAGAAGGAGGGCGACG	2505594

## A.1.2 CRISPR-*CCNF*<sup>S621G</sup> mouse model histopathology

### A.1.2.1 Immunofluorescence staining

Below is the batch code that was written for measuring the intensity of cyclin F staining in spinal cord MNs (section 3.3.1.1). Text after two forward-slashes (//) gives comments for the user as to what the code underneath it is doing. The “waitForUser” command in this code allows the user to select the oval or freehand drawing tools to outline each neuron, add them to the ROI manager, after which their mean grey value can be measured.

```
//Ask user to select the source directory dir = getDirectory("Choose a Directory")
Generate a list of files in selected directory
list = getFileList(dir);
Array.sort(list);
Loop the code for all images in the selected directory
for (i = 0; i < list.length; i++)
filename = dir + list[i];
open(filename);
run("8-bit");
setAutoThreshold("Default dark no-reset");
//run("Threshold...");
setThreshold(11, 255);
waitForUser;
run("Close All");
```

### A.1.2.2 Nissl staining

Below is the batch code written for counting spinal cord MNs (section 3.3.2.1). Text after two forward-slashes (//) gives comments for the user as to what the code underneath it is doing. When the “waitForUser” command is reached, the user must draw a rectangular box on either the left or right ventral horn from the top of the central canal to the base of the horn.

```
//Ask user to select the source directory
dir = getDirectory("Choose a Directory")
//This generates a list of files in selected directory
list = getFileList(dir);
Array.sort(list);
```

```
//Loop the code for all images in the selected directory
for (i = 0; i <list.length; i++) {
filename = dir + list[i];
open(filename);
run("8-bit");
setAutoThreshold("Default no-reset");
waitForUser;
//This allows the user to select and run("Threshold...");
setOption("BlackBackground", false);
run("Convert to Mask");
waitForUser;
run("Analyze Particles...", "size=80-Infinity display exclude clear summarize add
insitu");
run("Close All");
}
```

### A.1.3 CRISPR-*CCNF*<sup>S621G</sup> mouse model tissue protein analysis

#### A.1.3.1 Protein lysate collection

Protocol used by Ms Flora Cheng to collect total protein lysates from fresh-frozen brain hemisphere tissue from WT and heterozygous and homozygous CRISPR-*CCNF*<sup>S621G</sup> mice.

Five times the weight of brain tissue in volume of complete RIPA buffer (10X plus phospho stop, 7X complete protease inhibitor, and RIPA buffer) was added to each brain which was kept on ice. The brains were sheared (Sonic Rupto 250, Omni International): four rounds of 10 pulses at 30% power, with mechanical shearing by pipette tip in between. The lysates were ultracentrifuged (40 min, 45,000 rpm, 4 °C) and the supernatant containing protein lysate, was collected. Total protein concentration was quantified via a bicinchoninic acid (BCA) assay following the Pierce<sup>TM</sup> BCA Protein Assay Kit (ThermoFisher). Triplicates of eight Milli-Q<sup>®</sup> H<sub>2</sub>O diluted albumin protein standards ranging from 0.00-0.80 μg/μL, and the protein lysate samples from, CRISPR-*CCNF*<sup>S621G</sup> mice brain, diluted with Milli-Q<sup>®</sup> H<sub>2</sub>O to 1:20, 1:15, 1:5, and 1:15, respectively, were loaded in triplicate into a 96-well optical reaction plate. A 50:1 dilution of solution A to solution B was prepared and 200 μL of this AB solution was added to each well. The plate was incubated (20 min, 37 °C) and absorbance (570 nm) levels from the standards and each sample read by the PHERAstar FS plate reader (BMG Labtech). A standard curve of protein concentration was generated from the average absorbance

levels of the standards, and the trend-line equation and  $R^2$  value were used to calculate sample protein concentrations. To prepare the proteins for SDS-PAGE, 4X loading buffer and 10X reducing reagent (DTT) were added to 15  $\mu\text{g}$  of each sample proteins such that all samples had the same volume. Samples were boiled (95  $^{\circ}\text{C}$ , 5 min) and centrifuged at 10,000 rpm for 5 sec. Each sample was loaded into 4-15% criterion<sup>TM</sup> TGX<sup>TM</sup> precast gel (Bio-rad), run at 85 V for 5 min, then 180 V until samples 3 cm away from the gel's edge. To visualise protein lanes, the gel was Coomassie stained (0.29 g Coomassie Blue R250 (ThermoFisher) in 500 mL 50%  $\text{CH}_3\text{OH}$ , 10% acetic acid, 15 min, RT, with rocking), rinsed with 25%  $\text{CH}_3\text{OH}$ , de-stained with 25%  $\text{CH}_3\text{OH}$  (overnight, RT, with rocking), and then imaged on the ChemiDoc<sup>TM</sup> XRS system (Bio-Rad) with Image Lab software. Each protein lane was then sectioned into five even fractions which were segmented into smaller 1 mm x 1 mm pieces and placed into individual Eppendorf tubes. The pieces were de-stained further with 50%  $\text{CH}_3\text{OH}/50$  mM  $\text{NH}_4\text{HCO}_3$ , and dehydrated (10 min) with 50%  $\text{CH}_3\text{CN}/50$  mM  $\text{NH}_4\text{HCO}_3$ , then 30 s with 100%  $\text{CH}_3\text{CN}$ . Next, pieces were air-dried, reduced by 10 mM DTT in 50 mM  $\text{NH}_4\text{HCO}_3$  (incubated at 37  $^{\circ}\text{C}$ , 45 min), alkylated by 20 mM iodoacetamide in 50mM  $\text{NH}_4\text{HCO}_3$ , and incubated in dark (RT, 45 min). The pieces were rinsed twice with 50%  $\text{CH}_3\text{CN}/50$  mM  $\text{NH}_4\text{HCO}_3$  for 5mins, dehydrated again with 100%  $\text{CH}_3\text{CN}$ , and air-dried. The gel pieces were trypsinised (1:75 trypsin:protein in 50mM  $\text{NH}_4\text{HCO}_3$ , overnight, 37  $^{\circ}\text{C}$ ), and peptides were extracted: 50%  $\text{CH}_3\text{CN}/2\%$  formic acid (RT, 15 min), dehydrated with 100%  $\text{CH}_3\text{CN}$ , dried in a vacuum centrifuge and re-suspended in 0.1% formic acid. For peptide clean-up, a C18 ziptip (OMIX C18 from Agilent, #Cat A57003100K) for each of the nine samples, was washed with 100  $\mu\text{L}$  100%  $\text{CH}_3\text{CN}$ . Each ziptip was equilibrated with 100  $\mu\text{L}$  0.1% formic acid, the samples were added into the ziptip and the ziptip was washed three times with 100  $\mu\text{L}$  0.1% formic acid. Peptides were eluted from the ziptip into an Eppendorf tube with 50%  $\text{CH}_3\text{CN}$  in 0.1% Formic Acid, the peptide solution was evaporated to dryness in a vacuum centrifuge, and then resuspended in 0.1% formic acid for mass spectrometry analysis.



## A.2 Results

### A.2.1 Mass spectrometry

#### A.2.1.1 Gene Ontology analysis

TABLE A.3: GO biological process categories from 564 “under-expressed” proteins in the heterozygous and homozygous CRISPR-*CCNF*<sup>S621G</sup> mice.

Monoacylglycerol catabolic process
ADP biosynthetic process
4-hydroxyproline metabolic process
Proline catabolic process
Aspartate catabolic process
Gamma-aminobutyric acid metabolic process
Valine metabolic process
Positive regulation of attachment of spindle microtubules to kinetochore
Positive regulation of autophagosome assembly
Positive regulation of protein localisation to Cajal body
Glyoxylate metabolic process
Branched-chain amino acid catabolic process
Fatty acid beta-oxidation using acyl-CoA dehydrogenase
IRES-dependent viral translational initiation
Positive regulation of establishment of protein localisation to telomere
AMP metabolic process
Short-chain fatty acid metabolic process
Peptidyl-serine dephosphorylation
Positive regulation of telomerase RNA localisation to Cajal body
Glutamate metabolic process
Dicarboxylic acid biosynthetic process
Nucleoside monophosphate phosphorylation
NADPH regeneration
Acetyl-CoA biosynthetic process
Positive regulation of amino acid transport
Glutamine metabolic process
Alditol metabolic process
Cellular response to interleukin-7
Tricarboxylic acid cycle
Positive regulation of telomere maintenance via telomerase
Phospholipid catabolic process
Toxin transport
Dopamine receptor signalling pathway
COPII vesicle coating
Regulation of microtubule polymerisation
Response to epidermal growth factor
Alpha-amino acid biosynthetic process
IRE1-mediated unfolded protein response
Pyruvate metabolic process
Protein folding

Table A.3 continued...

Cytoskeleton-dependent cytokinesis
Cytoplasmic translation
Ephrin receptor signalling pathway
Translational initiation
Glucose metabolic process
Platelet activation
Regulation of mRNA processing
Mitotic anaphase
Actin filament organisation
Stimulatory C-type lectin receptor signalling pathway
Regulation of extent of cell growth
Establishment of protein localisation to endoplasmic reticulum
Protein homooligomerization
Vacuolar transport
Fc receptor signalling pathway
Ribonucleoprotein complex assembly
Establishment or maintenance of cell polarity
Response to starvation
Positive regulation of cellular amide metabolic process
Positive regulation of cell morphogenesis involved in differentiation
Mitotic prometaphase
Positive regulation of neuron projection development
Peptidyl-serine phosphorylation
Positive regulation of protein complex assembly
Nuclear-transcribed mRNA catabolic process
Negative regulation of protein kinase activity
mRNA splicing, via spliceosome
Neutrophil degranulation
Positive regulation of supramolecular fibre organisation
Response to toxic substance
Positive regulation of cytoskeleton organisation
Regulation of actin filament organisation
Response to hypoxia
Response to oxidative stress
Response to antibiotic
Protein targeting
Neuron projection morphogenesis
Regulation of vesicle-mediated transport
Protein localisation to membrane
Synaptic signalling
Negative regulation of cellular component organisation
Lipid biosynthetic process
Brain development
Organelle assembly
Apoptotic process
Intracellular signal transduction
Positive regulation of catalytic activity
Detection of chemical stimulus involved in sensory perception of smell

### A.2.2 Western blot

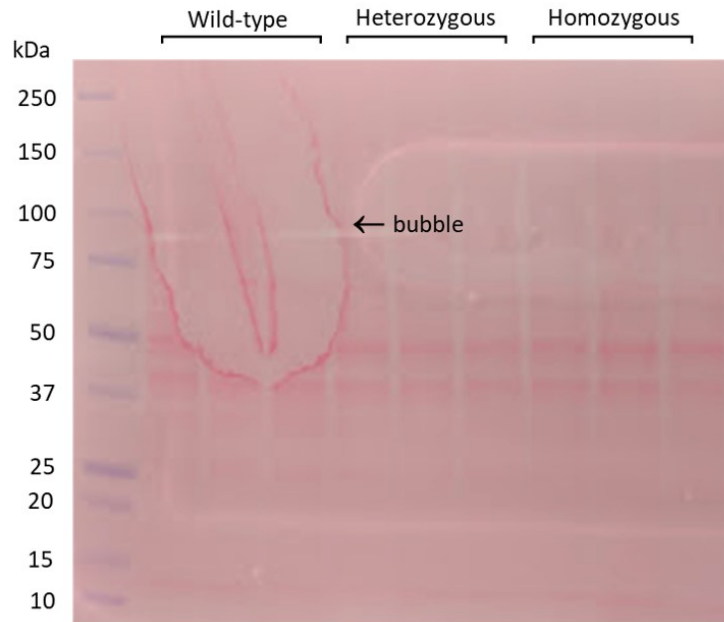


FIGURE A.1: **First Western blot membrane — incomplete protein transfer.** An image of the Ponceau stained Western blot membrane from the first Western blot experiment revealed incomplete protein transfer caused by a bubble produced in the wet transfer step. All of the mouse cohort brain protein lysates were used (from L → R) WT(#4, #15, #7), heterozygous(#14, #16, #9), and homozygous(#3, #8, #17).

### A.3 Biosafety approval letter

Please see the following three pages for details regarding the biosafety approval letter under which this study was conducted.

Appendix A.3 of this thesis has been removed as it may contain sensitive/confidential content



## References

- Al-Chalabi, A. and Hardiman, O. (2013), The epidemiology of ALS: a conspiracy of genes, environment and time, *Nature Reviews Neurology*, 9, 11, 617–628, doi:10.1038/nrneurol.2013.203 [113](#)
- Al-Chalabi, A., Jones, A., Troakes, C., King, A., Al-Sarraj, S., and van den Berg, L. H. (2012), The genetics and neuropathology of amyotrophic lateral sclerosis, *Acta Neuropathologica*, 124, 3, 339–352, doi:10.1007/s00401-012-1022-4 [2](#), [3](#), [27](#), [31](#)
- Alfaro, I. E., Albornoz, A., Molina, A., Moreno, J., Cordero, K., Criollo, A., et al. (2019), Chaperone Mediated Autophagy in the Crosstalk of Neurodegenerative Diseases and Metabolic Disorders, *Frontiers in Endocrinology*, 9, 1–13, doi:10.3389/fendo.2018.00778 [108](#)
- Anderson, C., Bredvik, K., Burstein, S., Davis, C., Meadows, S., Dash, J., et al. (2019), ALS/FTD mutant CHCHD10 mice reveal a tissue-specific toxic gain-of-function and mitochondrial stress response, *Pathology and Mechanisms of Neurological Disease*, 138, 1, 103–121, doi:10.1007/s00401-019-01989-y [5](#)
- Anderson, C. R., Ashwell, K. W. S., Collewyn, H., Conta, A., Harvey, A., Heise, C., et al. (2009), The spinal cord : a Christopher and Dana Reeve Foundation text and atlas (Academic Press, London), 1st edition [33](#), [97](#)
- Ashburner, M., Ball, C. A., Blake, J. A., Botstein, D., Butler, H., Cherry, J. M., et al. (2000), Gene ontology: tool for the unification of biology. The Gene Ontology Consortium, *Nature Genetics*, 25, 1, 25–29, doi:10.1038/75556 [36](#), [104](#)
- Australian Institute of Health and Welfare (AIHW) (2018), GRIM (General Record of Incidence of Mortality) books 2016: Motor neurone disease [1](#)
- Ayala, Y. M., De Conti, L., Avendaño-Vázquez, S. E., Dhir, A., Romano, M., D’Ambrogio, A., et al. (2011), TDP-43 regulates its mRNA levels through a negative feedback loop, *EMBO Journal*, 30, 2, 277–288, doi:10.1038/emboj.2010.310 [99](#)

- Bai, C., Richman, R., and Elledge, S. J. (1994), Human cyclin F, *The EMBO journal*, 13, 24, 6087–6098 [10](#), [101](#)
- Balendra, R. and Isaacs, A. M. (2018), C9orf72-mediated ALS and FTD: multiple pathways to disease, *Nature Reviews Neurology*, 14, 9, 544–558, doi:10.1038/s41582-018-0047-2 [2](#), [3](#)
- Barber, R. P., Phelps, P. E., Houser, C. R., Crawford, G. D., Salvaterra, P. M., and Vaughn, J. E. (1984), The morphology and distribution of neurons containing choline acetyltransferase in the adult rat spinal cord: An immunocytochemical study, *Journal of Comparative Neurology*, 229, 3, 329–346, doi:10.1002/cne.902290305 [112](#)
- Barré-Sinoussi, F. and Montagnutelli, X. (2015), Animal models are essential to biological research: issues and perspectives, *Future science OA*, 1, 4, FSO63–FSO63, doi:10.4155/fso.15.63 [11](#)
- Bauman, T. M., Ricke, E. A., Drew, S. A., Huang, W., and Ricke, W. A. (2016), Quantitation of Protein Expression and Co-localization Using Multiplexed Immunohistochemical Staining and Multispectral Imaging, *Journal of Visualized Experiments : JoVE*, , 110, 1–9, doi:10.3791/53837 [111](#)
- Belzil, V. V., Katzman, R. B., and Petrucelli, L. (2016), ALS and FTD: an epigenetic perspective, *Acta Neuropathologica*, 132, 4, 487–502, doi:10.1007/s00401-016-1587-4 [2](#)
- Berning, B. A. and Walker, A. K. (2019), The Pathobiology of TDP-43 C-Terminal Fragments in ALS and FTLD, *Frontiers in Neuroscience*, 13, 335, 1–27, doi:10.3389/fnins.2019.00335 [3](#)
- Borlado, L. R. and Méndez, J. (2007), CDC6: from DNA replication to cell cycle checkpoints and oncogenesis, *Carcinogenesis*, 29, 2, 237–243, doi:10.1093/carcin/bgm268 [109](#)
- Botella-López, A., Burgaya, F., Gavín, R., García-Ayllón, M. S., Gómez-Tortosa, E., Peña-Casanova, J., et al. (2006), Reelin expression and glycosylation patterns are altered in Alzheimer’s disease, *Proceedings of the National Academy of Sciences*, 103, 14, 5573–5578, doi:10.1073/pnas.0601279103 [106](#)
- Brettschneider, J., Lehmsiek, V., Mogel, H., Pfeifle, M., Dorst, J., Hendrich, C., et al. (2010), Proteome analysis reveals candidate markers of disease progression in amyotrophic lateral sclerosis (ALS), *Neuroscience Letters*, 468, 1, 23–27, doi:10.1016/j.neulet.2009.10.053 [110](#)
- Burdova, K., Yang, H., Faedda, R., Hume, S., Ebner, D., Kessler, B. M., et al. (2019), Cyclin F-Chk1 synthetic lethality mediated by E2F1 degradation, *bioRxiv*, 1–35, doi:10.1101/509810 [10](#)

- Chen, Z., Indjeian, V. B., McManus, M., Wang, L., and Dynlacht, B. D. (2002), CP110, a Cell Cycle-Dependent CDK Substrate, Regulates Centrosome Duplication in Human Cells, *Developmental Cell*, 3, 3, 339–350, doi:10.1016/S1534-5807(02)00258-7 [109](#)
- Chew, J., Gendron, T. F., Prudencio, M., Sasaguri, H., Zhang, Y.-J., Castanedes-Casey, M., et al. (2015), C9ORF72 repeat expansions in mice cause TDP-43 pathology, neuronal loss, and behavioral deficits, *Science*, 348, 6239, 1151–1154, doi:10.1126/science.aaa9344 [7](#)
- Chio, A., Logroscino, G., Hardiman, O., Swingler, R., Mitchell, D., Beghi, E., et al. (2009), Prognostic factors in ALS: A critical review, *Amyotrophic lateral sclerosis : official publication of the World Federation of Neurology Research Group on Motor Neuron Diseases*, 10, 5-6, 310–323, doi:10.3109/17482960802566824 [112](#)
- Clancy, B. and Cauller, L. J. (1998), Reduction of background autofluorescence in brain sections following immersion in sodium borohydride, *Journal of Neuroscience Methods*, 83, 2, 97–102, doi:https://doi.org/10.1016/S0165-0270(98)00066-1 [95](#)
- Corthell, J. T. (2014), *Basic Molecular Protocols in Neuroscience: Tips, Tricks, and Pitfalls* (Academic Press), doi:10.1016/C2014-0-00083-4 [112](#)
- D'angiolella, V., Esencay, M., and Pagano, M. (2013), A cyclin without cyclin-dependent kinases: cyclin F controls genome stability through ubiquitin-mediated proteolysis, *Trends in Cell Biology*, 23, 3, 135–140, doi:10.1016/j.tcb.2012.10.011 [10](#), [104](#)
- Dankert, J. F., Rona, G., Clijsters, L., Geter, P., Skaar, J. R., Bermudez-Hernandez, K., et al. (2016), Cyclin F-Mediated Degradation of SLBP Limits H2A.X Accumulation and Apoptosis upon Genotoxic Stress in G2, *Molecular Cell*, 64, 3, 507–519, doi:10.1016/j.molcel.2016.09.010 [109](#)
- D'Arcangelo, G. (2014), Reelin in the Years: Controlling Neuronal Migration and Maturation in the Mammalian Brain, *Advances in Neuroscience*, 2014, 1–19, doi:10.1155/2014/597395 [106](#)
- De Giorgio, F., Maduro, C., Fisher, E. M. C., and Acevedo-Arozena, A. (2019), Transgenic and physiological mouse models give insights into different aspects of amyotrophic lateral sclerosis, *Disease Models & Mechanisms*, 12, 1, 1–16, doi:10.1242/dmm.037424 [96](#), [99](#)
- Deng, H.-X., Shi, Y., Furukawa, Y., Zhai, H., Fu, R., Liu, E., et al. (2006), Conversion to the amyotrophic lateral sclerosis phenotype is associated with intermolecular linked insoluble aggregates of SOD1 in mitochondria, *Proceedings of the National Academy of Sciences*, 103, 18, 7142–7147 [3](#)

- D'Errico, P., Boido, M., Piras, A., Valsecchi, V., De Amicis, E., Locatelli, D., et al. (2013), Selective Vulnerability of Spinal and Cortical Motor Neuron Subpopulations in delta7 SMA Mice, *PLOS ONE*, 8, 12, e82654, doi:10.1371/journal.pone.0082654 97
- Devoy, A., Kalmar, B., Stewart, M., Park, H., Burke, B., Noy, S. J., et al. (2017), Humanized mutant FUS drives progressive motor neuron degeneration without aggregation in 'FUSDelta14' knockin mice, *Brain*, 140, 11, 2797–2805, doi:10.1093/brain/awx248 33, 97
- Ebstein, S. Y., Yagudayeva, I., and Shneider, N. A. (2019), Mutant TDP-43 Causes Early-Stage Dose-Dependent Motor Neuron Degeneration in a TARDBP Knockin Mouse Model of ALS, *Cell Reports*, 26, 2, 364–373, doi:10.1016/j.celrep.2018.12.045 112
- Ekegren, T., Hanrieder, J., and Bergquist, J. (2008), Clinical perspectives of high-resolution mass spectrometry-based proteomics in neuroscience—Exemplified in amyotrophic lateral sclerosis biomarker discovery research, *Journal of Mass Spectrometry*, 43, 5, 559–571, doi:10.1002/jms.1409 110
- Emanuele, M. J., Elia, A. E. H., Xu, Q., Thoma, C. R., Izhar, L., Leng, Y., et al. (2011), Global identification of modular cullin-RING ligase substrates, *Cell*, 147, 2, 459–474, doi:10.1016/j.cell.2011.09.019 109
- Emoto, K., Yamashita, S., and Okada, Y. (2005), Mechanisms of Heat-induced Antigen Retrieval: Does pH or Ionic Strength of the Solution Play a Role for Refolding Antigens?, *Journal of Histochemistry & Cytochemistry*, 53, 11, 1311–1321, doi:10.1369/jhc.5C6627.2005 94
- Evers, M. M., Toonen, L. J. A., and van Roon-Mom, W. M. C. (2015), Antisense oligonucleotides in therapy for neurodegenerative disorders, *Advanced Drug Delivery Reviews*, 87, 90–103, doi:https://doi.org/10.1016/j.addr.2015.03.008 4
- Fan, A. C. and Leung, A. K. L. (2016), RNA Granules and Diseases: A Case Study of Stress Granules in ALS and FTL, *Advances in Experimental Medicine and Biology*, 907, 263–296, doi:10.1007/978-3-319-29073-7\_11 2
- Fang, L., Teuchert, M., Huber-Abel, F., Schattauer, D., Hendrich, C., Dorst, J., et al. (2010), MMP-2 and MMP-9 are elevated in spinal cord and skin in a mouse model of ALS, *Journal of the Neurological Sciences*, 294, 1, 51–56, doi:https://doi.org/10.1016/j.jns.2010.04.005 111
- Fang, X., Ji, H., Kim, S.-W., Park, J.-I., Vaught, T. G., Anastasiadis, P. Z., et al. (2004), Vertebrate development requires ARVCF and p120 catenins and their interplay with

- RhoA and Rac, *The Journal of Cell Biology*, 165, 1, 87–98, doi:10.1083/jcb.200307109 [103](#)
- Farg, M. A., Sundaramoorthy, V., Sultana, J. M., Yang, S., Atkinson, R. A. K., Levina, V., et al. (2014), C9ORF72, implicated in amyotrophic lateral sclerosis and frontotemporal dementia, regulates endosomal trafficking, *Human Molecular Genetics*, 23, 13, 3579–3595, doi:10.1093/hmg/ddu068 [2](#)
- Feneberg, E., Gray, E., Ansorge, O., Talbot, K., and Turner, M. R. (2018), Towards a TDP-43-Based Biomarker for ALS and FTL, *Molecular Neurobiology*, 55, 10, 7789–7801, doi:10.1007/s12035-018-0947-6 [102](#)
- Flurkey, K., McUrrer, J., and Harrison, D. (2007), Mouse Models in Aging Research, in *The Mouse in Biomedical Research*, volume III (Elsevier Inc.), chapter 20, 637–672, doi:10.1016/B978-012369454-6/50074-1 [102](#), [112](#), [113](#)
- Franklin, K. B. J. and Paxinos, G. (2007), *The Mouse Brain in Stereotaxic Coordinates* (Academic Press, New York), third edition [27](#)
- FratTA, P., Sivakumar, P., Humphrey, J., Lo, K., Ricketts, T., Oliveira, H., et al. (2018), Mice with endogenous TDP-43 mutations exhibit gain of splicing function and characteristics of amyotrophic lateral sclerosis, *The EMBO journal*, 37, 11, 1–15, doi:10.15252/embj.201798684 [99](#)
- Galper, J., Rayner, S. L., Hogan, A. L., Fifita, J. A., Lee, A., Chung, R. S., et al. (2017), Cyclin F: A component of an E3 ubiquitin ligase complex with roles in neurodegeneration and cancer, *The International Journal of Biochemistry & Cell Biology*, 89, 216–220, doi:https://doi.org/10.1016/j.biocel.2017.06.011 [2](#), [10](#)
- Gong, Y., Slee, R. B., Fukai, N., Rawadi, G., Roman-Roman, S., Reginato, A. M., et al. (2001), LDL Receptor-Related Protein 5 (LRP5) Affects Bone Accrual and Eye Development, *Cell*, 107, 4, 513–523, doi:10.1016/S0092-8674(01)00571-2 [109](#)
- Gong, Y. H., Parsadanian, A. S., Andreeva, A., Snider, W. D., and Elliott, J. L. (2000), Restricted Expression of G86R Cu/Zn Superoxide Dismutase in Astrocytes Results in Astrocytosis But Does Not Cause Motoneuron Degeneration, *The Journal of Neuroscience*, 20, 2, 660–665, doi:10.1523/JNEUROSCI.20-02-00660.2000 [9](#)
- Govek, E.-E., Newey, S. E., and Van Aelst, L. (2005), The role of the Rho GTPases in neuronal development, *Genes & Development*, 19, 1, 1–49, doi:10.1101/gad.1256405 [104](#)

- Gurney, M. E., Pu, H., Chiu, A. Y., Mauro, C. D. C., Polchow, C. Y., Alexander, D. D., et al. (1994), Motor Neuron Degeneration in Mice That Express a Human Cu,Zn Superoxide Dismutase Mutation, *Science*, 264, 5166, 1772–1775, doi:10.1126/science.8209258 [9](#)
- Gusel'nikova, V. V. and Korzhevskiy, D. E. (2015), NeuN As a Neuronal Nuclear Antigen and Neuron Differentiation Marker, *Acta Naturae*, 7, 2, 42–47 [64](#)
- Hagan, C. (2017), When are mice considered old?, <https://www.jax.org/news-and-insights/jax-blog/2017/november/when-are-mice-considered-old> [102](#), [112](#), [113](#)
- He, C. Z. and Hays, A. P. (2004), Expression of peripherin in ubiquitinated inclusions of amyotrophic lateral sclerosis, *Journal of the Neurological Sciences*, 217, 1, 47–54, doi:<https://doi.org/10.1016/j.jns.2003.08.016> [64](#), [97](#)
- Hicks, G. G., Singh, N., Nashabi, A., Mai, S., Bozek, G., Klewes, L., et al. (2000), Fus deficiency in mice results in defective B-lymphocyte development and activation, high levels of chromosomal instability and perinatal death, *Nature Genetics*, 24, 2, 175–179, doi:10.1038/72842 [7](#)
- Hogan, A. L., Don, E. K., Fifita, J. A., Williams, K. L., Chung, R. S., Laird, A. S., et al. (2018), Constitutive overexpression of the ALS-linked gene CCNF fusions results in cytotoxicity to preclude generation of transgenic zebrafish models, *Matters*, 4, 3, 1–6 [11](#)
- Hogan, A. L., Don, E. K., Rayner, S. L., Lee, A., Laird, A. S., Watchon, M., et al. (2017), Expression of ALS/FTD-linked mutant CCNF in zebrafish leads to increased cell death in the spinal cord and an aberrant motor phenotype, *Human Molecular Genetics*, 26, 14, 2616–2626, doi:10.1093/hmg/ddx136 [11](#), [12](#), [101](#), [102](#), [104](#), [105](#), [109](#)
- Iguchi, Y., Katsuno, M., Niwa, J.-i., Takagi, S., Ishigaki, S., Ikenaka, K., et al. (2013), Loss of TDP-43 causes age-dependent progressive motor neuron degeneration, *Brain*, 136, 5, 1371–1382, doi:10.1093/brain/awt029 [9](#)
- Ikeda, W., Nakanishi, H., Miyoshi, J., Mandai, K., Ishizaki, H., Tanaka, M., et al. (1999), Afadin: A Key Molecule Essential for Structural Organization of Cell-Cell Junctions of Polarized Epithelia during Embryogenesis, *Journal of Cell Biology*, 146, 5, 1117–1131, doi:10.1083/jcb.146.5.1117 [103](#)
- Iridoy, M. O., Zubiri, I., Zelaya, M. V., Martinez, L., Ausín, K., Lachen-Montes, M., et al. (2018), Neuroanatomical Quantitative Proteomics Reveals Common Pathogenic Biological Routes between Amyotrophic Lateral Sclerosis (ALS) and Frontotemporal

- Dementia (FTD), *International Journal of Molecular Sciences*, 20, 4, 1–24, doi:10.3390/ijms20010004 [105](#)
- Ito, D., Hatano, M., and Suzuki, N. (2017), RNA binding proteins and the pathological cascade in ALS/FTD neurodegeneration, *Science Translational Medicine*, 9, 415, 1–10, doi:10.1126/scitranslmed.aah5436 [105](#)
- Ke, Y., van Hummel, A., Stevens, C., Gladbach, A., Ippati, S., Bi, M., et al. (2015), Short-term suppression of A315T mutant human TDP-43 expression improves functional deficits in a novel inducible transgenic mouse model of FTLD-TDP and ALS, *Pathology and Mechanisms of Neurological Disease*, 130, 5, 661–678, doi:10.1007/s00401-015-1486-0 [111](#)
- Kim, J.-E., Hong, Y. H., Kim, J. Y., Jeon, G. S., Jung, J. H., Yoon, B.-N., et al. (2017), Altered nucleocytoplasmic proteome and transcriptome distributions in an in vitro model of amyotrophic lateral sclerosis, *PLOS ONE*, 12, 4, 1–23, doi:10.1371/journal.pone.0176462 [106](#), [109](#)
- Kino, Y., Washizu, C., Kurosawa, M., Yamada, M., Miyazaki, H., Akagi, T., et al. (2015), FUS/TLS deficiency causes behavioral and pathological abnormalities distinct from amyotrophic lateral sclerosis, *Acta Neuropathologica Communications*, 3, 1, 1–11, doi:10.1186/s40478-015-0202-6 [7](#)
- Kiral, F. R., Kohrs, F. E., Jin, E. J., and Hiesinger, P. R. (2018), Rab GTPases and Membrane Trafficking in Neurodegeneration, *Current biology : CB*, 28, 8, R471–R486, doi:10.1016/j.cub.2018.02.010 [105](#)
- Kitano, M., Nakaya, M., Nakamura, T., Nagata, S., and Matsuda, M. (2008), Imaging of Rab5 activity identifies essential regulators for phagosome maturation, *Nature*, 453, 7192, 241–245, doi:10.1038/nature06857 [104](#)
- Kong, M., Barnes, E. A., Ollendorff, V., and Donoghue, D. J. (2000), Cyclin F regulates the nuclear localization of cyclin B1 through a cyclin–cyclin interaction, *EMBO Journal*, 19, 6, 1378–1388, doi:10.1093/emboj/19.6.1378 [10](#)
- Kruminis-Kaszkiel, E., Juranek, J., Maksymowicz, W., and Wojtkiewicz, J. (2018), CRISPR/Cas9 Technology as an Emerging Tool for Targeting Amyotrophic Lateral Sclerosis (ALS), *International Journal of Molecular Sciences*, 19, 3, 1–13, doi:10.3390/ijms19030906 [5](#)
- Lackie, R. E., Maciejewski, A., Ostapchenko, V. G., Marques-Lopes, J., Choy, W.-Y., Duennwald, M. L., et al. (2017), The Hsp70/Hsp90 Chaperone Machinery in Neurodegenerative Diseases, *Frontiers in Neuroscience*, 11, 254, 1–23, doi:10.3389/fnins.2017.00254 [108](#)

- Lee, A., Rayner, S., Gwee, S., Luca, A., Shahheydari, H., Sundaramoorthy, V., et al. (2018), Pathogenic mutation in the ALS/FTD gene, CCNF, causes elevated Lys48-linked ubiquitylation and defective autophagy, *Cellular and Molecular Life Sciences*, 75, 2, 335–354, doi:10.1007/s00018-017-2632-8 [11](#), [35](#), [96](#), [101](#), [105](#), [108](#)
- Lee, A., Rayner, S. L., De Luca, A., Gwee, S. S. L., Morsch, M., Sundaramoorthy, V., et al. (2017), Casein kinase II phosphorylation of cyclin F at serine 621 regulates the Lys48-ubiquitylation E3 ligase activity of the SCF(cyclin F) complex, *Open Biology*, 7, 10, 1–11, doi:10.1098/rsob.170058 [97](#), [99](#)
- Lee, Y.-K. and Lee, J.-A. (2016), Role of the mammalian ATG8/LC3 family in autophagy: differential and compensatory roles in the spatiotemporal regulation of autophagy, *BMB reports*, 49, 8, 424–430, doi:10.5483/bmbrep.2016.49.8.081 [105](#)
- Li-Cor Biosciences (2019), Application Guide: Good Westerns Gone Bad, <https://www.licor.com/documents/dq6jb8sgnkiwlas0g99b5hq0tsuvczyz> [82](#)
- Ling, S.-C., Polymenidou, M., and Cleveland, D. (2013), Converging Mechanisms in ALS and FTD: Disrupted RNA and Protein Homeostasis, *Neuron*, 79, 3, 416–438, doi:10.1016/j.neuron.2013.07.033 [96](#), [97](#), [113](#)
- Liu, C. (2013), Strategies for designing transgenic DNA constructs, *Methods in Molecular Biology*, 1027, 183–201, doi:10.1007/978-1-60327-369-5\_8 [3](#), [4](#)
- Liu, Y., Pattamatta, A., Zu, T., Reid, T., Bardhi, O., Borchelt, D. R., et al. (2016), C9orf72 BAC mouse model with motor deficits and neurodegenerative features of ALS/FTD, *Neuron*, 90, 3, 521–534 [108](#), [111](#)
- Livak, K. J. and Schmittgen, T. D. (2001), Analysis of relative gene expression data using real-time quantitative PCR and the 2  $\Delta\Delta$ CT method, *Methods*, 25, 4, 402–408 [41](#)
- Lutz, C. (2018), Mouse models of ALS: Past, present and future, *Brain Research*, 1693, 1–10, doi:https://doi.org/10.1016/j.brainres.2018.03.024 [3](#), [96](#)
- Machamer, J. B., Collins, S. E., and Lloyd, T. E. (2014), The ALS gene FUS regulates synaptic transmission at the Drosophila neuromuscular junction, *Human Molecular Genetics*, 23, 14, 3810–3822, doi:10.1093/hmg/ddu094 [3](#)
- Mancuso, R. and Navarro, X. (2015), Amyotrophic lateral sclerosis: Current perspectives from basic research to the clinic, *Progress in Neurobiology*, 133, 1–26, doi:10.1016/j.pneurobio.2015.07.004 [1](#), [2](#), [3](#), [27](#), [68](#), [104](#)

- Marden, J. J., Harraz, M. M., Williams, A. J., Nelson, K., Luo, M., Paulson, H., et al. (2007), Redox modifier genes in amyotrophic lateral sclerosis in mice, *The Journal of Clinical Investigation*, 117, 10, 2913–2919, doi:10.1172/JCI31265 97
- McCann, E. P., Williams, K. L., Fifita, J. A., Tarr, I. S., O' Connor, J., Rowe, D. B., et al. (2017), The genotype–phenotype landscape of familial amyotrophic lateral sclerosis in Australia, *Clinical Genetics*, 92, 3, 259–266, doi:10.1111/cge.12973 1, 2, 112
- Mi, H., Muruganujan, A., Ebert, D., Huang, X., and Thomas, P. D. (2018), PANTHER version 14: more genomes, a new PANTHER GO-slim and improvements in enrichment analysis tools, *Nucleic Acids Research*, 47, D1, 419–426, doi:10.1093/nar/gky1038 36
- Morrice, J. R., Gregory-Evans, C. Y., and Shaw, C. A. (2018), Animal models of amyotrophic lateral sclerosis: A comparison of model validity, *Neural Regeneration Research*, 13, 12, 2050–2054, doi:10.4103/1673-5374.241445 96
- Morrison, B. M., Morrison, J. H., Ripps, M. E., and Gordon, J. W. (1996), Quantitative immunocytochemical analysis of the spinal cord in G86R superoxide dismutase transgenic mice: Neurochemical correlates of selective vulnerability, *Journal of Comparative Neurology*, 373, 4, 619–631, doi:10.1002/(SICI)1096-9861(19960930)373:4<619::AID-CNE9>3.0.CO2-4 112
- Neumann, M., Sampathu, D. M., Kwong, L. K., Truax, A. C., Micsenyi, M. C., Chou, T. T., et al. (2006), Ubiquitinated TDP-43 in Frontotemporal Lobar Degeneration and Amyotrophic Lateral Sclerosis, *Science*, 314, 5796, 130–133, doi:10.1126/science.1134108 2, 64, 97
- Ng, A. S. L., Rademakers, R., and Miller, B. L. (2015), Frontotemporal dementia: a bridge between dementia and neuromuscular disease, *Annals of the New York Academy of Sciences*, 1338, 1, 71–93, doi:10.1111/nyas.12638 2, 68
- Nguyen, H. P., Van Broeckhoven, C., and van der Zee, J. (2018), ALS Genes in the Genomic Era and their Implications for FTD, *Trends in Genetics*, 34, 6, 404–423, doi: https://doi.org/10.1016/j.tig.2018.03.001 1
- Ogita, H., Rikitake, Y., Miyoshi, J., and Takai, Y. (2010), Cell adhesion molecules nectins and associating proteins: Implications for physiology and pathology, *Proceedings of the Japan Academy. Series B, Physical and Biological Sciences*, 86, 6, 621–629, doi: 10.2183/pjab.86.621 103
- O'Rourke, J. G., Bogdanik, L., Muhammad, A., Gendron, T. F., Kim, K. J., Austin, A., et al. (2015), C9orf72 BAC transgenic mice display typical pathologic features of ALS/FTD, *Neuron*, 88, 5, 892–901 2, 7

- O'Rourke, J. G., Bogdanik, L., Yáñez, A., Lall, D., Wolf, A. J., Muhammad, A. K. M. G., et al. (2016), C9orf72 is required for proper macrophage and microglial function in mice, *Science*, 351, 6279, 1324–1329, doi:10.1126/science.aaf1064 7
- Parakh, S., Perri, E. R., Jagaraj, C. J., Ragagnin, A. M. G., and Atkin, J. D. (2018), Rab-dependent cellular trafficking and amyotrophic lateral sclerosis, *Critical Reviews in Biochemistry and Molecular Biology*, 53, 6, 623–651, doi:10.1080/10409238.2018.1553926 105
- Pavloff, N., Rivard, D., Masson, S., Shen, S.-H., and Mes-Masson, A.-M. (1992), Sequence analysis of the large and small subunits of human ribonucleotide reductase, *DNA Sequence*, 2, 4, 227–234, doi:10.3109/10425179209020807 109
- Picher-Martel, V., Valdmanis, P. N., Gould, P. V., Julien, J.-P., and Dupré, N. (2016), From animal models to human disease: a genetic approach for personalized medicine in ALS, *Acta Neuropathologica Communications*, 4, 70, 1–29, doi:10.1186/s40478-016-0340-5 1, 104, 112
- Prasad, A., Bharathi, V., Sivalingam, V., Girdhar, A., and Patel, B. K. (2019), Molecular Mechanisms of TDP-43 Misfolding and Pathology in Amyotrophic Lateral Sclerosis, *Frontiers in molecular neuroscience*, 12, 25, doi:10.3389/fnmol.2019.00025 97
- Pyon, W. S., Gray, D. T., and Barnes, C. A. (2019), An Alternative to Dye-Based Approaches to Remove Background Autofluorescence From Primate Brain Tissue, *Frontiers in Neuroanatomy*, 13, 1–10 95
- QIAGEN (2005), AllPrep DNA/RNA Mini Handbook, <https://www.qiagen.com/au/resources/resourcedetail?id=bbd50261-3b80-4657-ad58-6a5a97b88821lang=en> 23
- Rademakers, R., Cruts, M., and Van Broeckhoven, C. (2004), The role of tau ( MAPT ) in frontotemporal dementia and related tauopathies, *Human Mutation*, 24, 4, 277–295, doi:10.1002/humu.20086 108
- Radulovic, M. and Godovac-Zimmermann, J. (2011), Proteomic approaches to understanding the role of the cytoskeleton in host-defense mechanisms, *Expert Review of Proteomics*, 8, 1, 117–126, doi:10.1586/epr.10.91 74
- Ragagnin, A. M. G., Shadfar, S., Vidal, M., Jamali, M. S., and Atkin, J. D. (2019), Motor Neuron Susceptibility in ALS/FTD, *Frontiers in Neuroscience*, 13, 532, 1–37 68
- Reaume, A. G., Elliott, J. L., Hoffman, E. K., Kowall, N. W., Ferrante, R. J., Siwek, D. R., et al. (1996), Motor neurons in Cu/Zn superoxide dismutase-deficient mice develop

- normally but exhibit enhanced cell death after axonal injury, *Nature Genetics*, 13, 1, 43–47 [9](#), [97](#)
- Renton, A. E., Chiò, A., and Traynor, B. J. (2013), State of play in amyotrophic lateral sclerosis genetics, *Nature Neuroscience*, 17, 1, 17–23, doi:10.1038/nn.3584 [1](#), [2](#), [3](#), [96](#), [113](#)
- Robertson, D., Savage, K., Reis-Filho, J. S., and Isacke, C. M. (2008), Multiple immunofluorescence labelling of formalin-fixed paraffin-embedded (FFPE) tissue, *BMC Cell Biology*, 9, 1, 1–10, doi:10.1186/1471-2121-9-13 [95](#)
- Sander, J. D. and Joung, J. K. (2014), CRISPR-Cas systems for editing, regulating and targeting genomes, *Nature Biotechnology*, 32, 4, 347–355, doi:10.1038/nbt.2842<https://www.nature.com/articles/nbt.2842#supplementary-information> [4](#)
- Santos, R. R., Torres, K. C., Lima, G. S., Fiamoncini, C. M., Mapa, F. C., Pereira, P. A., et al. (2014), Reduced frequency of T lymphocytes expressing CTLA-4 in frontotemporal dementia compared to Alzheimer’s disease, *Progress in Neuro-Psychopharmacology and Biological Psychiatry*, 48, 1–5, doi:<https://doi.org/10.1016/j.pnpbp.2013.06.019> [108](#)
- Saraceno, C., Catania, M., Paterlini, A., Fostinelli, S., Ciani, M., Zanardini, R., et al. (2018), Altered Expression of Circulating Cdc42 in Frontotemporal Lobar Degeneration, *Journal of Alzheimer’s disease : JAD*, 61, 4, 1477–1483, doi:10.3233/JAD-170722 [75](#), [104](#)
- Schindelin, J., Arganda-Carreras, I., Frise, E., Kaynig, V., Longair, M., Pietzsch, T., et al. (2012), Fiji: an open-source platform for biological-image analysis, *Nature methods*, 9, 7, 676–682, doi:10.1038/nmeth.2019 [32](#)
- Schweitzer, B. and Kingsmore, S. F. (2002), Measuring proteins on microarrays, *Current Opinion in Biotechnology*, 13, 1, 14–19, doi:[https://doi.org/10.1016/S0958-1669\(02\)00278-1](https://doi.org/10.1016/S0958-1669(02)00278-1) [111](#)
- Scotter, E. L., Chen, H.-J., and Shaw, C. E. (2015), TDP-43 Proteinopathy and ALS: Insights into Disease Mechanisms and Therapeutic Targets, *Neurotherapeutics*, 12, 2, 352–363, doi:10.1007/s13311-015-0338-x [2](#)
- Sharma, A., Lyashchenko, A. K., Lu, L., Nasrabad, S. E., Elmaleh, M., Mendelsohn, M., et al. (2016), ALS-associated mutant FUS induces selective motor neuron degeneration through toxic gain of function, *Nature Communications.*, 7, 1, 1–14, doi:10.1038/ncomms10465 [7](#)

- Shi, S. R., Key, M. E., and Kalra, K. L. (1991), Antigen retrieval in formalin-fixed, paraffin-embedded tissues: an enhancement method for immunohistochemical staining based on microwave oven heating of tissue sections, *The Journal of Histochemistry and Cytochemistry : Official Journal of the Histochemistry Society*, 39, 6, 741–748, doi:10.1177/39.6.1709656 94
- Soo, K., Halloran, M., Sundaramoorthy, V., Parakh, S., Toth, R., Southam, K., et al. (2015), Rab1-dependent ER–Golgi transport dysfunction is a common pathogenic mechanism in SOD1, TDP-43 and FUS-associated ALS, *Pathology and Mechanisms of Neurological Disease*, 130, 5, 679–697, doi:10.1007/s00401-015-1468-2 105
- Spitzer, N., Sammons, G. S., and Price, E. M. (2011), Autofluorescent cells in rat brain can be convincing impostors in green fluorescent reporter studies, *Journal of Neuroscience Methods*, 197, 1, 48–55, doi:10.1016/j.jneumeth.2011.01.029 95
- Stankiewicz, T. R. and Linseman, D. A. (2014), Rho family GTPases: key players in neuronal development, neuronal survival, and neurodegeneration, *Frontiers in Cellular Neuroscience*, 8, 314, doi:10.3389/fncel.2014.00314 75
- Stephenson, J. and Amor, S. (2017), Modelling amyotrophic lateral sclerosis in mice, *Drug Discovery Today: Disease Models*, 25-26, 35–44, doi:https://doi.org/10.1016/j.ddmod.2018.10.001 96
- Storm-Mathisen, J. (1977), Localization of transmitter candidates in the brain: the hippocampal formation as a model, *Progress in Neurobiology*, 8, 119–181, doi:https://doi.org/10.1016/0301-0082(77)90013-2 112
- Strachan, T. and Read, A. (2011), *Human Molecular Genetics* (Garland Science, New York, USA), 4th edition 99
- Swarup, V., Phaneuf, D., Bareil, C., Robertson, J., Rouleau, G. A., Kriz, J., et al. (2011), Pathological hallmarks of amyotrophic lateral sclerosis/frontotemporal lobar degeneration in transgenic mice produced with TDP-43 genomic fragments, *Brain*, 134, 9, 2610–2626, doi:10.1093/brain/awr159 9
- Szklarczyk, D., Gable, A. L., Lyon, D., Junge, A., Wyder, S., Huerta-Cepas, J., et al. (2019), STRING v11: protein-protein association networks with increased coverage, supporting functional discovery in genome-wide experimental datasets, *Nucleic Acids Research*, 47, D1, D607–D613, doi:10.1093/nar/gky1131 36
- Tai, X., Van Laethem, F., Pobeziński, L., Guintier, T., Sharrow, S. O., Adams, A., et al. (2012), Basis of CTLA-4 function in regulatory and conventional CD4(+) T cells, *Blood*, 119, 22, 5155–5163, doi:10.1182/blood-2011-11-388918 108

- Tan, R. H., Ke, Y. D., Ittner, L. M., and Halliday, G. M. (2017), ALS/FTLD: experimental models and reality, *Acta Neuropathologica*, 133, 2, 177–196, doi:10.1007/s00401-016-1666-6 [1](#), [2](#)
- The Gene Ontology Consortium (2018), The Gene Ontology Resource: 20 years and still GOing strong, *Nucleic Acids Research*, 47, D1, 330–338, doi:10.1093/nar/gky1055 [36](#), [104](#)
- Thomas, P. D., Campbell, M. J., Kejariwal, A., Mi, H., Karlak, B., Daverman, R., et al. (2003), PANTHER: A Library of Protein Families and Subfamilies Indexed by Function, *Genome Research*, 13, 9, 2129–2141, doi:10.1101/gr.772403 [36](#)
- Tu, Z., Yang, W., Yan, S., Guo, X., and Li, X.-J. (2015), CRISPR/Cas9: a powerful genetic engineering tool for establishing large animal models of neurodegenerative diseases, *Molecular Neurodegeneration*, 10, 1, 1–8, doi:10.1186/s13024-015-0031-x [5](#)
- Uhlén, M., Fagerberg, L., Hallström, B. M., Lindskog, C., Oksvold, P., Mardinoglu, A., et al. (2015), Tissue-based map of the human proteome, *Science*, 347, 6220, 12604191–12604199, doi:10.1126/science.1260419 [83](#), [85](#)
- van Blitterswijk, M., van Es, M. A., Hennekam, E. A. M., Dooijes, D., van Rheenen, W., Medic, J., et al. (2012), Evidence for an oligogenic basis of amyotrophic lateral sclerosis, *Human Molecular Genetics*, 21, 17, 3776–3784, doi:10.1093/hmg/ddc199 [113](#)
- van Hummel, A., Chan, G., van Der Hoven, J., Morsch, M., Ippati, S., Suh, L., et al. (2018), Selective Spatiotemporal Vulnerability of Central Nervous System Neurons to Pathologic TAR DNA-Binding Protein 43 in Aged Transgenic Mice, *The American Journal of Pathology*, 188, 6, 1447–1456, doi:10.1016/j.ajpath.2018.03.002 [27](#)
- Vance, C., Rogelj, B., Hortobágyi, T., De Vos, K. J., Nishimura, A. L., Sreedharan, J., et al. (2009), Mutations in FUS, an RNA Processing Protein, Cause Familial Amyotrophic Lateral Sclerosis Type 6, *Science*, 323, 5918, 1208–1211, doi:10.1126/science.1165942 [68](#)
- Verbeeck, C., Deng, Q., Dejesus-Hernandez, M., Taylor, G., Ceballos-Diaz, C., Kocerha, J., et al. (2012), Expression of Fused in sarcoma mutations in mice recapitulates the neuropathology of FUS proteinopathies and provides insight into disease pathogenesis, *Molecular Neurodegeneration*, 7, 1, 1–13, doi:10.1186/1750-1326-7-53 [7](#)
- Vermeulen, J., De Preter, K., Lefever, S., Nuytens, J., De Vloed, F., Derveaux, S., et al. (2011), Measurable impact of RNA quality on gene expression results from quantitative PCR, *Nucleic Acids Research*, 39, 9, 1–12, doi:10.1093/nar/gkr065 [100](#)

- Watts, J. K. and Corey, D. R. (2012), Silencing disease genes in the laboratory and the clinic, *The Journal of Pathology*, 226, 2, 365–379, doi:10.1002/path.2993 4
- Wexler, N. S., Young, A. B., Tanzi, R. E., Travers, H., Starosta-Rubinstein, S., Penney, J. B., et al. (1987), Homozygotes for Huntington's disease, *Nature*, 326, 6109, 194–197, doi:10.1038/326194a0 98
- White, M. A., Kim, E., Duffy, A., Adalbert, R., Phillips, B. U., Peters, O. M., et al. (2018), TDP-43 gains function due to perturbed autoregulation in a Tardbp knock-in mouse model of ALS-FTD, *Nature Neuroscience*, 21, 4, 552–563, doi:10.1038/s41593-018-0113-5 111
- Williams, K. L., Topp, S., Yang, S., Smith, B., Fifita, J. A., Warraich, S. T., et al. (2016), CCNF mutations in amyotrophic lateral sclerosis and frontotemporal dementia, *Nature Communications*, 7, 11253–11259, doi:10.1038/ncomms11253https://www.nature.com/articles/ncomms11253#supplementary-information 1, 10, 11, 64, 96, 101, 105, 109
- Xia, R., Liu, Y., Yang, L., Gal, J., Zhu, H., and Jia, J. (2012), Motor neuron apoptosis and neuromuscular junction perturbation are prominent features in a Drosophila model of Fus-mediated ALS, *Molecular Neurodegeneration*, 7, 1, 1–17, doi:10.1186/1750-1326-7-10 3
- Yamano, K., Fogel, A. I., Wang, C., van der Blik, A. M., and Youle, R. J. (2014), Mitochondrial Rab GAPs govern autophagosome biogenesis during mitophagy, *eLife*, 3, 1–24, doi:10.7554/eLife.01612 105
- Yan, S., Wang, C.-E., Wei, W., Gaertig, M. A., Lai, L., Li, S., et al. (2014), TDP-43 causes differential pathology in neuronal versus glial cells in the mouse brain, *Human Molecular Genetics*, 23, 10, 2678–2693, doi:10.1093/hmg/ddt662 9
- Yang, C., Danielson, E. W., Qiao, T., Metterville, J., Brown, R. H., Landers, J. E., et al. (2016), Mutant PFN1 causes ALS phenotypes and progressive motor neuron degeneration in mice by a gain of toxicity, *Proceedings of the National Academy of Sciences*, 113, 41, E6209–E6218, doi:10.1073/pnas.1605964113 98
- Yulug, I., Egan, S., See, C., and Fisher, E. (1995), A human SHC-related sequence maps to chromosome 17, the SHC gene maps to chromosome 1, *Human Genetics*, 96, 2, 245–248, doi:10.1007/BF00207393 109
- Zhang, X.-M., Walsh, B., Mitchell, C. A., and Rowe, T. (2005), TBC domain family, member 15 is a novel mammalian Rab GTPase-activating protein with substrate preference for Rab7, *Biochemical and Biophysical Research Communications*, 335, 1, 154–161, doi:https://doi.org/10.1016/j.bbrc.2005.07.070 105

- Zhao, R., Lange, D., Voustianiouk, A., MacGrogan, D., Ho, L., Suh, J., et al. (2006), A ketogenic diet as a potential novel therapeutic intervention in amyotrophic lateral sclerosis, *BMC Neuroscience*, 7, 29, 1–10, doi:10.1186/1471-2202-7-29 [33](#), [97](#)
- Zhao, W., Varghese, M., Vempati, P., Dzhun, A., Cheng, A., Wang, J., et al. (2012), Caprylic Triglyceride as a Novel Therapeutic Approach to Effectively Improve the Performance and Attenuate the Symptoms Due to the Motor Neuron Loss in ALS Disease, *PLOS ONE*, 7, 11, e49191, doi:10.1371/journal.pone.0049191 [33](#), [97](#)